

**Magnetic Braking in Neutron Star Low Mass X-Ray Binaries**

by

Kenny Van

A thesis submitted in partial fulfillment of the requirements for the degree of

Doctor of Philosophy

Department of Physics  
University of Alberta

# Abstract

In this thesis, we investigate the effectiveness of the Skumanich magnetic braking prescription and propose two other magnetic braking schemes. First I will review some of the current fundamentals of binary systems and binary evolution along with a derivation of the Skumanich magnetic braking. Following this review, I introduce a boosted Skumanich prescription which includes the effects of stellar wind loss and convective turnover time. While this magnetic braking prescription more effectively reproduces observed persistent low-mass X-ray binaries than the commonly used Skumanich prescription, the most effective form of the boosted Skumanich prescription uses and ad-hoc wind and convection boosting. The second magnetic braking prescription introduced is the Convection and Rotation Boosted (CARB) magnetic braking that explicitly accounts for both the wind and convection leading to a more physical description of magnetic braking. After demonstrating the effectiveness of CARB magnetic braking, I use a comprehensive grid of simulated systems to determine the formation rates of progenitor binaries necessary to reproduce observed LMXBs. The progenitor search of observed LMXBs also revealed gaps in the observed parameter space where I propose some observed LMXBs with incomplete observed quantities may lie. Finally, I summarize the key results of this

work and propose future work on this topic of research.

# Preface

This thesis is original work by Kenny Van in collaboration with Professor Natalia Ivanova and Professor Craig Heinke at the University of Alberta. It is based substantially on the following papers: Van et al. (2019); Van and Ivanova (2019) and Van and Ivanova (2021).

Chapter 2 of this thesis contains text published as “Low-mass X-ray binaries: the effects of the magnetic braking prescription”, Van, K. X., Ivanova, N., & Heinke, C. O. 2019, MNRAS, 737483, 5595, doi: 10.1093/mnras/sty3489. In this work, I definitively show that the most commonly used magnetic braking prescription cannot effectively reproduce our sample of observed low-mass X-ray binaries (LMXBs). I derived the modified magnetic braking scheme, simulated the binaries, analysed the data and wrote the paper. N. Ivanova planned the project, supervised the work, and contributed to the writing of the paper. C. Heinke provided suggestions and edits to the paper.

Chapter 3 is work that has been published as “Evolving LMXBs: CARB Magnetic Braking”, Van, K. X., & Ivanova, N. 2019, ApJL, 886, L31,735, doi: 10.3847/2041-8213/ab571c. In this work I derive an improved magnetic braking scheme that more effectively accounts for convective turnover time and magnetized winds. I show that this improved magnetic braking scheme can effectively reproduce our sample of persistent LMXBs. I derived the improved magnetic braking scheme, simulated the binaries, analysed the data and wrote the paper. N. Ivanova planned the project, supervised the work, and contributed to the writing of the paper.

Chapter 4 of the thesis contains work submitted to APJ as “Constraining Progenitors of Observed LMXBs Using CARB Magnetic Braking”, Van, K.

X., & Ivanova, N. 2021. In this work I apply the improved magnetic braking scheme derived in Chapter 3 and use it to generate a large grid of simulated systems. I then use this simulated grid to compare it to observed persistent LMXBs to calculate progenitor rates. I simulated the binaries grid, analysed the data, calculated the rates and wrote the paper. N. Ivanova planned the project, supervised the work, and contributed to the writing of the paper.

Chapter 5 summarizes the conclusions from the two published works, “Low-mass X-ray binaries: the effects of the magnetic braking prescription”, Van, K. X., Ivanova, N., & Heinke, C. O. 2019, MNRAS, 737483, 5595, doi: 10.1093/mnras/sty3489, “Evolving LMXBs: CARB Magnetic Braking”, Van, K. X., & Ivanova, N. 2019, ApJL, 886, L31,735, doi: 10.3847/2041-8213/ab571c and the submitted work ‘Constraining Progenitors of Observed LMXBs Using CARB Magnetic Braking”, Van, K. X., & Ivanova, N. 2021.



# Acknowledgements

Acknowledgments here...

# Contents

<b>1</b>	<b>Introduction</b>	<b>1</b>
1.1	Low Mass X-ray Binaries . . . . .	1
1.2	Accretion in LMXBs . . . . .	2
1.2.1	Roche Lobe Overflow . . . . .	2
1.2.2	Mass Transfer Stability . . . . .	4
1.2.3	Mass Transfer Efficiency . . . . .	6
1.2.4	Eddington Limit . . . . .	7
1.3	Angular Momentum Loss Mechanisms . . . . .	8
1.3.1	Gravitational Radiation . . . . .	9
1.3.2	Mass Loss . . . . .	9
1.3.3	Magnetic Braking . . . . .	10
1.4	Simulating Binary Systems . . . . .	15
1.5	Objectives . . . . .	16
1.6	Methodology . . . . .	16
<b>2</b>	<b>Low Mass X-ray Binaries: The Effects of the Magnetic Braking Prescription</b>	<b>19</b>
2.1	Introduction . . . . .	20
2.2	Numerical Method . . . . .	22
2.2.1	Setting up and evolving the population of binaries . . . . .	22
2.2.2	Magnetic braking . . . . .	25
2.2.3	Verification against a previous study . . . . .	31

2.3	Observational Data for NS LMXBs . . . . .	33
2.4	Principal Results . . . . .	39
2.4.1	Evolutionary Tracks . . . . .	39
2.4.2	Binary Properties . . . . .	47
2.4.3	Relative Densities . . . . .	51
2.5	Comparison to the observed population of LMXBs . . . . .	52
2.5.1	Other effects . . . . .	59
2.6	Conclusions . . . . .	61
<b>3</b>	<b>Evolving LMXBs: CARB Magnetic Braking</b>	<b>64</b>
3.1	Introduction . . . . .	65
3.2	Magnetic Braking . . . . .	66
3.3	Evolution through the mass transfer . . . . .	68
3.4	Comparison with the observed population of LMXBs . . . . .	71
3.5	Conclusions . . . . .	76
<b>4</b>	<b>Constraining Progenitors of Observed LMXBs Using CARB Magnetic Braking</b>	<b>79</b>
4.1	Introduction . . . . .	80
4.2	Model . . . . .	82
4.2.1	Population Grid . . . . .	82
4.2.2	Magnetic Braking . . . . .	84
4.2.3	Accretion rate . . . . .	85
4.2.4	Persistent Systems . . . . .	87
4.2.5	Relating the observed LMXBs to the simulated LMXBs .	88
4.2.6	Progenitor search . . . . .	89
4.3	Analysis . . . . .	90
4.3.1	Ultra Compact Systems . . . . .	93
4.3.2	Short Period . . . . .	94
4.3.3	Medium Period . . . . .	96

4.3.4	Long Period . . . . .	98
4.3.5	Effective Temperature . . . . .	99
4.3.6	Wider Bins . . . . .	101
4.4	Rate Estimates . . . . .	104
4.4.1	UCXBs . . . . .	109
4.4.2	Short and Medium Period . . . . .	111
4.4.3	Long Period . . . . .	111
4.4.4	Combined Rates . . . . .	112
4.5	Unobserved Systems . . . . .	113
4.5.1	Region “A”: Short Initial Periods . . . . .	114
4.5.2	Region “B”: $M_i \sim 1.5M_\odot$ , $P_i \sim 1$ day . . . . .	116
4.5.3	Region “C”: $M_i \sim 2.0M_\odot$ , $P_i \lesssim 0.5$ days . . . . .	117
4.5.4	Region “D”: $M_i \sim 3.0M_\odot$ , $P_i \sim 1$ day . . . . .	118
4.5.5	Region “E”: $P_i \gtrsim 1.5$ days, $M_i \lesssim 3.0M_\odot$ . . . . .	121
4.5.6	Regions “F” and “G”: High Initial Mass . . . . .	121
4.5.7	Uniform Initial Parameter Space Hypothesis . . . . .	123
4.6	Conclusion . . . . .	124
<b>5</b>	<b>Conclusion</b>	<b>128</b>
5.1	Modified Skumanich . . . . .	128
5.2	CARB Magnetic Braking . . . . .	129
5.3	Future Work . . . . .	130
<b>A</b>	<b>Custom MESA Routines</b>	<b>132</b>
A.1	Implementation of Eddington Limit . . . . .	132
A.2	Boosted Skumanich Magnetic Braking . . . . .	133
A.3	CARB Magnetic Braking . . . . .	136
<b>B</b>	<b>Sample MESA inlist Files</b>	<b>143</b>
B.1	Boosted Skumanich Sample . . . . .	143

B.2 CARB MB Sample . . . . .	146
<b>C Black Hole Table</b>	<b>150</b>

# List of Tables

2.1	The different scaling values used in Equation 2.20 for the various cases. . . . .	31
2.2	Sco X-1 Test Properties . . . . .	33
2.3	Observed Neutron Star LMXBs . . . . .	37
2.4	Properties of Persistent LMXBs . . . . .	54
2.5	Properties of Transient LMXBs . . . . .	54
2.6	Maximum Lifetime of an Observed LMXB and Fraction of Parameter Space . . . . .	56
3.1	Binned Properties of LMXBs . . . . .	74
4.1	The grid sizes for mass and orbital periods for different ranges of initial donor masses and initial orbital periods. . . . .	82
4.2	Binned Properties of LMXBs . . . . .	89
4.3	Extended MT for Non-UCXBs . . . . .	101

4.4	The table shows the initial period and mass resulting in the minimum formation rate. The subscripts min and avg denote the minimum and average. The rate $\Gamma$ in units of systems per Gyr as calculated using equation 4.9. The period is the initial orbital period of the progenitor binary in $\log_{10}(\text{days})$ and the mass, $M_i$ , is the initial mass of the donor in $M_\odot$ . The two combined rows at the bottom shows the average minimum and maximum calculated formation rates when we randomly select a progenitor for our observed LMXBs. . . . .	107
4.5	A summary of the different regions of our parameter space and a summary of how observable a system from this region is. . . .	113
4.6	Possible LMXBs . . . . .	127
C.1	Observed Black Hole LMXBs . . . . .	151

# List of Figures

- 1.1 A schematic view of Roche lobes in the  $x - y$  plane. The system consists of a  $1.4M_{\odot}$  accretor and a  $1.0M_{\odot}$  donor with an initial orbital period of 2 days. The two different lines show two different surfaces of equal gravitational potential. . . . . 4
- 2.1 The results of the two models tested to verify our results to reproduce the observed system Sco X-1. The upper curve in the plot is the evolution using the modified MB, and the lower curve is the evolution using the default MB. The star on the plot represents the approximate location of Sco X-1 based on observations with the colour of the star corresponding to the observed mass transfer rate. The colour bar denotes the MT rate of the binary system with the observed MT of Sco X-1 observed as  $\log_{10}(M_{\odot}/\text{yr}^{-1}) \approx -7.7$ . The modified MB can reproduce the appropriate MT observed in Sco X-1 while the default MB cannot. 34

2.2 A collection of subplots showing the evolution through mass transfer for all initial periods, shown on the grid of initial donor masses and mass ratios. The data shown is only after the onset of RLOF with the colour bar indicating $\log_{10}(MT)$ . The evolutionary tracks evolve from the right of the subplots leftwards as the donor loses mass through mass transfer. At higher donor masses and low periods, there exist a subset of systems which abruptly terminate their tracks as they begin to transfer mass dynamically. The points on the plot represent observable systems, with errors found in Table 2.3. Circles are transient systems, and triangles are persistent systems. The single star point is the binary Sco X-1 used to test the validity of our numeric results. The range of periods in each plot is the same, but the range of donor masses differs. The abrupt cutoff at higher periods is a result of the star reaching the end of its life. . . . .	41
2.3 A similar figure to 2.2 using case 2, convection boosted MB from Table 2.1. The general behaviour of these simulated systems is similar to that of the systems following the Skumanich law, in Fig. 2.2. . . . .	42
2.4 A similar figure to 2.2 using case 3, intermediate MB from Table 2.1. Note that the mass transfer rates are substantially higher than in the previous cases, Figs. 2.2 and 2.3. . . . .	43
2.5 A similar figure to 2.2 using case 4, wind boost MB from Table 2.1. Here the mass transfer rates are extremely high. . . . .	44

2.6	A figure showing the evolutionary tracks of a binary system consisting of a $1.2M_{\odot}$ initial mass donor with a $1.4M_{\odot}$ NS at a variety of initial periods using the wind boosted MB. The colour bar shows the magnetic field strength of the donor star at a given point in the binary evolution. The magnetic field is given in units of the solar magnetic field, which is $\sim 1\text{G}$ . . . . .	46
2.7	A scatter plot showing the changes in NS mass during the evolution of our systems. The lower hashed area shows the periods corresponding to ultra compact sources. The default and convection boosted cases suggest that all short period binaries contain a massive NS. . . . .	48
2.8	The surface C/N abundance mass fraction of the donor star. The initial C/N ratio of a star is $\sim 3.36$ or $\sim 0.53$ on the log scale.	49
2.9	The surface N/O abundance mass fraction of the donor star. The initial N/O ratio of a star is 0.108 or $\sim -0.96$ on the log scale.	50
2.10	The relative probability of finding a system at a given point in our parameter space, assuming a the initial distribution of binaries from section 2.2.1. The symbols on the plot represent the observed systems with their given errors (see Table 2.3). Circles are transient systems and triangles are persistent systems. The single star point is the binary Sco X-1. The two grey dashed lines represent the critical MT rates for thermal-viscous accretion stability using an NS mass of $1.4M_{\odot}$ (Coriat et al., 2012). These two lines are denoted with “DIM non irr” for the critical MT rate without the effects of irradiation while “DIM irr” is the critical MT rate with the effects of irradiation. Binaries that lie above the line are predicted to be persistent LMXBs while systems below are transient. The left hashed area represents the period range for ultra-compact sources. . . . .	53

3.1	The evolution of $M_{\text{NS}}$ during the mass transfer. The $\eta$ value denotes the MT efficiency. The triangle symbols represent persistent LMXBs (data from Van et al., 2019). . . . .	69
3.2	The relative probability of finding a system in a given bin in period-MT space. Each bin spans a width and height of 0.1 in $\log_{10}(P)$ and $\log_{10}(\dot{M}_{\text{acc}})$ . The symbols used are the same as in figure 3.1. The two grey dashed lines represent the critical MT separating persistent and transient systems for $M_{\text{NS}} = 1.4M_{\odot}$ as described by the disk instability model (DIM) (Coriat et al., 2012). The upper line includes the effects of irradiation while the lower line does not. . . . .	72
4.1	The progenitors of the observed LMXBs split into distinct classes based on the periods of the currently observed systems as denoted in Table 4.2. Some observed systems share common progenitors, to show this, the individual grid points are semitransparent. The black dashed line denotes the shortest initial period with which the initial binary would start as a detached system. The red dashed line denotes the shortest initial period which the detached binary can have when the progenitor is 10 million years old. The systems on the left of the black dashed line started their evolution while having an initial Roche lobe overflow. . . . .	91
4.2	The progenitors of the four types of the observed LMXB. The colour shows $f_{\text{obs},i}$ , the fraction of time the modelled system shows up as one of the observed LMXB, as compared to the time it can be observed as any persistent LMXB, see Equation 4.7). The black and the red dashed lines are as in Figure 4.1. . .	92

4.3	The short period systems from Figure 4.2 split into the individual systems. The colour shows $f_{\text{obs}}$ , the fraction of time the modelled system shows up as one of the observed LMXB, as compared to the time it can be observed as any persistent LMXB. The black and the red dashed lines are as in Figure 4.1. . . . .	97
4.4	The ratio between observed and persistent times of the two medium period LMXBs. Similar to Figure 4.1, the black and red dashed lines show the shortest period where an initial binary would start as a detached system and the shortest initial period which the detached binary can have when the progenitor is 10 million years old respectively. . . . .	98
4.5	The progenitors of Sco X-1 and Cyg X-2 when the effective temperature is excluded in black and included in red. The black and red dashed lines are identical to those in Figure 4.1. . . . .	100
4.6	A similar figure to Figure 4.1 but using the wider bins for the observable quantities. The red and black dashed lines are the same as those described in Figure 4.1. . . . .	102
4.7	A sample of the high mass progenitors of UCXB systems found when using the wider bins. The red squares show the locations of the observed LMXBs using the wider bins. The colour bar shows the mass transferred $\dot{M}_{\text{tr}}$ . . . . .	103
4.8	A sample of the low mass progenitors of UCXB systems found when using the wider bins. The red squares and colour bar are the same as in Figure 4.7. . . . .	105
4.9	The minimum formation rate of the observed LMXBs, (see Equation 4.9). The labelled sections in the plot denote specific regions of the parameter space where the simulations do not overlap with any observed LMXBs. . . . .	106

4.10 A subset of simulated systems with a short initial period, $P_i \lesssim$ 0.5 days. The color of the lines indicates the mass transfer rate of a given simulation at that point. The red boxes show the mass ratio and period bins of the four observed short period LMXBs in Table 4.2. The black points show portions of the evolution where the binary does not experience RLOF. . . . .	115
4.11 A subset of simulated systems from the region denoted as "B" in Figure 4.9. . . . .	117
4.12 A subset of simulated systems from the region denoted as "C" in Figure 4.9. The red boxes show the bins for the UCXB and short period observed binaries. . . . .	119
4.13 A subset of simulated systems from the region denoted as "D" in Figure 4.9. The red boxes show the bins for the UCXB and short period observed binaries. . . . .	120
4.14 A subset of our parameters space such that the progenitor bina- ries have initial periods longer than 1.5 days and initial masses less than $3.0M_\odot$ (region "E"). The red boxes show the mass ra- tio and periods of the two observed medium period LMXBs in Table 4.2. . . . .	122
4.15 A subset of simulated systems with the initial donor masses ex- ceeding at least $3.5M_\odot$ , and more massive than Cygnus X-2 pro- genitors for each given initial orbital period. . . . .	123

# Chapter 1

## Introduction

### 1.1 Low Mass X-ray Binaries

A binary system consists of two stars gravitationally bound to each other orbiting about a centre of mass. These systems were initially proposed by Michell (1767) and introduced in a catalogue by Herschel (1802). While binary systems have been studied for over 200 years, only recently, with advancements in observational techniques and modelling tools, has the understanding of stellar and binary evolution drastically increased. Understanding binary systems is paramount in understanding stellar evolution with stellar multiples being common (Abt and Levy, 1976; Abt, 1983; Mason et al., 2009; Sana and Evans, 2011; Chini et al., 2012; Almeida et al., 2017) and a significant fraction of massive stars experiencing mass transfer (MT) at some point during their lifetime, drastically impacting their evolution (Sana et al., 2012).

Binary interactions are often postulated to be a mechanism in producing exotic signals or stellar systems. In many cases, exotic binary systems such as the compact binary systems detected by the Laser Interferometer Gravitational-Wave Observatory (LIGO), MT is necessary to explain the production and evolution of the system (The LIGO Scientific Collaboration et al., 2019, 2020a,b). Of particular interest here are low mass X-ray binaries (LMXBs) which are

systems consisting of a compact object such as a black hole (BH) or a neutron star (NS), accreting material from a donor star.

## 1.2 Accretion in LMXBs

In LMXBs, X-ray radiation is produced when material is accreted onto the compact object. Based on the configuration of the system such as the type of compact object and binary separation, the material accreted can be a result of stellar winds or due to MT through  $L_1$  neighbourhood, the process that is known as Roche Lobe overflow (RLOF). Wind MT occurs when the companion loses material through stellar winds and the compact object accretes this material. This method of mass transfer normally occurs in binaries with a black hole and a high mass donor. RLOF, on the other hand, occurs when the radius of the donor star exceeds the region where material remains gravitationally bound to it. When this occurs, material may flow from the donor to the accretor. In this work where I focus on NS LMXBs, RLOF will be the only mechanism of MT used in this work.

### 1.2.1 Roche Lobe Overflow

The Roche lobe of a star is the region around a star where material is gravitationally bound to that star. The effective gravitational potential of a binary system assuming a circular orbit, constant angular velocity and in the corotation frame is given by the following equation (Eggleton, 2006):

$$\Phi_R(x, y, z) = -\frac{GM_d}{\sqrt{\left[x + \left(\frac{M_a}{M}\right)a\right]^2 + y^2 + z^2}} - \frac{GM_a}{\sqrt{\left[x - \left(\frac{M_d}{M}\right)a\right]^2 + y^2 + z^2}} - \frac{GM}{2a^3}(x^2 + y^2), \quad (1.1)$$

Here  $G$  is the gravitational constant,  $M_a$  and  $M_d$  denotes the mass of the accretor and donor respectively.  $M = M_a + M_d$  is the combined mass of the

binary and  $a$  is the binary separation. Equation 1.1 is in Cartesian coordinates with the origin at the center of mass of the binary. A graphical representation of the Roche potential in the  $x - y$  plane is shown in Figure 1.1 showing a surface of equipotential and the  $L_1$  Lagrange point. The  $L_1$  Lagrange point is the first intersection between the effective potentials of the donor and accretor and is the location of mass transfer when RLOF occurs. Depending on which star fills their respective Roche lobe, there are three different classes of binary system as described in Kopal (1955):

1. Detached Systems: Neither star has filled their Roche lobe and the stars are primarily interacting gravitationally. The stars may still transfer material through winds but no material should be transferred through RLOF.
2. Semi-Detached Systems: One of the two stars have filled their Roche lobe and RLOF is occurring. The donor star is transferring mass through the  $L_1$  Lagrange point to the accretor.
3. Contact Systems: Both stars have filled their respective Roche lobes and the stars are in physical contact with one another.

In this work I focus on semi-detached systems where a donor star will be transferring mass to a neutron star.

While Equation 1.1 describes the surface of effective gravitational potential, the volume-equivalent radius of the Roche lobe that crosses the  $L_1$  Lagrange point was approximated in 1D by Eggleton et al. (1973) as

$$\frac{R_{\text{RL}}}{a} \approx \frac{0.49q^{2/3}}{0.6q^{2/3} + \ln(1 + q^{1/3})}, \quad (1.2)$$

where  $R_{\text{RL}}$  is the Roche lobe radius,  $q$  is the ratio of the donor mass to the accretor mass  $M_d/M_a$  and  $a$  is the binary separation. I will be using subscripts  $d$  and  $a$  to denote the donor and accretor respectively throughout this work.

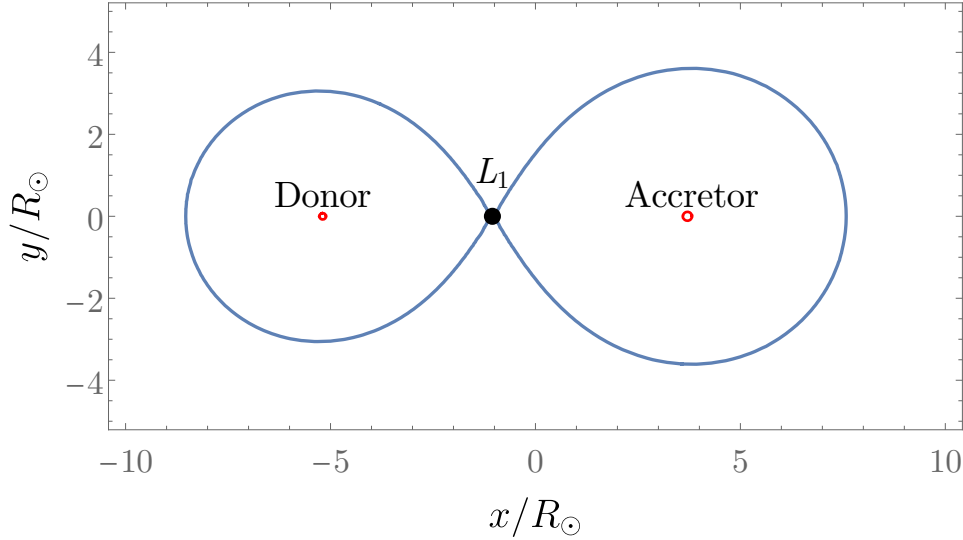


Figure 1.1: A schematic view of Roche lobes in the  $x - y$  plane. The system consists of a  $1.4M_{\odot}$  accretor and a  $1.0M_{\odot}$  donor with an initial orbital period of 2 days. The two different lines show two different surfaces of equal gravitational potential.

### 1.2.2 Mass Transfer Stability

After mass transfer starts, the lifetime and stability of this process is directly related to the timescale over which it occurs. Depending on how the donor, the accretor and the Roche lobe change due to mass transfer, the mass transfer can occur over different timescales (Hjellming and Webbink, 1987; Soberman et al., 1997). The timescale of mass transfer is defined by three mass-radius relations, these quantities represent the response of the star's radius to mass loss:

$$\xi_{\text{eq}} = \left( \frac{d \ln R}{d \ln M} \right)_{\text{eq}}, \xi_{\text{RL}} = \left( \frac{d \ln R}{d \ln M} \right)_{\text{RL}}, \xi_{\text{ad}} = \left( \frac{d \ln R}{d \ln M} \right)_{\text{ad}}. \quad (1.3)$$

These relations define the mass-radius relations of stars in thermal equilibrium, the Roche lobe, and for a star losing mass adiabatically. Inequalities between these three relations define the timescale and type of mass transfer occurring in a binary system.

1. Stable Mass Transfer ( $\xi_{\text{RL}} \leq \xi_{\text{eq}}$ ): The donor star remains in thermal

equilibrium through mass transfer. RLOF is driven by the nuclear evolution of the donor which expands its radius and occurs on the nuclear timescale. For a main sequence star burning hydrogen, this timescale can be given by:

$$\tau_{\text{nuc}} \approx 0.007 \frac{M_{\text{core}} c^2}{L} \approx 10^{10} \frac{M}{M_{\odot}} \frac{L_{\odot}}{L} \text{ yrs.} \quad (1.4)$$

2. Thermal Timescale Mass Transfer ( $\xi_{\text{eq}} < \xi_{\text{RL}} \leq \xi_{\text{ad}}$ ): Mass transfer in this regime remains stable and is driven by the thermal readjustment of the donor star. While the star is no longer in thermal equilibrium, mass transfer is still stable and self regulating. In thermal timescale mass transfer, the mass transfer will saturate at a value regulated by the thermal timescale of the donor

$$\dot{M}_{\text{max}} \approx -\frac{M_d}{\tau_{\text{KH}}}, \quad (1.5)$$

with  $\tau_{\text{KH}}$  being the thermal or Kelvin-Helmholtz time scale:

$$\tau_{\text{KH}} = \frac{E_{\text{therm}}}{L} \approx \frac{GM^2}{2RL} \approx 1.5 \times 10^7 \left( \frac{M}{M_{\odot}} \right)^2 \frac{R_{\odot}}{R} \frac{L_{\odot}}{L} \text{ yrs.} \quad (1.6)$$

If the mass transfer rate is lower than  $\dot{M}_{\text{max}}$  then the donor star will expand and increase the mass transfer rate. If the mass transfer rate is initially larger than  $\dot{M}_{\text{max}}$  then the donor star shrinks and suppresses the mass transfer rate.

3. Dynamically Unstable Mass Transfer ( $\xi_{\text{ad}} < \xi_{\text{RL}}$ ): Dynamically unstable mass transfer occurs when the donor star cannot readjust quickly enough to keep the star within its Roche Lobe. Depending on the entropy profile of the star, it is possible that the donor star will expand as it loses mass (Woods and Ivanova, 2011; Pavlovskii and Ivanova, 2015). In this scenario, the radius expands with mass loss causing the mass transfer rate to grow resulting in a runaway effect. Systems with very high mass

transfers may even lose mass through other Lagrange points resulting in a common envelope event (see Ivanova et al., 2013; Ivanova and Nandez, 2016, for more information on common envelope events).

These three types of mass transfer timescales can generally describe the different types of RLOF a binary system may undergo. It is possible for binary systems that initially experience stable mass transfer to increase and later experience dynamically unstable mass transfer (Webbink et al., 1983; Hjellming and Webbink, 1987). This delayed unstable mass transfer occurs when the mass transfer is initially stable, but due to mass loss, it is possible to expose a region of the star where the entropy increases with increasing mass. These regions respond to mass loss by expanding outwards leading to runaway mass transfer. Numerically simulating these processes is complex and numerically intensive. In this work we use Modules for Experiments in Stellar Astrophysics (**MESA**) numeric code. **MESA** is a very robust code that uses advanced techniques to avoid crashing. The **MESA** code will reduce a simulations time step when the system encounters physically complex situations. If the time steps get too small, the **MESA** simulation will end stopping the stellar evolution prior to the user defined stopping condition. In binary systems, this can occur even at thermal timescale mass transfer if the donor star enters a physically complex phase of its evolution. My research focuses on stable and thermal timescale mass transfer in long living LMXBs.

### 1.2.3 Mass Transfer Efficiency

Once RLOF occurs and material flows from the donor through the  $L_1$  Lagrange point, a fraction of the mass may be deflected away from the accretor resulting in less mass accreted. The fraction of the material lost from the donor and is accreted by the compact object is known as the MT efficiency. An analytic description of the MT efficiency is not known but in the context of NSs, there is

observational evidence that a significant amount of the mass lost by the donor isn't accreted (Antoniadis et al., 2012, 2016). Additionally, a fraction of the material accreted onto the neutron star is also converted to binding energy further reducing the efficiency. Depending on the equation of state used to describe the neutron star, this value can also vary between  $f_{\text{BE}} \approx 0.85 - 0.90$  (Lattimer and Prakash, 2007). The exact value that I employ in my stellar simulations will be described in the respective chapters.

#### 1.2.4 Eddington Limit

A well established upper limit on the mass accretion rate is the Eddington limit. The Eddington limit is the maximum luminosity a star can have before the radiation pressure exceeds the gravitational force pulling the material inwards. With luminosity directly related to the mass accretion rate, it can be shown that the Eddington limit sets an upper limit to accretion as well. If the accretion rate  $\dot{M}_d$  exceeds the Eddington-limited MT rate  $\dot{M}_{\text{Edd}}$ , the excess  $\dot{M}_d - \dot{M}_{\text{Edd}}$  cannot be accreted on to the compact object, and is lost from the system. For the Eddington limited MT rate on a NS I use,

$$\begin{aligned}\dot{M}_{\text{Edd}} &= \frac{4\pi c R_a}{\kappa_e} \\ &\approx \frac{3.4}{1+X} \times 10^{-8} M_{\odot} \text{ yr}^{-1}.\end{aligned}\tag{1.7}$$

$R_a$  is the radius of the accretor,  $\kappa_e$  is the opacity due to Thomson electron scattering,  $\kappa_e = 0.2(X + 1) \text{ cm}^2 \text{ g}^{-1}$ , where  $X$  is the hydrogen mass fraction in the material transferred from the donor. It is important to note that Equation 1.7 assumes spherical symmetry and in reality, some systems exceed the Eddington limit resulting in ultra-luminous X-ray sources (Colbert and Mushotzky, 1999). One well known ULX with a NS accretor is M82 X-2 which had an observed luminosity of  $\approx 1.8 \times 10^{40} \text{ erg s}^{-1}$  (Bachetti et al., 2014). This source is ob-

served to have a mass accretion rate approximately two orders of magnitude larger than the Eddington limit predicted in Equation 1.7. The NS in M82 X-2 is predicted to have a moderately strong magnetic field which would suppress the opacity. With a lower opacity, the Eddington limit would increase to sufficiently high values to explain the luminosity observed for this system (Karino and Miller, 2016).

### 1.3 Angular Momentum Loss Mechanisms

During the evolution of a neutron star LMXB, MT would only occur if the donor star overfills its Roche lobe,  $R_{\text{RL}} \leq R_d$ . For this to occur, either the radius of the donor must increase or the Roche lobe must shrink. From Equation 1.2 we see that before RLOF,  $q$  should remain largely constant as the mass of the stars is only affected by wind mass loss. Stellar winds do not play a significant role on the masses of stars during the main sequence if these stars are intermediate or low-mass stars. This implies that in LMXBs, where the donor star is on the main sequence and it is not massive, the start of RLOF is only dependant on the evolution of the orbital separation due to the orbital angular momentum loss. The angular momentum of a binary system is related to the masses and the binary separation through the following equation

$$J^2 = G \frac{M_d^2 M_a^2}{M_d + M_a} a(1 - e^2). \quad (1.8)$$

The change in orbital separation can then be given by

$$\frac{\dot{J}}{J} = \frac{\dot{a}}{a} + 2\frac{\dot{M}_d}{M_d} + 2\frac{\dot{M}_a}{M_a} - \frac{\dot{M}_d + \dot{M}_a}{M_d + M_a} - 2\frac{\dot{e}e}{1 - e^2}. \quad (1.9)$$

Here  $J$  is the angular momentum,  $e$  is the orbital eccentricity and the other variables are the same as those defined above. Prior to RLOF, the primary mechanism to shrink the binary separation is through the loss of angular mo-

mentum. The angular momentum of a binary system is lost through gravitational radiation, mass lost from the system or via magnetic braking.

### 1.3.1 Gravitational Radiation

Among the angular loss mechanisms, gravitational radiation is the most well understood and predictable. Gravitational radiation is the process where angular momentum is lost through the production of gravitational waves. The historic example of gravitational radiation is the Hulse-Taylor binary (Weisberg and Huang, 2016) with more recent examples of gravitational waves detected by LIGO (The LIGO Scientific Collaboration et al., 2019, 2020a,b). Assuming a circular orbit, the loss of angular momentum through gravitational radiation is given by (Faulkner, 1971; Kraft et al., 1962; Landau and Lifshitz, 1975)

$$\dot{J}_{\text{GR}} = -\frac{32}{5c^5} \left( \frac{2\pi G}{P} \right)^{7/3} \frac{(M_d M_a)^2}{(M_d + M_a)^{2/3}}. \quad (1.10)$$

Here  $P$  is the orbital period of the binary. Gravitational radiation is more important for short period, high mass binary systems as seen in Equation 1.10. In the case of NS LMXBs, the effects of gravitational radiation are overshadowed by magnetic braking or mass loss until the periods are on the order of hours.

### 1.3.2 Mass Loss

As explained in Section 1.2, there is clear observational evidence that the NS in LMXBs does not accrete all of the material lost from the donor star. In addition to possible stellar winds, the mass lost from inefficient MT will carry angular momentum away from the binary. Any material lost through winds will carry the specific angular momentum of the star where the wind originated. The material that is lost from the system due to inefficient mass transfer or the Eddington limit will carry specific angular momentum of the accretor. Angular

momentum loss due to mass loss can be described by:

$$\dot{J}_{\text{ML}} = \dot{M}_{d,\text{loss}} \left( \frac{M_a}{M_d + M_a} a \right)^2 \Omega + \dot{M}_{a,\text{loss}} \left( \frac{M_d}{M_d + M_a} a \right)^2 \Omega \quad (1.11)$$

Here  $\dot{M}_{d,\text{loss}}$  and  $\dot{M}_{a,\text{loss}}$  denote the mass loss from the donor or accretor that does not remain in the system respectively. In general, this mechanism of angular momentum loss is less well understood than gravitational radiation due to uncertainties in wind mass loss rates and MT efficiency. Both mass transfer efficiency and wind mass loss rates are topics of ongoing research (Antoniadis et al., 2012, 2016; Renzo et al., 2017). The strength of this mechanism depends entirely on the amount of mass lost from the system which is an area of ongoing research. In LMXBs with an initially non-massive main sequence donor, mass loss from the systems would not be significant until RLOF occurs as the wind mass loss rate in these types of stars is relatively small.

### 1.3.3 Magnetic Braking

The loss of angular momentum with gravitational radiation operates primarily in short-period systems. At the same time, unless one of the stars loses lots of mass through winds while widening the system, the angular momentum loss through mass loss only plays a significant role once RLOF begins. In relatively wide non-mass transferring systems with intermediate or low-mass donors, the dominant mechanism of angular momentum loss that lead to the shrinkage of the orbital separation is different, and is known as magnetic braking. Magnetic braking is the process where material remains locked in corotation with the star's surface out to large radii due to the magnetic field. Since the radius to which the matter is in corotation is substantially larger than the star's radius, the amount of angular momentum lost can be appreciable, despite the amount of the mass loss being small. Magnetic braking is the main angular momentum

loss mechanism for NS LMXBs with large periods prior to RLOF.

Unfortunately, unlike gravitational radiation that was derived from first principles (Kraft et al., 1962; Landau and Lifshitz, 1975), no such analytic solution to magnetic braking exists. The physical description of magnetic braking depends on the magnetic field geometry, the type of wind from the star and the relation between the magnetic field strength and the physical properties of the star (Weber and Davis, 1967; Mestel, 1968; Mestel and Spruit, 1987). The angular momentum is lost through magnetic braking when material leaves the system through the Alfvèn surface. The Alfvèn surface represents the maximum radius where the material remains locked in corotation with the star. Beyond this value, the ram pressure pushing the material out of the system exceeds the magnetic pressure binding the material to the system (Mestel, 1968; Mestel and Spruit, 1987):

$$\frac{1}{2}\rho_A v_A^2 \simeq \frac{B(r)^2}{8\pi}. \quad (1.12)$$

$\rho_A$  and  $v_A$  are the density and velocity of the material at the Alfvèn surface.  $B(r)$  describes the magnetic field strength as a function of radius. In the simplest case,  $B(r)$  can represent a radial magnetic field given by:

$$B(r) = B_s \frac{R_s^2}{r^2}. \quad (1.13)$$

The subscript  $s$  denotes the value of that variable at the surface of the star. This gives a mathematical description of an Alfvèn surface in a system with a radial magnetic field:

$$4\pi R_A^4 \rho_A v_A^2 = B_s^2 R_s^4, \quad (1.14)$$

Assuming an isotropic wind and enforcing mass continuity, the wind mass loss rate is:

$$\begin{aligned}\dot{M}_W &= 4\pi R^2 \rho_s v_s, \\ &= 4\pi R_A^2 \rho_A v_A,\end{aligned}\tag{1.15}$$

By combining Equations 1.14 and 1.15, the radius of the Alfvèn surface is:

$$R_A^2 = \frac{B_s^2 R^4}{\dot{M}_W v_A}.\tag{1.16}$$

The amount of angular momentum lost through an isotropic wind leaving a spherically symmetric Alfvèn surface can be given by:

$$\begin{aligned}\dot{J}_{MB} &= -4\pi \Omega \int_0^{\pi/2} \rho_A v_A R_A^2 (R_A \sin \theta)^2 \sin \theta d\theta \\ &\simeq -\frac{8}{3} \pi \Omega \rho_A v_A R_A^4, \\ &\simeq -\frac{2}{3} \Omega \dot{M}_W R_A^2, \\ &\propto \Omega B_s^2 R_s^4\end{aligned}\tag{1.17}$$

The surface magnetic field strength can be related to other physical properties of the star through the Rossby number (Parker, 1971; Noyes et al., 1984; Ivanova, 2006). These relations allows for the following equation:

$$\begin{aligned}\frac{B_s}{B_{s,\odot}} &= \frac{R_0}{R_{0,\odot}}, \\ \frac{B_s}{B_{s,\odot}} &= \frac{\Omega}{\Omega_\odot} \frac{\tau_{\text{conv}}}{\tau_{\odot \text{conv}}}.\end{aligned}\tag{1.18}$$

Combining Equations 1.17 and 1.18 gives

$$\dot{J}_{MB} \propto R^4 \Omega^3.\tag{1.19}$$

Assuming a radial magnetic field and isothermal winds results in an equation for magnetic braking that has the same functional dependence as the well-known “Skumanich” prescription, which is to the date is the most commonly used parameterization of magnetic braking. This empirical prescription was originally built on the observation that the equatorial spin of slowly rotating, G-type main sequence stars decreases with age (Skumanich, 1972).

$$v_e \approx f \times 10^{14} t_0^{-1/2} \text{ cm s}^{-1}. \quad (1.20)$$

$v_e$  is the equatorial rotation speed,  $f$  is a constant that ranges from  $0.73 - 1.78$ , and  $t_0$  is the amount of time the star has spent on the main sequence. Verbunt and Zwaan (1981) used the relationship between the age of the star and its equatorial spin to derive a magnetic braking prescription.

$$\dot{J} = -5 \times 10^{-29} f^{-2} M_d R_d^4 \Omega^3. \quad (1.21)$$

While the functional dependence can be explained by the specific choice of the magnetic field geometry and wind properties, the calibration constant comes from the empirical comparison between observations of slowly rotating solar-type stars and theoretical stellar models. It is worth mentioning that both the functional dependence and the calibration constant were derived for the case of low-mass main-sequence slowly rotating stars. The initial rotation for rapidly rotating stars in this prescription does not affect the outcome much.

Rappaport et al. (1983) found significant uncertainties in applying this prescription to binary systems and further parameterized the equation to its most commonly seen form:

$$\dot{J}_{\text{MB, sk}} = -3.8 \times 10^{-30} M_d R_d^4 \left( \frac{R_d}{R_\odot} \right)^{\gamma_{\text{MB}}} \Omega^3 \text{ dyne cm.} \quad (1.22)$$

Here  $\Omega$  is the angular velocity of the donor star in units of  $s^{-1}$  and  $\gamma_{MB}$  is a dimensionless parameter commonly ranging from 0-4 with  $\gamma_{MB} = 4$  corresponding to the Skumanich scaling for Equation 1.22. While this is the most common magnetic braking prescription, this does not mean the equation effectively models the magnetic braking for all systems. It has been shown that numerical studies of LMXBs using the Skumanich prescription result in calculated MT rates that differ from observation by up to an order of magnitude (Podsiadlowski et al., 2002).

These discrepancies in the Skumanich prescription have led to different research groups applying different assumptions and improvements in deriving many different magnetic braking schemes. Justham et al. (2006) assumes a dipolar magnetic field and an irradiation driven wind to derive a magnetic braking scheme for Ap/Bp donor stars in a binary system. Other studies such as Ivanova (2006) have also assumed a dipolar field but in that work, they relate the magnetic field strength of the donor to internal properties such as the turnover time in pre-main sequence stars. More recently, Pavlovskii and Ivanova (2016) tested both radial and dipolar magnetic fields with isothermal winds and varied the strength of the magnetic field with convective turnover time. Pavlovskii and Ivanova (2016) applied this magnetic braking scheme to reproduce the well studied LMXB, Sco X-1. With such dramatically different stellar systems, it is uncertain if these magnetic braking prescriptions will effectively reproduce binaries beyond what they were designed for. This work focuses on improving the currently used magnetic braking prescription by using a more physically motivated derivation and using the improved prescription to reproduce observed LMXBs with a wide range of observed properties.

## 1.4 Simulating Binary Systems

Depending on the initial configuration of the binary system, a wide range of possible exotic systems can be produced. With additional complications in the physics during evolution, there are a significant number of uncertainties in modelling and studying both binary and isolated systems. However, due to the wide gamut of exotic stellar systems that are a result of binary interactions, studies in the field of stellar evolution have led to significant advancements in numerical models of these systems. X-ray binaries in general have been used as laboratories for theorists to test and verify stellar models using numerical simulations (Faulkner, 1971; Rappaport et al., 1983; Webbink et al., 1983; Joss and Rappaport, 1984; Podsiadlowski et al., 2002; Justham et al., 2006).

In regards to simulating LMXBs, there are two different approaches for gaining insight into these systems using numerical simulations. One approach is to study a well documented observed system and generalize the theories to other binaries (Eggleton, 1983; Justham et al., 2006; Pavlovskii and Ivanova, 2016; Podsiadlowski and Rappaport, 2000; Verbunt and Zwaan, 1981). The other approach is to employ a technique known as population synthesis where a set of initial assumptions is applied to a large number of stellar systems in the parameter space of interest. The results of population synthesis are commonly used to generate statistical properties of those stellar systems (Fragos et al., 2008; Kalogera and Webbink, 1998; Kobulnicky and Fryer, 2007; Rappaport et al., 2005) or generate formation rates of exotic stellar systems using different initial conditions (Belczynski et al., 2018, 2020; Bruzual and Charlot, 2003). In this work, I employ a reverse population synthesis technique where we infer initial progenitor properties using our simulated results.

## 1.5 Objectives

The objectives of this research are to demonstrate the ineffectiveness of the Skumanich magnetic braking scheme and to derive an improved prescription. This will be done using Modules for Experiments in Stellar Astrophysics (**MESA**) (Paxton et al., 2011, 2013, 2015, 2018, 2019), a commonly used 1D stellar evolution code where I can easily test the magnetic braking prescriptions in a parameter space search. The main goals of these simulations are the following:

1. Clearly show that the default Skumanich magnetic braking scheme cannot effectively reproduce a well studied sample of observed LMXBs.
2. Demonstrate that the convection and rotation boosted (CARB) magnetic braking prescription derived using advancements in the understanding of the Alfvèn radius and the effects of convection on the magnetic field.
3. Using the CARB prescription, simulate a comprehensive grid of binary systems to calculate progenitor formation rates of observed persistent LMXBs.

## 1.6 Methodology

To determine if a magnetic braking scheme is effective, I need to perform a comprehensive parameter space search to conclusively show if the prescription can or cannot reproduce observed LMXBs. This requires a large number of simulated systems to ensure that complete coverage of relevant properties is done. While there are different numerical approaches to stellar simulations, this work uses a 1D grid based numerical code **MESA**. 1D stellar evolution codes assume spherical symmetry and can be less physically accurate than higher dimensional codes. 1D codes require significantly less computing power and because this work focuses on the broad effects that differences in magnetic

braking have on the evolution of a binary system, the use of a 1D stellar code like **MESA** is the best balance between computational cost and accuracy.

The **MESA** stellar evolution code is a robust, well documented and easily modifiable stellar evolution code. Throughout this work I use version 10398 in Chapter 2 and version 11701 in Chapters 3 and 4. A **MESA** simulation requires the user to define a variety of initial conditions such as initial donor mass and binary period, the two properties that I explore in the parameter space search. The exact details of the **MESA** options used will be presented in Chapters 2, 3 and 4 with an example in Appendix B. With the modular implementation of **MESA**, a user can easily make modifications or additions to the included physics in the code. This allows me to easily include the Eddington limit as described in Equation 1.7 and implement any modified magnetic braking prescriptions. These implementations are shown in Appendix A.

In this work, I generate a grid of simulated binaries that represents a reasonable range of initial periods and donor masses using the different magnetic braking schemes presented. After generating the simulated results, the simulated systems are compared to well studied observed LMXBs to determine if the observed systems can be reproduced using a given magnetic braking scheme. I focus on the mass ratio, period, and mass transfer rates of the LMXBs when making this comparison. By drawing cuboids using these three observed properties and their errors, I can determine if an observed LMXB can be reproduced by the magnetic braking prescription used and how long lived these simulated LMXBs are. This is primarily done in Chapters 2 and 3 where I derive improved magnetic braking prescriptions and test their effectiveness.

In Chapter 4 I employ what I call *reverse population synthesis*. Standard population synthesis techniques apply initial assumptions to produce a large population of stellar systems. The results of this technique are often used to predict expected populations of stellar objects. In the reverse case, I make no initial assumptions to the distribution of systems and instead use the results to

infer the initial conditions. After the grid of simulated results is produced using the improved magnetic braking scheme, I use this technique to calculate the progenitor formation rate. Another result of producing a comprehensive grid of simulated LMXBs is being able to find structure in the viable progenitors in the observed systems as well as determining gaps in where we expect to find more observable systems.

In summary, throughout this work, I will be deriving improved magnetic braking schemes and applying them to large grids of binaries with a wide range of initial donor masses and binary periods to generate a comprehensive grid of results. I will then compare this grid of simulated systems to observed LMXBs to test the effectiveness of a prescription. Chapter 2 will contain a comprehensive list of LMXBs and define our criteria for systems used to comparison to the simulated results. I will also briefly describe the conditions for what is considered a persistent or transient LMXB in this Chapter. In Chapter 2 I derive the first modified magnetic braking scheme which applies additional scaling factors to the Skumanich prescription and present the results using this model. Chapter 3 will contain the derivation of my convection and rotation boosted (CARB) magnetic braking prescription and the initial tests on our sample of observed LMXBs. In Chapter 4 I will apply the CARB magnetic braking scheme to a comprehensive grid of initial masses and periods to calculate possible progenitor production rates using the reverse population synthesis technique. Finally, Chapter 5 will summarize my results and present future considerations and prospects using the improved magnetic braking prescriptions.

## Chapter 2

# Low Mass X-ray Binaries: The Effects of the Magnetic Braking Prescription

K. X. Van<sup>1,\*</sup>, N. Ivanova<sup>1</sup>, C.O. Heinke<sup>1</sup>

<sup>1</sup>University of Alberta, Dept. of Physics, 11322-89 Ave, T6G 2E7, Canada

\* E-mail: kvan@ualberta.ca

*Accepted 2018 December 19. Received 2018 December 19; in original form 2018*

*October 15*

DOI: 10.1093/mnras/sty3489

## ABSTRACT

We present a population study of low- and intermediate-mass X-ray binaries (LMXBs) with neutron star accretors, performed using the detailed 1D stellar evolution code **MESA**. We identify all plausible Roche-lobe overflowing binaries at the start of mass transfer, and compare our theoretical mass transfer tracks to the population of well-studied Milky Way LMXBs. The mass-transferring evolution depends on the accepted magnetic braking (MB) law for angular momentum loss. The most common MB prescription ("Skumanich MB") originated from observations of the time-dependence of rotational braking of Sun-

type stars, where the angular momentum loss rate depends on the donor mass  $M_d$ , donor radius  $R_d$ , and rotation rate  $\Omega$ ,  $\dot{J} \propto M_d R_d^\gamma \Omega^3$ . The functional form of the Skumanich MB can be also obtained theoretically assuming a radial magnetic field, isotropic isothermal winds, and boosting of the magnetic field by rotation. Here we show that this simple form of the Skumanich MB law gives mass transfer rates an order of magnitude too weak to explain most observed persistent LMXBs. This failure suggests that the standard Skumanich MB law should not be employed to interpret Galactic, or extragalactic, LMXB populations, with either detailed stellar codes or rapid binary population synthesis codes. We investigate modifications for the MB law, and find that including a scaling of the magnetic field strength with the convective turnover time, and a scaling of MB with the wind mass loss rate, can reproduce persistent LMXBs, and does a better job at reproducing transient LMXBs.

**Key words:** methods: numerical – binaries: general – stars: evolution – stars: magnetic field – X-rays: binaries.

## 2.1 Introduction

Low mass X-ray binaries (LMXBs) with a neutron star (NS) accretor are among the most well-studied binary systems in astrophysics. Over 100 of them have been observationally identified in the Milky Way over the last 50 years, while a plethora of binary parameters – mass ratios, orbital periods, mass transfer (MT) rates, and donors' effective temperatures in some cases – have been determined for several of them. For many years, X-ray binaries have posed as an enticing problem for theorists, providing grounds to verify ways to model binary stellar evolution (Faulkner, 1971; Rappaport et al., 1983; Webbink et al., 1983; Joss and Rappaport, 1984; Podsiadlowski et al., 2002). The applications of theoretical models of LMXBs are not limited to only our Galaxy, but have also been applied to interpret the observed populations of X-ray binaries in

other galaxies (e.g., Fragos et al., 2008; Tremmel et al., 2013), and even to estimate their feedback on reionization of the early universe (e.g., Fragos et al., 2013)

Understanding and interpreting LMXBs can be split into two distinct stages: the formation and life of a binary system with a NS before the start of the MT, and the evolution of the binary system during the MT. Before the onset of the MT, the evolution of the binary is expected to proceed through a common envelope phase and a supernova explosion (Bhattacharya and van den Heuvel, 1991). Supernova natal kicks, supernova explosion mechanisms, and widely used pulsar kick distributions, while observationally derived, are not fully understood (Fryer et al., 2012; Hobbs et al., 2005). The outcomes of common envelope events are highly uncertain as well (for a review, see Ivanova et al., 2013).

In this paper, we focus on the evolution of LMXBs during MT. The driving mechanism of the MT phase is the donor's response to the mass and angular momentum loss. In short period systems, the dominant channel of angular momentum loss is gravitational radiation, which is well understood theoretically and has been confirmed by observations (Weisberg and Huang, 2016; LIGO Scientific Collaboration and VIRGO Collaboration, 2016; LIGO Scientific Collaboration and Virgo Collaboration, 2017). In cases with longer orbital periods, magnetic braking (MB) is the dominant angular momentum loss mechanism (Rappaport et al., 1983). The strength of MB affects the evolution of LMXBs by increasing or decreasing the angular momentum loss of the binary. In cases where the angular momentum loss is greater, the binary will tend to shrink and thus undergo more aggressive MT. The default assumption for MB is to adopt the "Skumanich" empirical law where the angular momentum loss scales with donor mass  $M_d$ , donor radius  $R_d$ , and rotation rate  $\Omega$ ,  $\dot{J} \propto M_d R_d^\gamma \Omega^3$  (Skumanich, 1972). In theoretical models, this empirical law is used by employing the parameterized prescriptions for MB stated by either Verbunt and Zwaan

(1981) or Rappaport et al. (1983). Numerical studies of LMXB populations have shown systematic mismatches between simulated results and observations. Observed MT rates have been found differing from the predicted rates in simulated systems by up to an order of magnitude (Podsiadlowski et al., 2002). Despite obtaining more detailed data on LMXBs, the discrepancies remained prevalent. For instance, Sco X-1 cannot be explained by the "Skumanich" law. To match the observations of Sco X-1, the rate of angular momentum loss has to be boosted, for example by taking into account the effect of stellar wind loss Pavlovskii and Ivanova (2015).

We are taking this analysis a step further by including the effects of the convective turnover time, as well as considering a non-isothermal stellar wind § 2.2.2. We apply different MB laws to a grid of 2136 binary systems spanning reasonable initial conditions, for a circularized binary system with a NS, where MT starts within 10 Gyr § 2.2.1. We describe the principal properties of the simulated MT systems in § 2.4 and have compiled a table with updated properties of some observed NS LMXBs (see § 2.3). The observational data is then used to constrain the MB laws in § 2.5.

## 2.2 Numerical Method

### 2.2.1 Setting up and evolving the population of binaries

We consider the set of initial binary systems as follows:

- The masses of donors range from  $M_d = 1.0M_\odot$  to  $M_d = 7M_\odot$ . The grid in donor masses uses steps of  $1M_\odot$  for donors with masses  $\geq 5M_\odot$ ,  $0.5M_\odot$  for donors between  $3M_\odot$  and  $5M_\odot$ ,  $0.2 M_\odot$  for donors between  $2.4M_\odot$  and  $3M_\odot$ , and  $0.1M_\odot$  for donors with masses  $\leq 2.4M_\odot$ . This is the mass of the donors at ZAMS. The adopted metallicity is  $Z = 0.02$ .
- The initial binary orbital periods range from the periods at which the

donor stars would overflow their Roche lobes at ZAMS, to the maximum orbital period at which they would start the MT while they are on the red giant branch. We define the initial period as the period at ZAMS of the donor star; which is not the same as the period that a binary would have at the start of the MT. There can be a large difference between when the initial period at the donor stars ZAMS and at the onset of RLOF. The mesh for the initial orbital periods has a fixed step of 0.05 in  $\log_{10}(P)$ . All orbits are circular.

- With the initial mesh of seed masses and periods, we ran 2136 simulations for each considered MB scheme (see § 2.2.2).
- The compact companions are NSs with mass  $M_a = 1.4M_\odot$  and radius  $R_a = 11.5$  km.

All calculations for the single stars and mass transferring binaries were performed using the one-dimensional stellar evolution code **MESA**<sup>1</sup> (Modules for Experiments in Stellar Astrophysics), revision 10398 and the August 2018 release of the **MESASDK**<sup>2</sup>. **MESA** is a modern open-source set of stellar libraries as described in Paxton et al. (2011, 2013, 2015, 2018). The donors are evolved using default assumptions as in **MESA**. In particular, we use the mixing length  $\alpha = 2$ , no semiconvection, and no overshooting. **MESA** uses mixing length theory as described in Cox and Giuli (1968). We adopt a grey atmosphere boundary condition and use the OPAL opacity tables for solar composition (Grevesse and Noels, 1993)<sup>3</sup>.

The donor stars are evolved using Reimer’s wind mass loss prescription (Reimers, 1975):

---

<sup>1</sup><http://mesa.sourceforge.net>

<sup>2</sup><http://www.astro.wisc.edu/~townsend/static.php?ref=mesasdk>

<sup>3</sup>The inlists files can be found at the **MESA** marketplace website: [http://cococubed.asu.edu/mesa\\_market/](http://cococubed.asu.edu/mesa_market/)

$$\dot{M}_d^w = \eta \times 4 \times 10^{-13} \frac{R}{R_\odot} \frac{L}{L_\odot} \frac{M_\odot}{M} M_\odot \text{yr}^{-1}, \eta = 1 \quad (2.1)$$

$\eta$  is a scaling factor or efficiency of wind loss. In our calculations we use  $\eta = 1$ .

When the donor star overfills its Roche lobe we calculate MT; we do not consider any other forms of MT. For the Roche lobe radius, we use the fitting formula for the volume equivalent one-dimensional star's radius, as provided by Eggleton (1983):

$$\frac{R_L}{a} = \frac{0.49q^{2/3}}{0.6q^{2/3} + \ln(1 + q^{1/3})}. \quad (2.2)$$

Here  $R_L$  is the Roche lobe radius of the donor star with mass  $M_d$ ,  $a$  is the orbital separation between the two stars, and  $q = M_d/M_a$  is the mass ratio of the two stars. To calculate the MT via the Lagrange point between the two stars  $L_1$ ,  $\dot{M}_d^{L1}$ , we employ the “Ritter” mass loss scheme, as implemented in MESA (see Ritter, 1988, for details of this MT prescription). We consider that the MT may be non conservative. If  $\dot{M}_d^{L1}$  exceeds the Eddington-limited MT rate  $\dot{M}_{\text{Edd}}$ , the excess  $\dot{M}_d^{L1} - \dot{M}_{\text{Edd}}$  cannot be accreted on to the compact object, and is assumed to be lost from the system. For the Eddington limited MT rate on a NS we use,

$$\dot{M}_{\text{Edd}} = \frac{4\pi c R_a}{\kappa_e} \approx \frac{3.4}{1+X} \times 10^{-8} M_\odot \text{ yr}^{-1} \quad (2.3)$$

Here  $\kappa_e$  is the opacity due to Thomson electron scattering,  $\kappa_e = 0.2(X+1) \text{ cm}^2 \text{ g}^{-1}$ , where  $X$  is the hydrogen mass fraction in the material transferred from the donor.

The angular momentum of the system is lost through gravitational radiation, or through MB, or is carried away with the mass lost from the system. The mass lost from the donor due to wind mass loss leaves with the specific angular momentum of the donor. Note the orbital evolution is calculated before the start of the MT as well. If the MT rate exceeds  $\dot{M}_{\text{Edd}}$ , the material

exceeding the Eddington limit is lost with the specific angular momentum of the accretor. The angular momentum loss due to gravitational radiation is found using the standard formula (Faulkner, 1971):

$$\frac{\dot{J}_{\text{GR}}}{J} = -\frac{32}{5} \frac{G^3}{c^5} \frac{M_{\text{d}} M_{\text{a}} (M_{\text{d}} + M_{\text{a}})}{a^4} \quad (2.4)$$

### 2.2.2 Magnetic braking

We calculate the MT sequences considering several prescriptions for the angular momentum loss via MB. The first prescription considered uses the formulation from Rappaport et al. (1983):

$$\dot{J}_{\text{MB,Sk}} = -3.8 \times 10^{-30} M_{\text{d}} R_{\odot}^4 \left( \frac{R_{\text{d}}}{R_{\odot}} \right)^{\gamma_{\text{mb}}} \Omega^3 \text{dyne cm} \quad (2.5)$$

Here,  $R_{\text{d}}$  is the radius of the donor,  $\gamma_{\text{mb}}$  is a dimensionless parameter from 0 to 4 and  $\Omega$  is the angular velocity of the donor. The stars are kept in corotation with the binary as the angular velocity is calculated using the binary period. With  $\gamma_{\text{mb}} = 4$ , Equation 2.5 describes the standard Skumanich law as derived by Verbunt and Zwaan (1981), and is the most commonly used form for MB in calculations of LMXB evolution.

The Skumanich law was scaled to describe main sequence stars similar to our Sun. In systems with donors different from the Sun, the increased rate of mass loss with the stellar wind, as well as magnetic field strength that does not scale directly with the angular velocity of the star, will play a role in the MB calculation (Mestel, 1968; Mestel and Spruit, 1987; Kawaler, 1988). To determine the effects of these additional terms, we follow similar steps as Pavlovskii and Ivanova (2015). We start with the formulation given by Mestel and Spruit (1987) which parameterizes the amount of angular momentum lost from the system through mass leaving through the Alfvèn surface. The Alfvèn surface is the surface where the ram pressure is equal to the magnetic pressure

(Mestel, 1968; Mestel and Spruit, 1987):

$$\frac{1}{2}\rho_A v_A^2 \simeq \frac{B(r)^2}{8\pi}. \quad (2.6)$$

$\rho_A$  and  $v_A$  denote the density and velocity of the wind as it crosses the Alfvèn surface.  $B(r)$  is the poloidal magnetic field strength as a function of radius. This value encompasses the structure of the magnetic field of the star. In the simplest case where the magnetic field is radial, and  $B_s$  is the surface magnetic field strength, then:

$$B(r) = B_s \frac{R_s^2}{r^2}. \quad (2.7)$$

Throughout this work, we will only be using a radial magnetic field, but it should be noted that other magnetic field structures are possible. In the context of magnetic braking however, the Alfvèn surface represents the maximum radius where the stellar wind is locked in corotation with the surface of the star, beyond this point the mass is assumed to be lost (Mestel, 1968; Mestel and Spruit, 1987). The equation which describes the angular momentum loss through an Alfvèn surface is:

$$\begin{aligned} \dot{J}_{MB} &= -4\pi\Omega \int_0^{\pi/2} \rho_A v_A R_A^2 (R_A \sin \theta)^2 \sin \theta d\theta \\ &\simeq -\frac{8}{3}\pi\Omega\rho_A v_A R_A^4, \\ &\simeq -\frac{2}{3}\Omega\dot{M}_W R_A^2. \end{aligned} \quad (2.8)$$

Here it is assumed that the Alfvèn surface,  $R_A$  does not depend on  $\theta$ , the polar angle, and that the wind coming from the star is isotropic. Should the system be rapidly rotating the scaling of the magnetic braking to the rotation rate will change as so-called dead zones may form (see discussion in Ivanova, 2006). It is important to note the Mestel and Spruit (1987) parameterization

can account for “dead zones” where material is trapped in magnetic fields lines and not lost through the Alfvèn surface. The material confined within the dead zone remain in corotation within the dipole field and is not lost from the system. We don’t include the effects of dead zones in this work and as such may over estimate the amount of material lost and thus the angular momentum loss in tight binaries. The wind mass loss rate, if isotropic can be described using the following equation:

$$\begin{aligned}\dot{M}_W &= 4\pi R^2 \rho_s v_s, \\ &= 4\pi R_A^2 \rho_A v_A,\end{aligned}\tag{2.9}$$

Combining equations 2.6 and 2.7 gives us:

$$4\pi R_A^4 \rho_A v_A^2 = B_s^2 R^4,\tag{2.10}$$

Including the wind mass loss equation as given in equation 2.9, equation 2.10 becomes:

$$\begin{aligned}\dot{M}_W R_A^2 v_A &= B_s^2 R^4, \\ R_A^2 &= \frac{B_s^2 R^4}{\dot{M}_W v_A}.\end{aligned}\tag{2.11}$$

Under the assumption of isothermal winds, the wind reaches a sonic wind velocity at the Alfvèn surface of  $v_A = c_w$  (Mestel and Spruit, 1987) where  $c_w$  is a constant value. Combining equations 2.8 and 2.11 gives the following MB scaling equation:

$$\dot{J}_{\text{MB}} \propto \Omega B_s^2 R^4.\tag{2.12}$$

Equation 2.12 interestingly, does not contain any scaling with the stellar

wind, despite the wind strength being a fundamental physical property of MB. The assumption of isothermal winds does not apply to giant stars. In the case of giant stars with cooler temperatures, winds may be accelerated by a variety of mechanisms, this requires a different self-consistent description of the wind velocity (Suzuki, 2007). In the case of a radial field and a nonthermal wind where the wind moves at speeds on order of the escape velocity,

$$v_A^2 = \frac{2GM}{R}, \quad (2.13)$$

We get the following scaling:

$$\dot{J}_{\text{MB}} \propto \dot{M}_{\text{W}} \Omega B_s^4 R^4. \quad (2.14)$$

The strength of the surface magnetic field,  $B_s$ , scales with the dynamo number  $N_d$  (Parker, 1971). The dynamo number is related to physical values in the MB through the Rossby number,  $R_0$  (Noyes et al., 1984),

$$\begin{aligned} N_d &\approx R_0^{-2}, \\ N_d &\approx \Omega^2 \tau_{\text{conv}}^2. \end{aligned} \quad (2.15)$$

Here  $\tau_{\text{conv}}$  is the turnover time of convective eddies,

$$\tau_{\text{conv}} = \int_R^{R_s} \frac{dr}{v_{\text{conv}}}. \quad (2.16)$$

$R$  and  $R_s$  are the bottom and the top of the outer convective zone respectively, while  $v_{\text{conv}}$  is the local convective velocity. We follow a simple approximation made by Ivanova (2006) where  $B_s \propto N_d^{1/2}$ . This allows us to adopt the scaling relations:

$$\begin{aligned}\frac{B_s}{B_{s,\odot}} &= \frac{R_0}{R_{0,\odot}}, \\ \frac{B_s}{B_{s,\odot}} &= \frac{\Omega}{\Omega_\odot} \frac{\tau_{\text{conv}}}{\tau_{\odot\text{conv}}}.\end{aligned}\tag{2.17}$$

Work by Aurière et al. (2015) has shown a general correlation between the semi-empirical Rossby number and the observed magnetic field strength of a star. Aurière et al. (2015) also noted that dwarf stars have a steeper relation between these properties than giant stars. In general, dwarf stars have been found to have shorter rotation periods with strong magnetic fields. As such, the relation used likely underestimates the strength of the magnetic field in dwarf stars. Rewriting the magnetic field scaling in Equation 2.12 gives us the following:

$$\begin{aligned}\dot{J}_{\text{MB}} &\propto \Omega B_s^2 R^4, \\ &\propto \Omega^3 \tau_{\text{conv}}^2 R^4.\end{aligned}\tag{2.18}$$

The radial isothermal approximation results in the Skumanich scaling with  $\Omega^3 R^4$  if we ignore the convective turnover time  $\tau_{\text{conv}}$ . The radial non-thermal approximation from Equation 2.14 becomes

$$\begin{aligned}\dot{J}_{\text{MB}} &\propto \dot{M}_W \Omega B_s^4 R^4 \\ &\propto \dot{M}_W \Omega^5 \tau_{\text{conv}}^4 R^4.\end{aligned}\tag{2.19}$$

Rewriting the Skumanich law to include the additional terms for wind  $\dot{M}_W$ , convective turnover time  $\tau_{\text{conv}}$  and rotation rate  $\Omega$ , the general MB equation we use will be

$$\dot{J}_{\text{MB,boost}} = \dot{J}_{\text{MB,Sk}} \left( \frac{\Omega}{\Omega_{\odot}} \right)^{\beta} \left( \frac{\tau_{\text{conv}}}{\tau_{\odot,\text{conv}}} \right)^{\xi} \left( \frac{\dot{M}_{\text{W}}}{\dot{M}_{\odot,W}} \right)^{\alpha}. \quad (2.20)$$

The value used to normalize the convective turnover time,  $\tau_{\odot,\text{conv}} = 2.8 \times 10^6$  s, was found by evolving a  $1M_{\odot}$  star at  $Z=0.020$  to 4.6 Gyrs. Similarly, the solar wind value  $\dot{M}_{\odot,W} = 2.5 \times 10^{-14} M_{\odot} \text{ yr}^{-1}$  (Carroll and Ostlie, 2006), and  $\Omega_{\odot} \approx 3 \times 10^{-6} \text{ s}^{-1}$  is the angular frequency of the Sun using an orbital period of 24 days.

The power  $\xi$  can vary, where  $\xi = 0$  describes the same simplified assumptions for which the Skumanich law is valid with  $\alpha = 0$  and  $\beta = 0$  (i.e., radial magnetic field and isothermal winds).  $\xi = 2$  is the case described in equation 2.18 which results in the convection boosted Skumanich case.  $\xi$  may be as high as 4 for the case of winds from giants where the velocity of the wind grows linearly with distance; we note that in this case, the dependence on the angular velocity will also have to be modified to  $\Omega^5$ , vs. the Skumanich law's factor of  $\Omega^3$ . Therefore in this case,  $\xi = 4$ ,  $\beta = 2$  and  $\alpha = 1$ .

We will use these additional scaling terms and define different MB cases for the tested grid of binaries:

1. “Default”: We use the default MB scheme described by Rappaport et al. (1983), without the additions mentioned in Pavlovskii and Ivanova (2015).  $\gamma_{\text{mb}} = 4$  in this case, and all subsequent cases.
2. “Convection-boosted”: We adopt the scaling found in Equation 2.18, which is the Skumanich law, scaled by the convective turnover time  $(\tau_{\text{conv}})^{\xi}$ . The value of  $\xi = 2$  will be used in this prescription.
3. “Intermediate”: We use the convection-boosted MB scheme and apply an additional wind scaling term, linear in wind mass loss rate ( $\alpha = 1$ ).
4. “Wind-boosted”: This MB scheme uses the scaling values from Equation 2.19. This prescription includes all three scaling terms shown in

Case	$\beta$	$\xi$	$\alpha$
1 - Default Skumanich	0	0	0
2 - Convection Boosted	0	2	0
3 - Intermediate	0	2	1
4 - Wind Boosted	2	4	1

Table 2.1: The different scaling values used in Equation 2.20 for the various cases.

Equation 2.20 with  $\beta = 2$ ,  $\xi = 4$  and  $\alpha = 1$ .

These systems are evolved to 10 Gyrs, or until the donor star loses its envelope and detaches. If the simulation encounters dynamically unstable MT, which `MESA` was not designed to adequately model, the system will likely encounter numerical issues and stop. We do not consider irradiation effects on the companion star during its evolution (see §6).

### 2.2.3 Verification against a previous study

Of particular importance is the binary system Scorpius X-1 as this system allows us to compare our results to the work of Pavlovskii and Ivanova (2016). In Pavlovskii and Ivanova (2016), the authors used a modified MB prescription where  $\alpha = 1$ ,  $\beta = 0$ , and  $\xi = 0$ , with an MB gamma  $\gamma_{\text{mb}}$  of 3. In this work, we tested all MB prescriptions described in §2.2.1 and used an MB gamma  $\gamma_{\text{mb}}$  of 4. To ensure the changes to MB were correctly implemented, the comparisons between models used in Pavlovskii and Ivanova (2016) were rerun.

Sco X-1 is an LMXB, observed to have a mass ratio in the range from 0.28 - 0.51, favouring a value of  $\approx 0.30$  (Mata Sánchez et al., 2015; Steeghs and Casares, 2002). The NS is constrained to have a mass of  $< 1.73 M_\odot$  (Mata Sánchez et al., 2015). The period of Sco X-1 is 18.8951 hours, and the MT rate is estimated to be at least  $\sim 2.2 \times 10^{-8} M_\odot \text{yr}^{-1}$  (Watts et al., 2008; Pavlovskii and Ivanova, 2016). Observations of this system provided upper limits on the spectral class of the donor of K4 or later, with the luminosity class IV, and the implied effective temperature less than 4800 K.

The models tested in Pavlovskii and Ivanova (2016) were composed of a donor at ZAMS with masses ranging from  $0.9$  to  $1.8M_{\odot}$ , and a NS varying from  $1.24$  to  $1.6M_{\odot}$ . They assumed solar metallicity and Reimer’s wind prescription. That study, to find the mass transferred the  $L_1$  Lagrange point,  $\dot{M}_d^{L1}$ , used the method described in Pavlovskii and Ivanova (2015), while we use the “Ritter” prescription. The method of Pavlovskii and Ivanova (2015) is important for determining the initial MT stability in systems with a very high mass ratio, and the use of the “Ritter” prescription should not play a role in the test of Sco X-1, or in finding long-lived LMXBs. Pavlovskii and Ivanova (2016) considered the case of standard MB and wind-boosted MB, adopting  $\gamma_{mb} = 3$  for both. This is the default value for  $\gamma_{mb}$  in **MESA**<sup>4</sup>. Pavlovskii and Ivanova (2016) find the default prescription of MB gives insufficient mass transfer to reproduce the observed mass transfer rate of Sco X-1, by at least an order of magnitude. To produce the observed properties of Sco X-1 (within  $\approx 10\%$  estimated uncertainty), a modified MB law must instead be used.

In this test only, for comparison purposes, we have run similar MT sequences with  $\gamma_{mb} = 3$ . We considered one of the sets of binary companion masses presented in Pavlovskii and Ivanova (2016): a  $1.3M_{\odot}$  NS and a  $1.0 M_{\odot}$  donor. The test run for the default MB was done using an initial period of 2.7 days, while for the test of the wind-boosted MB we used an initial period of 7.6 days. Both initial periods were taken from systems in Pavlovskii and Ivanova (2016). The binary systems were evolved until they had similar orbital periods as Sco X-1. The MT tracks of the two systems are shown in Figure 2.1. They are similar to those shown in Figures 1 and 2 of Pavlovskii and Ivanova (2016). The results of the simulations with the two MB prescriptions as well as the observed values are listed in Table 2.2.

As can be seen, we confirm that the modified MB prescription better re-

---

<sup>4</sup>We note this value was chosen to be default by the **MESA** core developers groups, to make a test comparison to results published in the past, and is not motivated by physics; we remain convinced that the standard Skumanich law should be used with  $\gamma_{mb} = 4$ .

Table 2.2: Sco X-1 Test Properties

Quantity	Observed	Boosted MB	Default MB	Ref.
Mass Ratio	0.28 - 0.51	0.42	0.28	(1,2)
Period [Hours]	18.89551	18.90	18.90	(3)
MT [ $M_{\odot}\text{yr}^{-1}$ ]	$2.2 \times 10^{-8}$	$2.1 \times 10^{-8}$	$1.1 \times 10^{-9}$	(3)
Effective Temperature [K]	4800	4718	4627	(1,2)
Donor Mass [ $M_{\odot}$ ]	0.28 - 0.70	0.56	0.50	(1,2)
NS Mass [ $M_{\odot}$ ]	< 1.73	1.33	1.79	(1,2)

**Notes.** The calculated values are taken at the point where the period of the simulated binary is  $\approx 18.89551$  hours. (1) Steeghs and Casares (2002); (2) Mata Sánchez et al. (2015); (3) Watts et al. (2008)

produces the observed value of the MT rate in Sco X-1. We will return to the case of Sco X-1 in section 2.5 to review which MB prescriptions can reproduce Sco X-1.

### 2.3 Observational Data for NS LXMBs

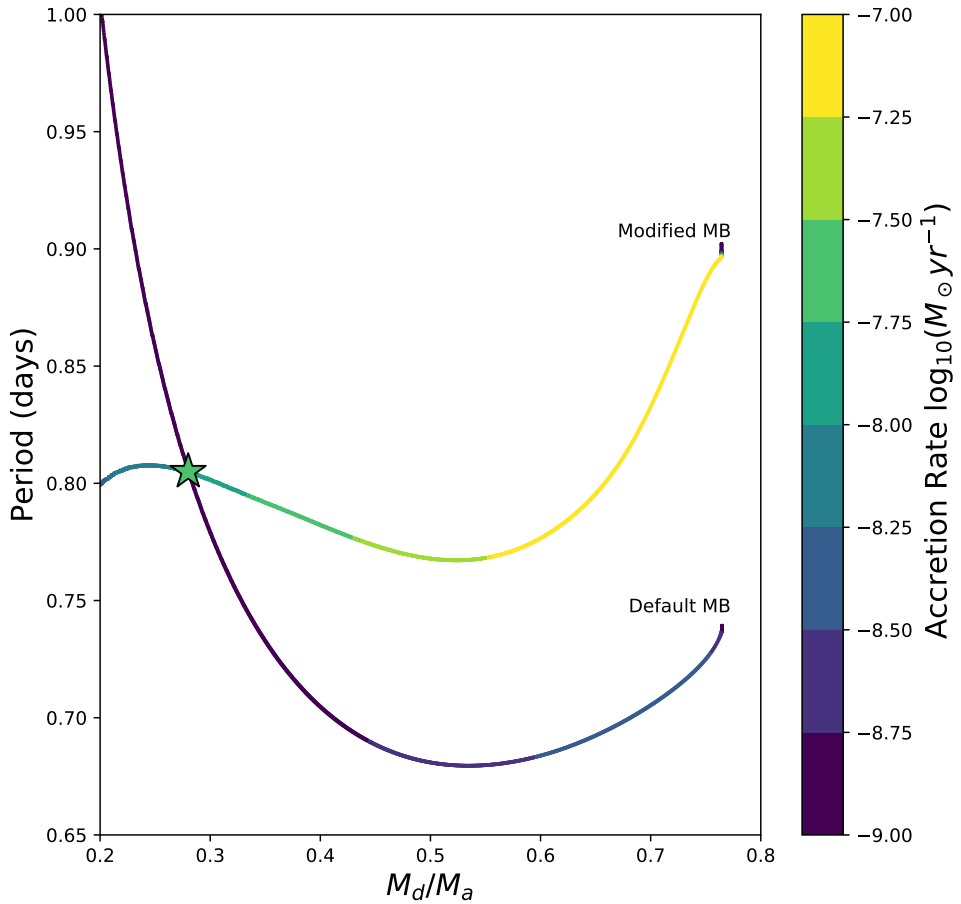


Figure 2.1: The results of the two models tested to verify our results to reproduce the observed system Sco X-1. The upper curve in the plot is the evolution using the modified MB, and the lower curve is the evolution using the default MB. The star on the plot represents the approximate location of Sco X-1 based on observations with the colour of the star corresponding to the observed mass transfer rate. The colour bar denotes the MT rate of the binary system with the observed MT of Sco X-1 observed as  $\log_{10}(M_\odot/\text{yr}^{-1}) \approx -7.7$ . The modified MB can reproduce the appropriate MT observed in Sco X-1 while the default MB cannot.

CC

Source	Flags	$M_d$ ( $M_\odot$ )	Mass Ratio ( $M_d/M_a$ )	Period (Hours)	Distance (kpc)	Average Mass Transfer ( $M_\odot \text{ yr}^{-1}$ )	Reference
4U 1820-303	Per, GC, UC	—	—	0.183 S87	$7.9 \pm 0.4$ H13	$1.2 \pm 0.6 \times 10^{-8}$ H13	S87, H13
4U 0513-40	Per, GC, UC	0.045	0.03*	0.283 Z09	$12.1 \pm 0.6$ H13	$1.2 \pm 0.6 \times 10^{-9}$ H13	Z09, H13
2S 0918-549	Per, UC	0.024 – 0.039 Z11	0.02 – 0.03*	0.290 S01	$5.4 \pm 0.8$ H13	$2.6 \pm 1.5 \times 10^{-10}$ H13	Z11, H13
4U 1543-624	Per, UC	0.03 W04	0.02*	0.303 W04	7 H13	$1.3_{-1.2}^{+1.8} \times 10^{-9}$ H13	W04, H13
4U 1850-087	Per, GC, UC	0.04 H96	0.03*	0.343 H96	$6.9 \pm 0.3$ H13	$2.2 \pm 1.1 \times 10^{-10}$ H13	H96, H13
M15 X-2	Per, GC, UC	0.02 – 0.03 D05b	0.02*	0.377 D05b	$10.4 \pm 0.5$ H13	$3.8 \pm 1.9 \times 10^{-10}$ H13	D05b, H13
IGR J17062-6143	T, PSR, UC	0.0155 – 0.0175 S18b	0.01*	0.633 S18b	$7.3 \pm 0.5$ K17	$2.5 \times 10^{-11}$ K17	K17, S18b
XTE J1807-294	T, PSR, UC	—	—	0.670 M03	$8_{-3.3}^{+4}$ H13	$< 1.5_{-1.2}^{+1.9} \times 10^{-11}$ H13	M03, H13
4U 1626-67	Per, PSR, UC	$< 0.036$ H13	0.02*	0.700 C98a	$8_{-3}^{+5}$ H13	$8.0_{-6}^{+14} \times 10^{-10}$ H13	C98a, H13
XTE J1751-305	T, PSR, UC	—	—	0.710 M02	$8_{-1.3}^{+0.5}$ H13	$5.1_{-2.9}^{+2.6} \times 10^{-12}$ H13	M02, H13
XTE J0929-314	T, PSR, UC	$\simeq 0.01$ G02	0.007	0.730 G02	$8_{-3}^{+7}$ H13	$< 9.7_{-7.7}^{+25} \times 10^{-12}$ H13	G02, H13
4U 1916-053	Per, UC	$0.064 \pm 0.01$ H13	0.046	0.833 W81	$9.3 \pm 1.4$ H13	$6.3 \pm 3.7 \times 10^{-10}$ H13	W81, H13
Swift J1756.9-2508	T, PSR, UC	$\leq 0.022$ K07	0.02	0.912 K07	$8 \pm 4$ H13	$1.7_{-1.5}^{+2.3} \times 10^{-11}$ H13	K07, H13
NGC 6440 X-2	T, PSR, GC, UC	$\simeq 0.0076$ B15	0.005	0.955 A10	$8.5 \pm 0.4$ H13	$1.0 \pm 0.5 \times 10^{-12}$ H13	A10, B15, H13
HETE J1900.1-2455	T, PSR	0.016 – 0.07 K06a	0.01 – 0.05*	1.39 W08	$4.7 \pm 0.6$ W08	$4.63 \times 10^{-11}$ W08	K06a, W08
1A 1744-361	T	0.07 – 0.22 B06	0.07?*	$1.62 \pm 0.37$ W08	$6 \pm 3$ W08	$2.22 \times 10^{-11}$ W08	B06, W08
IGR J17379-3747	T, PSR	$> 0.056$ S18a	$> 0.04^*$	1.88 S18a	$\sim 8.5$ S18a	$\sim 4 \times 10^{-11}$ S18a	S18a, S18c
SAX J1808-3658	T, PSR	$0.04_{-0.01}^{+0.02}$ W13	0.04*	2.01 C98b	$3.4 - 3.6$ C12	$1.73 \times 10^{-11}$ C12	C98b, C12, W13
XB 1832-330	T, GC	—	—	2.1 E12	10.0 P01	$\sim 3 \times 10^{-10}$ E12	P01, E12
IGR 00291+5934	T, PSR	0.039 – 0.16 D17	0.02 – 0.11	2.46 G06	$2.6 - 3.6$ C12	$1 \times 10^{-12}$ D17	C12, G05, D17
4U 1822-00	Per, M	—	—	3.20? S07	$6.3 \pm 2$ S07	$9.0_{-5.0}^{+8.0} \times 10^{-10}$ S07	S07
4U 1636-536	Per	0.29 – 0.48*	0.21 – 0.34 W16	3.79 W08	$6 \pm 0.5$ W08	$1.25 \times 10^{-9}$ C12	C12, W08, W16
EXO 0748-676	T	0.1? D14a	0.07?*	3.82 D14a	$7.1 \pm 1.2$ D14a	$< 4.4 \times 10^{-10}$ C12	C12, D14a
4U 1254-69	Per	0.45 C68b	0.33 – 0.36 C13	3.93 W08	$13 \pm 3$ W08	$1.77 \times 10^{-9}$ W08	C86b, C13, W08
4U 1728-16 (GX 9+9)	Per	0.4 K09b	0.29 K09b	4.20 L07	5? K06b	$2.91 \times 10^{-9}$ C97	C97, K06b, L07
XTE J1814-338	T	0.19 – 0.32 W17	$0.123_{-0.01}^{+0.012}$ W17	4.27 W08	$8 \pm 1.6$ C12	$< 5.99 \times 10^{-12}$ C12	C12, W08, W17

4U 1735-444	Per	$\leq 0.58$	$0.05 - 0.41^{C06}$	4.65 W08	$8.5 \pm 1.3$ W08	$6.31 \times 10^{-9}$ C12	C06, C12, W08
4U 1746-37	Per, GC	--	-	5.16 B04	11.6 B04	$1 \times 10^{-9}$ B04	S01, B04
2A 1822-371	Per, M	$0.47 \pm 0.04$ I15	$0.28$ I15	5.57 B17	2.5 B17	$\sim 2 \times 10^{-8}$ B17	B17, I15
XTE J2123-058	T	$0.76 \pm 0.22$ C02	$0.49 \pm 0.1$ C01	5.96 W08	$9.6 \pm 1.3$ W08	$< 7 \times 10^{-12}$ C12	C02, C12, S03a, W08
X 1658-298	T	$0.3 - 0.8$ P18	$0.21 - 0.57^*$	7.12 D14a	$12 \pm 3$ W08	$1 \times 10^{-9}$ W08	D14a, P18, W08
2A 0521-720 (LMC X-2)	Per, M	-	-	8.16 L07	$50 \pm 2$ A09	$4 \times 10^{-8}$ C12	C12, A09, L07
SAX J1748.9-2021	T, GC	$0.12 - 1$ S16	$0.09 - 0.71^*$	8.76 S16	$8.5 \pm 0.4$ S16	$\sim 7 \times 10^{-11}$ W08	S16, W08
IGR J18245-2452	T, GC	$> 0.17$ P13	$0.12^*$	11.0 P13	5.5 P13	$\lesssim 1.0 \times 10^{-10}$ P13	P13
GRS 1747-312	T, GC	--	-	12.36 I03	9.5 V18	$1 \times 10^{-10}$ V18	B04, V18
4U 1456-32 (Cen X-4)	T	$0.31 \pm 0.27$ D05a	$0.18 \pm 0.06$ D05a	15.1 L07	$1.2 \pm 0.2$ C12	$4 \times 10^{-11}$ C12	C12, D05a, L07
AC 211 (X2127+12)	Per, GC	$\sim 0.1$ V04	$\sim 0.1$ V04	17.1 I93	10.4 C68b	$\sim 7 \times 10^{-9}$ I93	C86, I93, V04
H 1617-155 (Sco X-1)	Per, M	$0.28 - 0.70$ S15	$0.28 - 0.51$ S15	18.9 W08	$2.8 \pm 0.3$ S15	$3 \times 10^{-8}$ C12	C12, S15, W08
4U 1908+005 (Aql X-1)	T	-	-	18.9 W08	$4.55 \pm 1.35$ W08	$6 \times 10^{-10}$ C12	C12, W08
4U 1624-49	Per	-	-	20.9 B00	$15_{-2.6}^{+2.9}$ X09	$4.6 \times 10^{-9}$ B09	B09, L05, X09
3A 1702-363 (GX 349+2)	Per	0.78*	$\sim 0.56$ I09	$21.9 \pm 0.4$ I09	$5 \pm 1.5$ C12	$2.37 \pm 1 \times 10^{-8}$ C12	C12, I09, W08
2A 1655+353 (Her X-1)	T	$2.03 \pm 0.37$	1.45	40.8 L07	$6.1_{-0.4}^{+0.9}$ L14	$1.3 \times 10^{-8}$ C12	C12, L07, R11
4U 2142+38 (Cyg X-2)	Per, M	$0.56 \pm 0.07$ P16	$0.34 \pm 0.01$ P16	236.3 W08	$10.55 \pm 4.45$ W08	$3.0 \times 10^{-8}$ C12	C12, M18, W08
GRO J1744-28	T, M	$0.2 - 0.7$ D15	$0.15 - 0.5^*$	284.0 L07	8? D15	$\sim 1 \times 10^{-8}$ D14b	D15, D14b, L07

Table 2.3: The periods and mass transfer rates are either taken directly from the listed reference, or calculated using values from that reference. Any value with a ? attached is a rough estimate of that value. If possible, the mass fraction or companion mass is taken directly from the source. If a companion mass or mass fraction can be calculated, this is done assuming a neutron star mass of  $1.4M_{\odot}$ . These calculated values are denoted by a \* and are simply an approximation. We include any errors that could be taken directly from the reference paper. In cases where an error was not listed but can be calculated, we did so. The error in the mass transfer rate is calculated by looking at the errors in distances, flux, or luminosity from the listed reference. The second column notes systems that are persistent (Per), transient (T), with a neutron star of mass exceeding  $1.6M_{\odot}$  (M), systems with pulsars (PSR), systems in globular clusters (GC), and ultra compact systems (UC). References: A09 - Agrawal and Misra (2009), A10 - Altamirano et al. (2010), B00 - Bałucińska-Church et al. (2004), B04 - Bałucińska-Church et al. (2004), B06 - Bhattacharyya et al. (2006), B09 - Balman (2009), B10 - Bayless et al. (2010), B15 - Bult et al. (2015), B17 - Bak Nielsen et al. (2017), C86a - Charles et al. (1986) C86b - Courvoisier et al. (1986), C97 - Christian and Swank (1997), C98a - Chakrabarty (1998), C98b - Chakrabarty and Morgan (1998), C02 - Casares et al. (2002), C06 - Casares et al. (2006), C12 - Coriat et al. (2012), C13 - Cornelisse et al. (2013), D05a - D'Avanzo et al. (2005), D05b - Dieball et al. (2005), D14a - D'Aì et al. (2014), D14b - Degenaar et al. (2014), D15 - D'Aì et al. (2015), D17 - De Falco et al. (2017), E12 - Engel et al. (2012), G02 - Galloway et al. (2002), G05 - Galloway et al. (2005), H96 - Homer et al. (1996), H07 - Heinke et al. (2007), H10 - Harris (2010), H13 - Heinke et al. (2013), I93 - Illovaisky et al. (1993), I03 - in't Zand et al. (2003), I09 - Iaria et al. (2009), I15 - Iaria et al. (2015), J10 - Jain et al. (2010), K06a - Kaaret et al. (2006), K06b - Kong et al. (2006), K07 - Krimm et al. (2007), K17 - Keek et al. (2017), L05 - Lommen et al. (2005), L07 - Liu et al. (2007), M02 - Markwardt et al. (2002), M03 - Markwardt et al. (2003), M18 - Mondal et al. (2018), P01 - Parmar et al. (2001), P13 - Papitto et al. (2013), P16 - Premachandra et al. (2016), P17 - Patruno (2017), P18 - Ponti et al. (2018), R11 - Rawls et al. (2011), S01 - Sidoli et al. (2001), S87 - Stella et al. (1987), S03a - Shahbaz et al. (2003), S07 - Shahbaz et al. (2007), S15 - Mata Sánchez et al. (2015) S16 - Sanna et al. (2016), S18a - Sanna et al. (2018), S18b - Strohmayer et al. (2018a), S18c - Strohmayer et al. (2018b) W81 - Walter et al. (1981), W04 - Wang and Chakrabarty (2004), W08 - Watts et al. (2008), W13 - Wang et al. (2013), W16 - Wisniewicz et al. (2016), W17 - Wang et al. (2017), V04 - van Zyl et al. (2004), V18 - Vats et al. (2018), X09 - Xiang et al. (2009), Z09 - Zurek et al. (2009), Z11 - Zhong and Wang (2011)

To compare our results to observations, we have compiled a list of up-to-date properties of some Milky Way NS LMXBs. See Table 2.3 for a list of systems, relevant data, and references.

The systems with periods shorter than 80 minutes are ultra-compact X-ray binaries (UCXBs), where the donor star must be partly or completely degenerate. Our binary evolution method may not necessarily be the dominant method to produce these systems, but we keep them in the consideration. Within the table there are also systems labelled as GC systems, which are systems found in globular clusters. Binaries formed within a globular cluster are not likely to be produced from primordial binaries, but instead are more effectively produced via dynamical encounters between binaries, as well as via physical collisions between NSs and subgiants (Verbunt, 1987; Ivanova et al., 2005, 2008).

The other flags shown in the second column denote if the source is a persistent or transient system. Persistent systems are those where bright ( $L_X > 10^{35}$  erg/s) X-ray emissions have been consistently seen whenever X-ray monitoring missions have observed these systems, over a 40-60 year timespan. Transient systems have large changes in their X-ray emission, typically exceeding  $L_X = 10^{36}$  erg/s at some points (outbursts) and declining below  $L_X = 10^{35}$  erg/s at other times (quiescence). There are several systems currently thought to be persistent which could instead be in a long-term outburst state (lasting  $>50$  years), and may be reclassified as transient systems in the future.

Meyer and Meyer-Hofmeister (1981) predicted the existence of a critical MT rate separating the persistent and transient systems. The disc instability model (DIM) predicts under what circumstances an accretion disk will experience instabilities (see Lasota, 2001, for a review of DIM). Stability in the context of the DIM means an accretion disc does not experience outbursts; a stable disc that remains hot will produce a persistent X-ray binary. The criterion for stability is given by Coriat et al. (2012):

$$\dot{M}_{\text{crit}} = k P_{\text{hr}}^b \text{ g s}^{-1} \quad (2.21)$$

Here,  $P_{\text{hr}}$  is the period of the system in hours. For the non-irradiated case,  $k = (2.6 \pm 0.9) \times 10^{16}$ , and  $b = 1.76$ . If there is irradiation of the accretion disc, and the accretor is a NS,  $b = 1.59$  and  $k = (2.9 \pm 0.9) \times 10^{15}$ . Systems that lie above the DIM line are expected to be persistent while systems below the line are transient.

Here, we only consider the systems where the MT rate is known. If the cited papers do not provide the MT rate but instead provide the X-ray luminosity,  $L_x$ , we find  $\dot{M}$  using

$$\dot{M} = \frac{L_x R_a}{GM_a} . \quad (2.22)$$

Observationally, an upper limit for NS mass has been found to be  $2.01 \pm 0.04 M_\odot$  (Antoniadis et al., 2013), our calculations will be done assuming the mass of the NS is  $M_a = 1.4 M_\odot$  with a radius of  $R_a = 11.5$  km (Özel and Freire, 2016). The key properties of interest for this work are the mass ratio  $q = M_d/M_a$ , the period  $p$  and the average mass transfer rate  $\dot{M}$ .

## 2.4 Principal Results

### 2.4.1 Evolutionary Tracks

Here we present the results for the 2136 binary models of each MB prescription by plotting the evolutionary tracks grouped by donor mass on subplots in figures 2.2 - 2.5. These figures show the donor mass and period evolution of each simulated binary over the course of its lifetime. Mass in these figures is meant as a proxy for time as the donor stars all decrease in mass over the course of the binary evolution. The binary population simulations each required on order of hours to days to finish, totalling approximately thirty core years of

simulation time. For comparison purposes, we overlay the observed data points from Table 2.3 on the plots. Sco X-1 is denoted with a star in the subplots as it was our test case from 2.2.3.

We can see that our choice of initial conditions affects the resulting evolutionary track of the system. In general, the more massive the donor star, the higher the MT rate. The choice of initial period results in changes that are less monotonic in comparison. Many systems starting with short periods may initiate Roche lobe overflow (RLOF) immediately, while longer period systems may lose significant mass through winds before this.

The separation between systems which evolve to longer orbital periods during their evolution, and those in which the orbital periods shrink, is known as the bifurcation period (Podsiadlowski et al., 2002; van der Sluys et al., 2005). As the initial donor mass increases, the bifurcation period also increases until we encounter systems undergoing dynamically unstable MT. We will refer to a binary with the orbital period near the end of its evolution larger than the period at the start of RLOF as growing in period, while systems with a shorter period near the end of their evolution are shrinking. One can see that most of the observed LMXBs are located in the region of shrinking systems. Specifically, in the case using the default Skumanich law, several of them are in the parameter space where the shrinking and growing systems bifurcate.

## Default

The default Skumanich MB results are shown in Figure 2.2. This MB prescription produces a clear bifurcation in periods through the low and intermediate mass donors. The bifurcation period at RLOF is  $\sim 1$  day and shows a distinct split in periods as no binaries pass through the region  $q < 0.4$ ,  $1 \lesssim \log_{10}(P) \lesssim 2.5$ . The sharp transition seen in the low mass high period systems is a result of the binary reaching a stopping conditions given in Section 2.2.1.

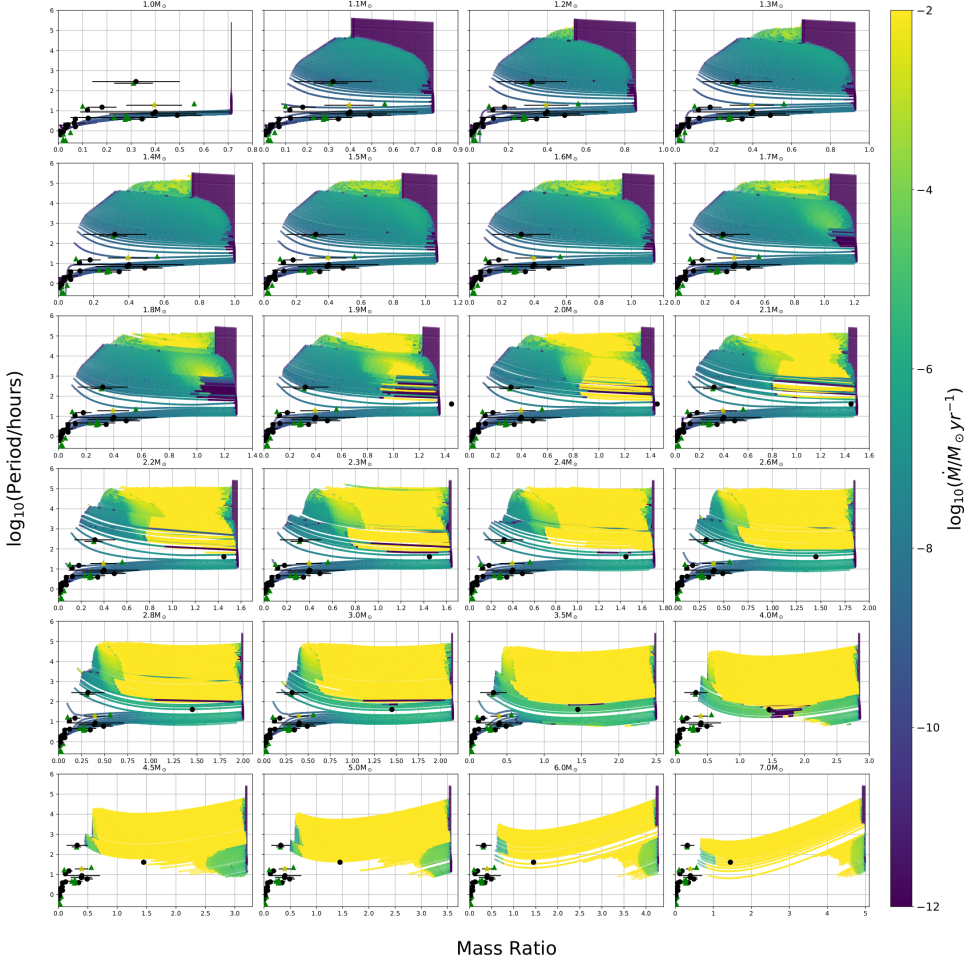


Figure 2.2: A collection of subplots showing the evolution through mass transfer for all initial periods, shown on the grid of initial donor masses and mass ratios. The data shown is only after the onset of RLOF with the colour bar indicating  $\log_{10}(\dot{M})$ . The evolutionary tracks evolve from the right of the subplots leftwards as the donor loses mass through mass transfer. At higher donor masses and low periods, there exist a subset of systems which abruptly terminate their tracks as they begin to transfer mass dynamically. The points on the plot represent observable systems, with errors found in Table 2.3. Circles are transient systems, and triangles are persistent systems. The single star point is the binary Sco X-1 used to test the validity of our numeric results. The range of periods in each plot is the same, but the range of donor masses differs. The abrupt cutoff at higher periods is a result of the star reaching the end of its life.

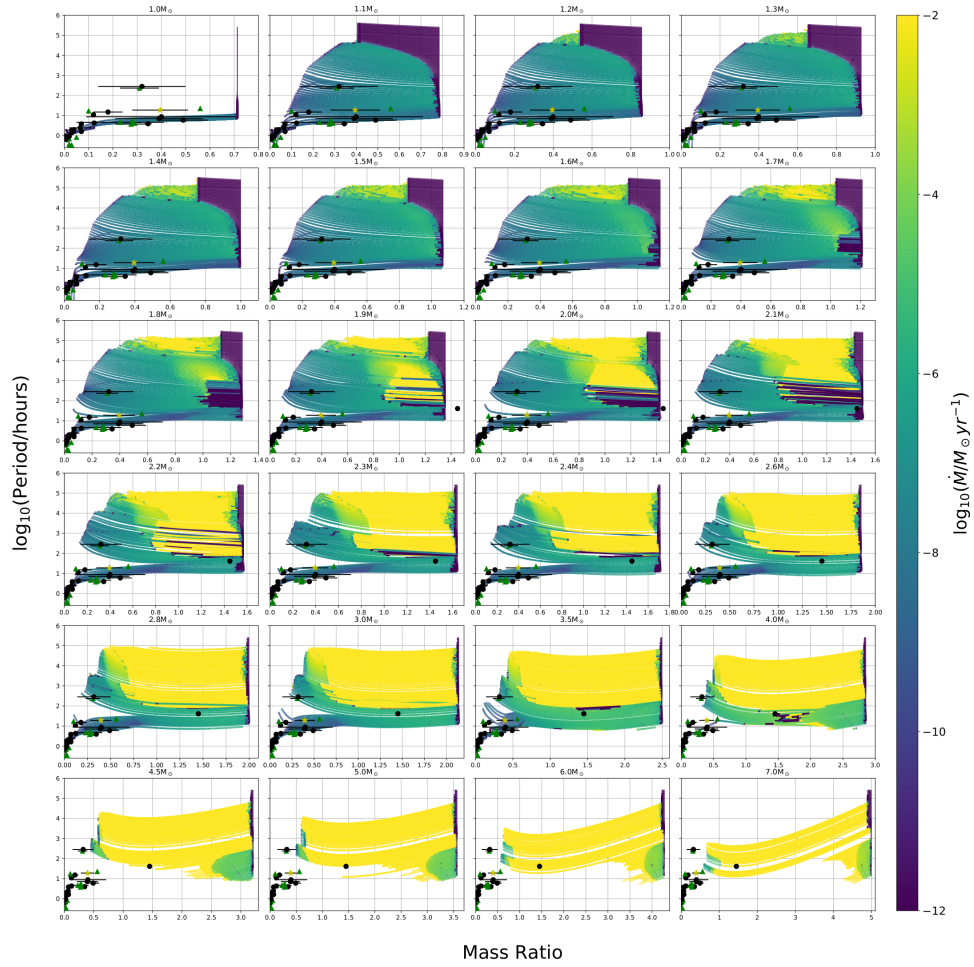


Figure 2.3: A similar figure to 2.2 using case 2, convection boosted MB from Table 2.1. The general behaviour of these simulated systems is similar to that of the systems following the Skumanich law, in Fig. 2.2.

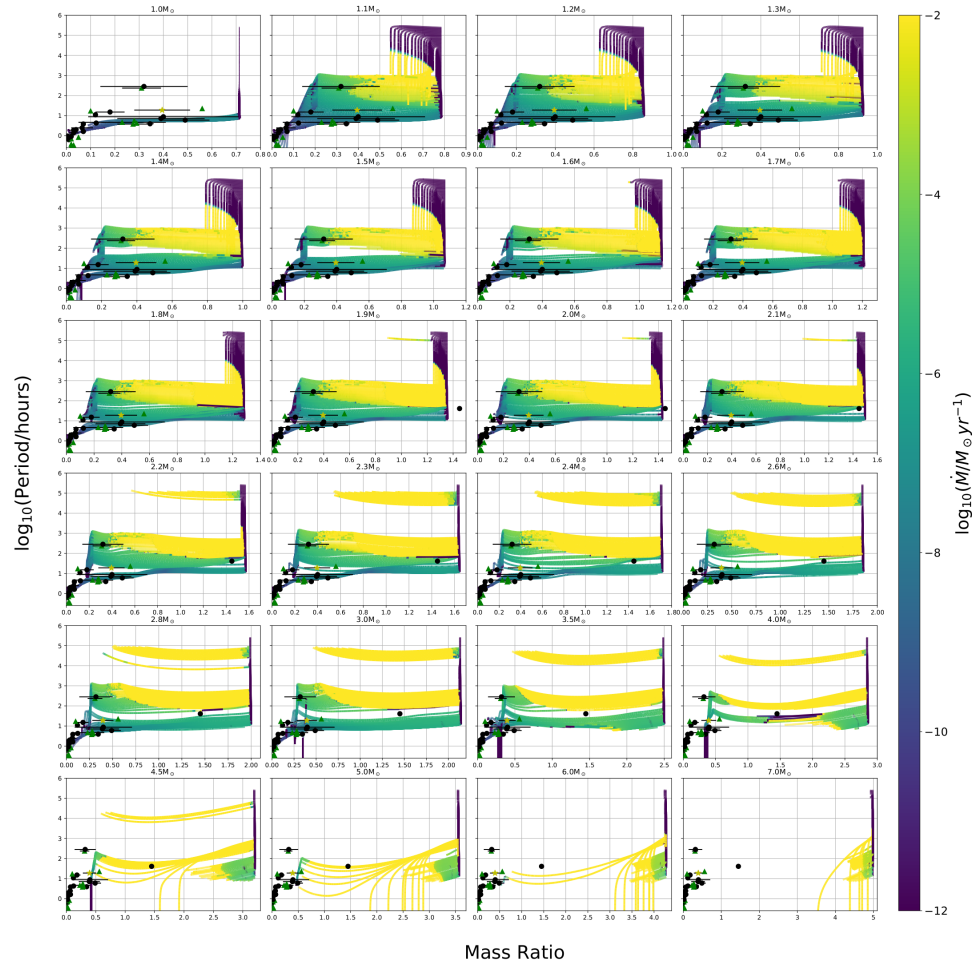


Figure 2.4: A similar figure to 2.2 using case 3, intermediate MB from Table 2.1. Note that the mass transfer rates are substantially higher than in the previous cases, Figs. 2.2 and 2.3.

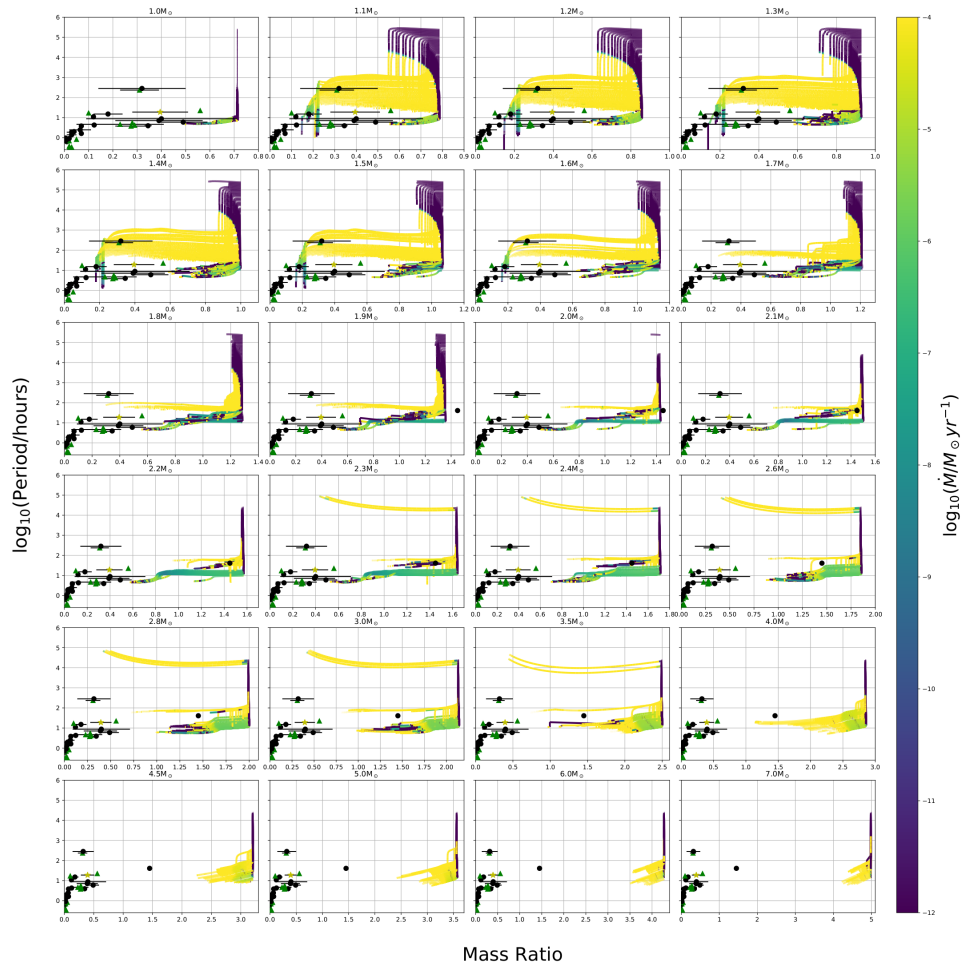


Figure 2.5: A similar figure to 2.2 using case 4, wind boost MB from Table 2.1. Here the mass transfer rates are extremely high.

## Convection Boosted

From Figure 2.3, we cannot see many differences between the default MB and the “convection boosted” MB. One difference between the default and convection boosted MB schemes is that evolutionary tracks run through the region  $q < 0.4$ ,  $1 \lesssim \log_{10}(P) \lesssim 2.5$ . The additional systems passing through this region cause some ambiguity in determining bifurcation periods in systems with initial donor masses  $M \lesssim 1.5M_\odot$ , since the binaries near the bifurcation period show very little change in period over their evolution.

## Intermediate

The “Intermediate” case includes the additional scaling factor which accounts for the effects of wind mass loss as seen in equation 2.20. Figure 2.4 shows the behaviour of the binary systems with this MB prescription. The additional wind scaling plays a significant role in wider binary systems. The stronger MB scheme brings the binary systems together on a shorter timescale. In these systems, the MB and total angular momentum loss are consistently an order of magnitude higher than the default case. Therefore, the system loses enough angular momentum due to MB that gravitational radiation comes into play once MB stops.

## Wind Boosted

The “wind boost” case shown in figure 2.5, includes the effects of the convective turnover time and accounts for the rotation rate of the star. In this case, the individual values of magnetic field strength as calculated using equation 2.17, the turnover time, and the wind mass loss rates are all within reasonable ranges. The magnetic field, which reaches a maximum of 100G shown in Figure 2.6, is within the range expected for giant stars (Aurière et al., 2015). The convective turnover time is also similar to those calculated by Pavlovskii and Ivanova (2015) for systems that are predicted to reproduce Sco X-1. It appears

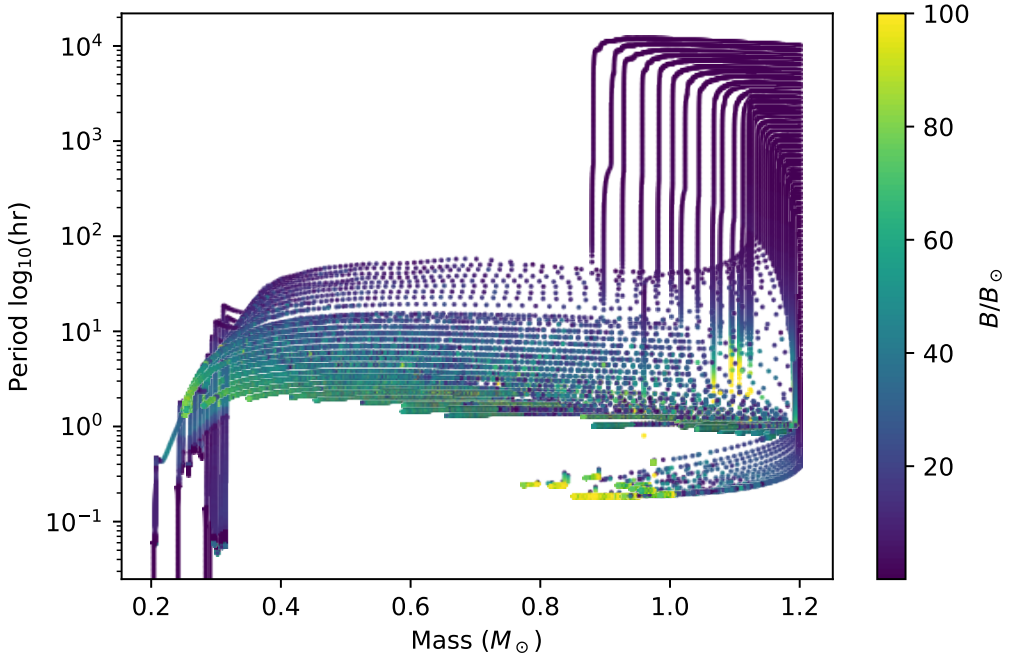


Figure 2.6: A figure showing the evolutionary tracks of a binary system consisting of a  $1.2M_{\odot}$  initial mass donor with a  $1.4M_{\odot}$  NS at a variety of initial periods using the wind boosted MB. The colour bar shows the magnetic field strength of the donor star at a given point in the binary evolution. The magnetic field is given in units of the solar magnetic field, which is  $\sim 1G$ .

that the individual properties are all within reasonable ranges. However, the combination of all these boost factors produces MB that is too strong, resulting in MT that consistently exceeds  $1M_{\odot} \text{ yr}^{-1}$ . MT at these rates results in evolution on a dynamical timescale, and as such the results from this highly boosted MB should not be trusted. It is likely that this prescription has reached and exceeded a saturation limit that is not accounted for in this work (Mestel and Spruit, 1987). It has been shown that in cases where the rotation rate is high, additional magnetic field structure effects must be included to dampen the angular momentum loss (Ivanova and Taam, 2003). For completeness, we include the results from the wind-boosted case, but since the MT rate is so high, it is unlikely these simulations accurately describe reality.

## 2.4.2 Binary Properties

Figure 2.7 shows evolutionary tracks in the donor mass-period plane with the colour of each point representing the neutron star mass at that point. If a system experiences MT below the Eddington limit, the accretor mass can grow significantly. The significant increase in mass is a common outcome for default Skumanich MB, and the convection boosted cases, where most of the LMXBs evolve to contain a NS more massive than  $2M_{\odot}$ . A “stronger MB”, such as our intermediate case, produces fewer systems where NS masses have increased significantly, due to the MT exceeding the Eddington limit for portions of the evolution. The lack of substantial accretion of material onto the NS is even more apparent in the wind-boosted case where there is no significant increase in mass despite the large decrease in donor mass. However, the wind-boosted systems generally die too quickly – most simulations don’t reach the relevant M, P range for the majority of observed binaries. From observations there is a lack of NS detected near  $2.0M_{\odot}$  with the most massive detected at  $2.01 \pm 0.04M_{\odot}$  (Antoniadis et al., 2013). The results shown in the default and convection boosted case suggest that all short period binaries contain a NS with a mass exceeding  $2.0M_{\odot}$ , whereas observations have found that these systems contain NS accretors in the range of  $1.4M_{\odot}$ . This preliminary result strongly supports the stronger MB prescriptions over the weaker convection boost and default cases.

Measurement of the surface chemical composition is possible in select binary systems. In binary systems involving white dwarf accretors, the surface chemical abundances can constrain the possible formation channels, with high  $N/C > 10$  or  $N/O \gtrsim 10$  implying a helium donor (Nelemans et al., 2010). Uncertainties in model spectra for UCXBs result in unreliable abundance ratios (Werner et al., 2006). The existence of strong C and O lines but weak He and N lines imply a helium donor star. However, in many cases more detailed observations are necessary to classify the possible donors (Nelemans et al., 2010).

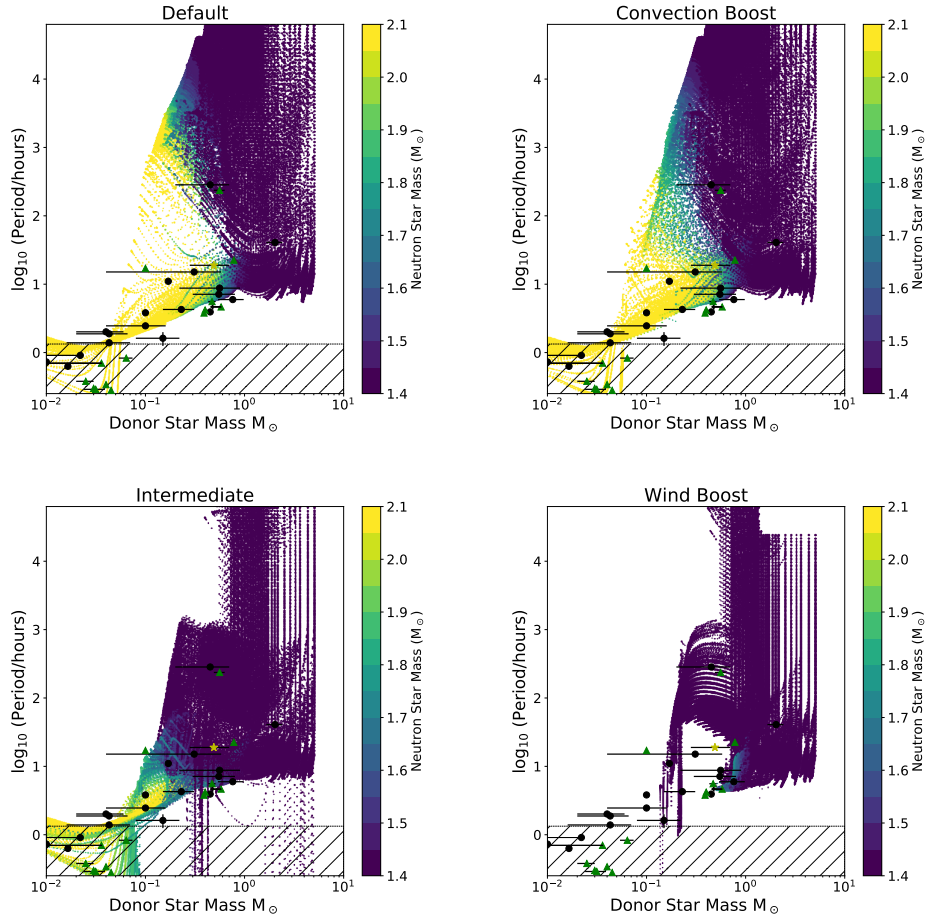


Figure 2.7: A scatter plot showing the changes in NS mass during the evolution of our systems. The lower hashed area shows the periods corresponding to ultra compact sources. The default and convection boosted cases suggest that all short period binaries contain a massive NS.

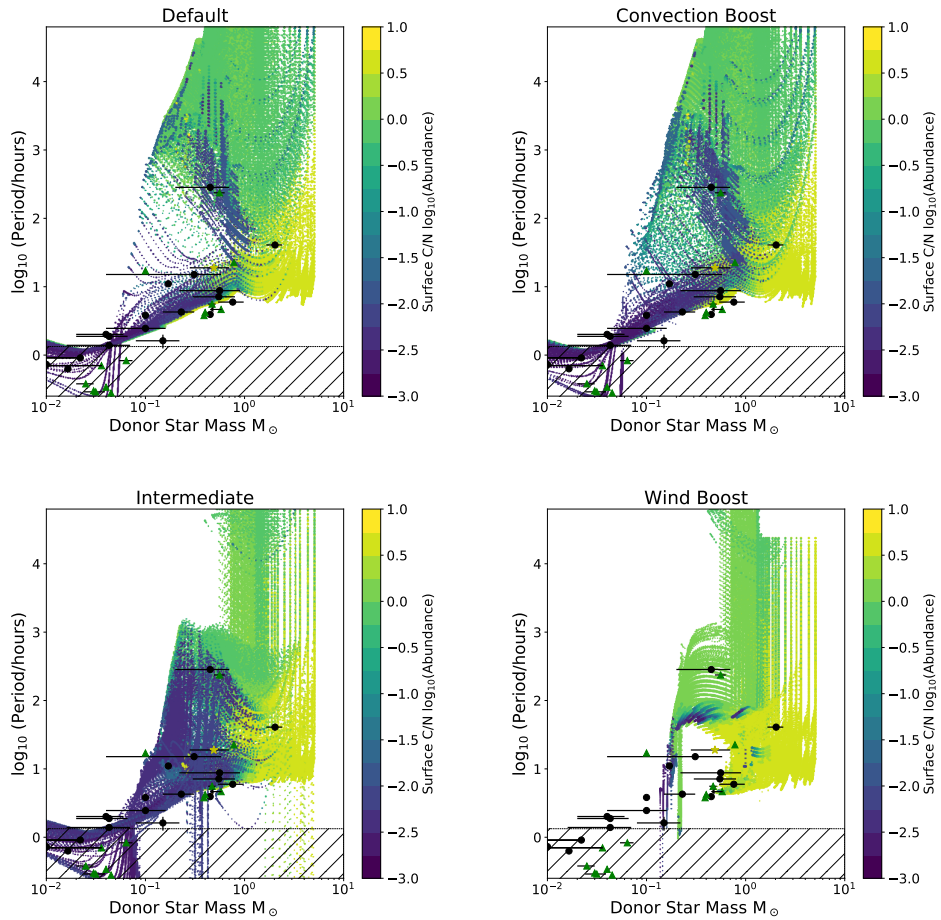


Figure 2.8: The surface C/N abundance mass fraction of the donor star. The initial C/N ratio of a star is  $\sim 3.36$  or  $\sim 0.53$  on the log scale.

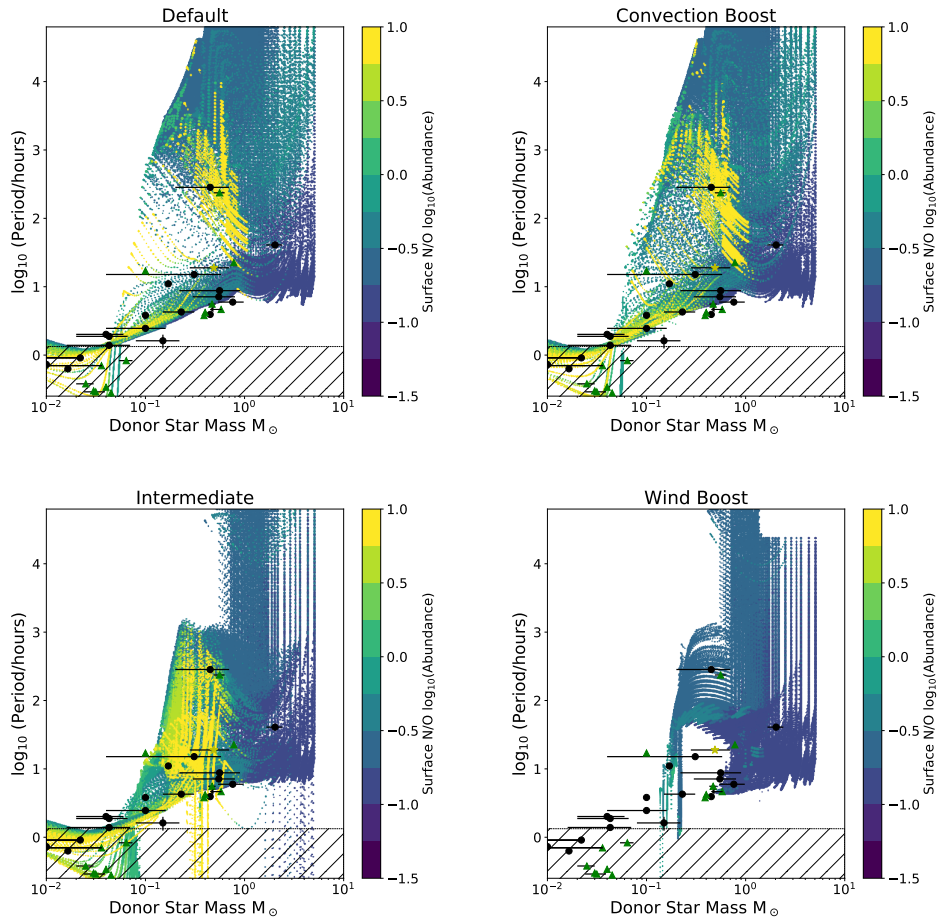


Figure 2.9: The surface N/O abundance mass fraction of the donor star. The initial N/O ratio of a star is 0.108 or  $\sim -0.96$  on the log scale.

Figures 2.8 and 2.9 show the C/N and N/O surface ratios from the simulated systems, respectively. In our donors, the initial C:N:O ratio is 0.37:0.108:1.0.

This change of abundance indicates where the donor star is in its evolution. In systems with a lower-mass donor,  $M \sim 1M_{\odot}$ , the donors show high N abundances as the donor star is stripped of C and O. In binaries with more massive donors,  $M \gtrsim 1.5M_{\odot}$ , the CN and CNO cycles can result in substantial changes in chemical composition. These significant changes can be observed in the material that is being transferred in these compact binaries.

### 2.4.3 Relative Densities

Figure 2.10 shows the data plotted in the period-MT plane with the colour bar representing a normalized frequency. Here we can see which systems are more or less likely to appear in each respective bin. We calculate frequency as follows:

1.  $\tau_{\text{tot}}^{mn}$  is the total evolution time of a binary system, as defined by the initial  $m$ -period and  $n$ -mass.
2.  $\tau_{ij}^{mn}$  is the time that a system defined by the initial  $m$ -period and  $n$ -mass spends in an  $i$ -period bin and a  $j$ -MT rate bin.
3.  $f_{ij}^{mn} = \tau_{ij}^{mn}/\tau_{\text{tot}}^{mn}$  is the fraction of time (or frequency) that a particular system (given by an initial  $mn$ ) appears in a bin defined by a particular  $i$ -period and  $j$ -MT rate.
4.  $f_{ij} = \max(f_{ij}^{mn})$  the frequency plotted in Fig. 2.10, is the maximum frequency of all systems to appear in a particular  $i,j$  bin.

The frequency gives an indication of where the evolutionary tracks spend the maximum amount of time during the evolution in the period-MT plane. This frequency however, does not necessarily represent a likelihood of detecting

a binary in said bin as we have neglected effects of how likely a binary is to form and the number of systems which may cross through a bin. This is done to avoid equating regions where many systems cross into a bin for short periods of time to regions where one system spends a large fraction of its lifetime. For example, using this method, a bin where one binary spend  $10^7$  years out of its total lifetime within the parameter space results in a much higher frequency than a bin where 1000 binaries each spend  $10^4$  years.

We see the densest regions of the figure are at short periods, with low MT rates. These systems correspond to the binaries that have shrinking periods over the course of their evolution, including ultra-compact binaries. In general, the higher the MT rate, the lower the frequency; this is not surprising as it is difficult to maintain high MT rates. In the default MB, there is a gap in the simulated density between  $0.5 \lesssim \log_{10}(P/\text{hr}) \lesssim 1.0$  and  $\log_{10}(\dot{M}/M_\odot \text{yr}^{-1}) \lesssim -11$ . While there are no observed systems in this range, this gap begins to get populated once convection is accounted for and is filled in with the “intermediate” prescription. In general, as the MB boost is increased, the MT rate at lower periods is also increased. The “convection boost”, “intermediate” and “wind boost” cases appear to more effectively reproduce the systems with periods  $\log_{10}(P/\text{hr}) \sim 1$  and MTs near the Eddington limit. These systems include GX 9+9, 4U 1735+444, and 2A 1822-371, which do not overlap with any simulated systems in figure 2.10. Sco X-1, on the other hand, appears to be reproducible in figure 2.10, as there is significant overlap with the simulated systems in the period-MT plane. We argue, however, that to reproduce an observed LMXB, in addition to the period and MT rate, we must also match the mass ratio of the system.

## 2.5 Comparison to the observed population of LMXBs

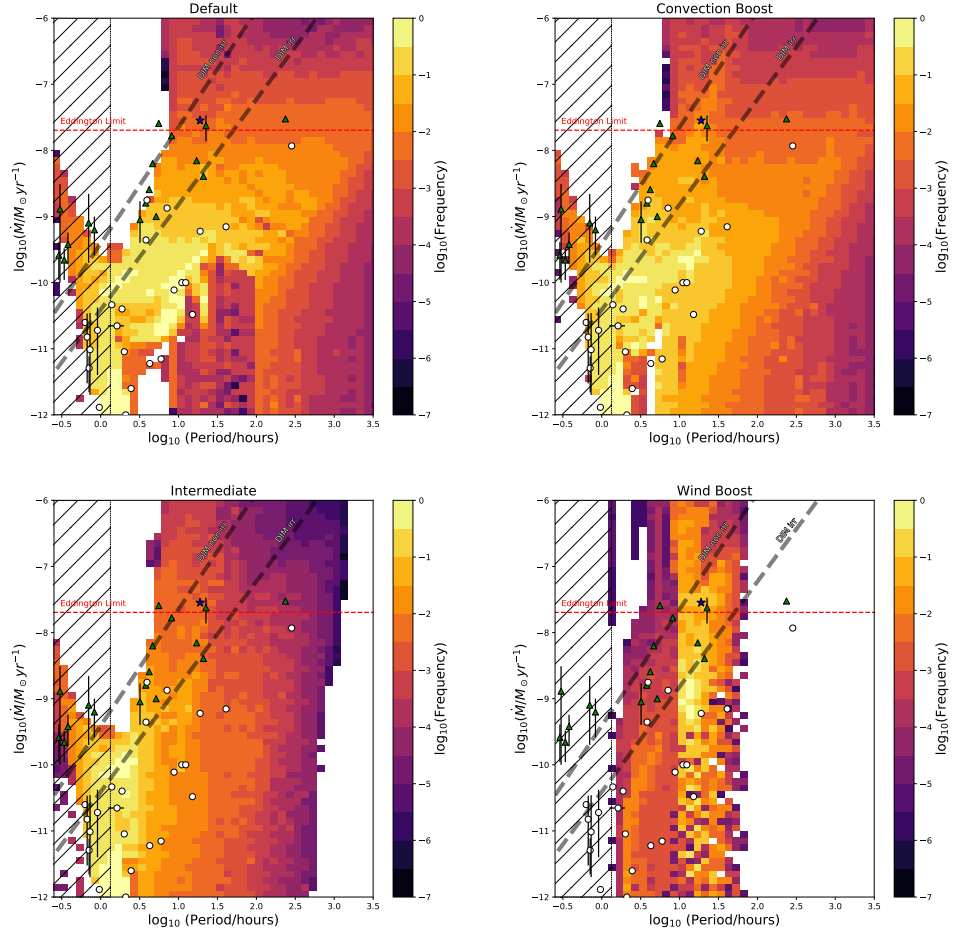


Figure 2.10: The relative probability of finding a system at a given point in our parameter space, assuming a the initial distribution of binaries from section 2.2.1. The symbols on the plot represent the observed systems with their given errors (see Table 2.3). Circles are transient systems and triangles are persistent systems. The single star point is the binary Sco X-1. The two grey dashed lines represent the critical MT rates for thermal-viscous accretion stability using an NS mass of  $1.4M_{\odot}$  (Coriat et al., 2012). These two lines are denoted with “DIM non irr” for the critical MT rate without the effects of irradiation while “DIM irr” is the critical MT rate with the effects of irradiation. Binaries that lie above the line are predicted to be persistent LMXBs while systems below are transient. The left hashed area represents the period range for ultra-compact sources.

System Name	$\log_{10}(P)$	q	$\log_{10}(\dot{M}_a)$
Ultra-compact XRBs			
4U 0513-40	[-0.57, -0.52]	[0.01, 0.06]	[-9.2, -8.6]
2S 0918-549	[-0.56, -0.51]	[0.01, 0.06]	[-9.8, -8.6]
4U 1543-624	[-0.54, -0.49]	[0.01, 0.06]	[-9.1, -8.6]
4U 1850-087	[-0.48, -0.43]	[0.01, 0.06]	[-10.0, -8.4]
M15 X-2	[-0.44, -0.39]	[0.01, 0.06]	[-9.7, -9.1]
4U 1626-67	[-0.17, -0.12]	[0.01, 0.06]	[-9.7, -8.6]
4U 1916-053	[-0.10, -0.05]	[0.03, 0.08]	[-9.6, -8.9]
4U 1636-536	[0.56, 0.61]	[0.15, 0.40]	[-9.1, -8.6]
GX 9+9	[0.60, 0.65]	[0.20, 0.33]	[-8.7, -8.2]
4U 1735-444	[0.65, 0.70]	[0.29, 0.48]	[-8.4, -7.9]
2A 1822-371	[0.73, 0.78]	[0.26, 0.36]	[-7.8, -7.3]
Sco X-1	[1.26, 1.31]	[0.15, 0.58]	[-7.8, -7.3]
GX 349+2	[1.33, 1.38]	[0.39, 0.65]	[-8.0, -7.3]
Cyg X-2	[2.35, 2.40]	[0.25, 0.53]	[-7.7, -7.2]

Table 2.4: The binned properties of selected persistent NS LMXBs. The periods are in hours, the mass accretion rate  $\dot{M}_a$  is in  $M_\odot \text{ yr}^{-1}$ . The default bins' ranges are 0.05 in  $\log_{10} P$  and 0.5 in  $\log_{10} \dot{M}$ , centred around the measured observed values. Ranges are increased if observational uncertainties are larger than the default ranges. The ranges for mass ratios, if those were not provided with an error, are such that they could accommodate the plausible error in NS mass, from  $1.4 M_\odot$  to the range in  $1.2 - 2 M_\odot$ .

System Name	$\log_{10}(P)$	q	$\log_{10}(\dot{M}_a)$
HETE J1900.1-2455	[0.12, 0.17]	[0.01, 0.06]	[-10.5, -10.0]
1A 1744-361*	[0.19, 0.24]	[0.05, 0.18]	[-11.7, -10.7]
SAX J1808-3658	[0.28, 0.33]	[0.02, 0.07]	[-11.0, -10.5]
IGR 00291+5394	[0.37, 0.42]	[0.02, 0.13]	[-11.8, -11.3]
EXO 0748-676*	[0.56, 0.61]	[0.05, 0.10]	[-9.3, -8.3]
4U 1254-69	[0.57, 0.62]	[0.23, 0.38]	[-9.0, -8.5]
XTE J1814-338*	[0.61, 0.66]	[0.10, 0.27]	[-11.2, -10.2]
XTE J2123-058*	[0.76, 0.81]	[0.27, 0.82]	[-11.2, -10.2]
X 1658-298	[0.83, 0.88]	[0.15, 0.67]	[-9.1, -8.6]
SAX J1748.9-2021	[0.92, 0.97]	[0.06, 0.83]	[-10.3, -9.8]
IGR J18245-2452	[1.02, 1.07]	[0.09, 0.14]	[-10.2, -9.7]
Cen X-4	[1.16, 1.21]	[0.02, 0.48]	[-10.6, -10.1]
Her X-1	[1.59, 1.64]	[0.83, 2.00]	[-8.1, -7.6]
GRO J1744-28	[2.43, 2.48]	[0.25, 0.53]	[-8.2, -7.7]

Table 2.5: The adopted ranges of selected transient NS LMXBs. Quantities are as in Table 2.4 except in systems with a \* symbol. The mass transfer bins in these systems use the upper limit listed, and span  $\log_{10} \dot{M} = 1.0$ .

C<sub>7</sub>

System Name	Default		Convection Boosted		Intermediate		Wind Boost	
	$\tau_{\max}$ [years]	$A_{\text{sys}}/A_{\text{tot}}$						
4U 0513-40	$3.23 \times 10^6$	$4.75 \times 10^{-4}$	$1.24 \times 10^6$	$7.91 \times 10^{-4}$	$4.00 \times 10^6$	$1.90 \times 10^{-3}$	0	0
2S 0918-549	$4.09 \times 10^6$	$4.75 \times 10^{-4}$	$2.30 \times 10^6$	$7.91 \times 10^{-4}$	$4.40 \times 10^6$	$2.06 \times 10^{-3}$	0	0
4U 1543-624	$4.83 \times 10^6$	$6.33 \times 10^{-4}$	$4.80 \times 10^6$	$6.33 \times 10^{-4}$	$7.91 \times 10^6$	$2.06 \times 10^{-3}$	0	0
4U 1850-087	$8.33 \times 10^6$	$6.33 \times 10^{-4}$	$8.83 \times 10^6$	$1.11 \times 10^{-3}$	$1.28 \times 10^7$	$2.06 \times 10^{-3}$	0	0
M15 X-2	$1.21 \times 10^7$	$6.33 \times 10^{-4}$	$1.11 \times 10^7$	$1.27 \times 10^{-3}$	$1.41 \times 10^7$	$2.22 \times 10^{-3}$	0	0
4U 1626-67	$6.76 \times 10^7$	$9.50 \times 10^{-4}$	$1.06 \times 10^8$	$1.58 \times 10^{-3}$	$7.48 \times 10^7$	$6.33 \times 10^{-4}$	0	0
4U 1916-053	$1.85 \times 10^7$	$1.58 \times 10^{-4}$	$1.21 \times 10^7$	$3.17 \times 10^{-4}$	$3.76 \times 10^7$	$4.75 \times 10^{-4}$	0	0
4U 1636-536	$1.22 \times 10^8$	$4.23 \times 10^{-2}$	$6.24 \times 10^7$	$1.91 \times 10^{-2}$	$4.39 \times 10^7$	$7.74 \times 10^{-2}$	$1.22 \times 10^5$	$2.06 \times 10^{-3}$
GX 9+9	0	0	$3.38 \times 10^7$	$1.60 \times 10^{-2}$	$3.73 \times 10^7$	$5.89 \times 10^{-2}$	$1.85 \times 10^4$	$1.27 \times 10^{-3}$
4U 1735-444	0	0	$1.48 \times 10^7$	$5.70 \times 10^{-3}$	$9.83 \times 10^6$	$2.26 \times 10^{-2}$	0	0
2A 1822-371	0	0	0	0	$5.26 \times 10^6$	$3.39 \times 10^{-2}$	0	0
Sco X-1	0	0	$1.69 \times 10^7$	$3.48 \times 10^{-3}$	$1.75 \times 10^6$	$3.91 \times 10^{-2}$	$2.71 \times 10^3$	$2.37 \times 10^{-3}$
GX 349+2	$4.09 \times 10^5$	$7.91 \times 10^{-4}$	$1.50 \times 10^7$	$6.17 \times 10^{-3}$	$1.91 \times 10^5$	$2.37 \times 10^{-3}$	0	0
Cyg X-2	$1.65 \times 10^6$	$8.39 \times 10^{-3}$	$2.56 \times 10^6$	$1.74 \times 10^{-2}$	$2.00 \times 10^5$	$1.28 \times 10^{-2}$	0	0
HETE J1900.1-2455	$5.61 \times 10^8$	$6.61 \times 10^{-2}$	$3.05 \times 10^8$	$4.57 \times 10^{-2}$	$5.87 \times 10^8$	$1.01 \times 10^{-1}$	0	0
1A 1744-361*	$1.99 \times 10^6$	$1.58 \times 10^{-4}$	$3.51 \times 10^7$	$1.58 \times 10^{-4}$	$6.80 \times 10^7$	$7.91 \times 10^{-4}$	0	0
SAX J1808-3658	$5.49 \times 10^7$	$6.33 \times 10^{-4}$	$1.05 \times 10^8$	$6.33 \times 10^{-4}$	$1.66 \times 10^8$	$1.74 \times 10^{-3}$	0	0

IGR 00291+5394	0	0	0	0	$1.88 \times 10^8$	$4.75 \times 10^{-4}$	0	0
EXO 0748-676*	0	0	$4.09 \times 10^7$	$2.53 \times 10^{-3}$	0	0	0	0
4U 1254-69	$5.23 \times 10^7$	$1.28 \times 10^{-2}$	$1.06 \times 10^6$	$7.91 \times 10^{-4}$	$1.70 \times 10^7$	$1.65 \times 10^{-2}$	0	0
XTE J1814-338*	0	0	0	0	0	0	$2.60 \times 10^5$	$1.27 \times 10^{-3}$
XTE J2123-058*	0	0	0	0	$1.40 \times 10^3$	$1.58 \times 10^{-3}$	$2.25 \times 10^2$	$2.53 \times 10^{-3}$
X 1658-298	$1.19 \times 10^8$	$1.30 \times 10^{-2}$	$2.85 \times 10^7$	$8.23 \times 10^{-3}$	$1.55 \times 10^7$	$4.91 \times 10^{-3}$	$2.26 \times 10^4$	$3.17 \times 10^{-3}$
SAX J1748.9-2021	$7.55 \times 10^8$	$6.33 \times 10^{-4}$	$3.08 \times 10^8$	$1.27 \times 10^{-3}$	$4.92 \times 10^7$	$1.39 \times 10^{-2}$	$8.96 \times 10^4$	$2.69 \times 10^{-3}$
IGR J18245-2452	$8.91 \times 10^8$	$6.33 \times 10^{-4}$	0	0	$3.82 \times 10^7$	$2.37 \times 10^{-3}$	0	0
Cen X-4	0	0	$1.14 \times 10^8$	$1.58 \times 10^{-4}$	$3.53 \times 10^7$	$1.58 \times 10^{-2}$	$4.32 \times 10^3$	$1.11 \times 10^{-3}$
Her X-1	$7.38 \times 10^6$	$1.27 \times 10^{-3}$	$9.97 \times 10^6$	$1.27 \times 10^{-3}$	$5.68 \times 10^5$	$1.42 \times 10^{-3}$	$4.75 \times 10^5$	$2.69 \times 10^{-3}$
GRO J1744-28	$5.85 \times 10^6$	$8.70 \times 10^{-3}$	$5.48 \times 10^6$	$1.31 \times 10^{-2}$	$6.98 \times 10^4$	$5.70 \times 10^{-3}$	0	0

Table 2.6: For each observed system (and thus parameter space bin), we give the maximum amount of time,  $\tau_{\max}$ , that any simulated system spends in a given bin, and the fraction of the parameter space of simulated binaries which resemble the observed system,  $A_{\text{sys}}/A_{\text{tot}}$ . Our bins are defined in tables 2.4 and 2.5. The total parameter space  $A_{\text{tot}}$  spans the mass range from  $1 \leq M/M_{\odot} \leq 7$  and the period range from  $-0.5 \leq \log_{10}(P/\text{days}) \leq 4$ . The \* denotes systems where only an upper limit for the mass transfer rate is given.

We describe a set of binary systems that have an observationally determined MT rate, orbital period, and mass ratio (see Table 2.3, not all observed systems can be used). We bin each binary system within a range of period, MT and mass ratio, with the observed values used as the central bin values. These bins are then used to analyze the systems, and the adopted range for  $P$ ,  $\dot{M}$  and  $q$  are described in Tables 2.4 and 2.5. The “observational” bin sizes are large enough to accommodate the anticipated observational errors.

The likelihood of a given MB scheme being correct depends on how effectively it can reproduce the observed binary systems. To find this value, we check if a simulated MT system passes through any of the “observational” bins. If a simulated system passes through one of the observational bins, we can find the total time that the system spent  $\tau_{ij}^n$  in that “observational” bin. Here,  $n$  stands for the number of the “observational” bin, and  $ij$  describes the initial orbital period and the initial mass of the donor. We then find the size of the initial parameter space in the initial orbital periods and the donor masses, the parameter space from which the systems could evolve through the particular “observational” bin  $n$ .

In Table 2.6 we provide the maximum amount of time,  $\tau_{\max}^n$  that any of the simulated systems can spend in the  $n$  observational bin of interest, and the fraction of the initial parameter space that can produce the observed systems. These results are separated by MB prescription, with the wind-boosted case producing clearly ineffective results. With the high MT rate, the simulated parameter space overlaps with very few observed data points in 2.5 and 2.10. This high boost rate is likely invalid, and including a dampening factor should yield more realistic results.

The most striking result is that the default Skumanich MB law cannot reproduce most of the persistent systems - in fact, no observed persistent LMXBs with orbital periods between about 4.5 and 23 hours can be produced once we account for mass ratio. The main reason is that MB is not strong enough to

drive the observed MT rate. In principle, in addition to convection or wind-boosted MB laws, one can invoke also another alternative MB law to explain systems like Sco X-1 - as was done, e.g., by Chen (2017), who considered initial donors of  $1.5 - 2.5 M_{\odot}$  star and applied the MB law derived from Justham et al. (2006). The best fitting progenitor systems from Chen (2017) have  $1.6 - 1.8 M_{\odot}$  donors with a 300G fossil magnetic field. It would, however, be rather intriguing if most of the observed persistent systems must be descendants of low-mass A stars with magnetic fields about an order of magnitude weaker than that of Ap stars, but 100 times larger than that of regular stars.

A significant result is that while we can create UCXBs, the initial parameter space to form these systems, and the lifetimes of the systems in those data bins, suggest that binary systems with a NS accretor and a non-perturbed donor are unlikely to be the main progenitors. They are instead likely to be produced either in globular clusters via physical collisions of a NS with a red giant Ivanova et al. (2005), or as a result of common evolution in the field, where the MT can start either from a cooled-down stripped core or, conversely, from a hot stripped core (Heinke et al., 2013). While the UCXBs have low MT rates, the short time spent in the observed bin is due to the simulated binary having an MT rate near the boundary of the bin.

As the MB strength increases, the number of persistent systems that can be reproduced increases. The binaries that could not be reproduced by the default MB prescription, GX 9+9, 4U 1735-444 and Sco X-1, are those that Podsiadlowski et al. (2002) found had MT rates much higher than their simulations reached. The convection-boosted MB is necessary to reproduce these persistent systems. Similarly, the available evidence indicates that the MT rate of 2A 1822-371 is super-Eddington (Bak Nielsen et al., 2017). For 2A 1822-371, the convection-boosted case is still insufficient to reach the high MT observed. The wind-boosted case pushes the MT rate high enough to reproduce this system at an appropriate period. The mass ratio however, does not match with

the observed binary.

The reproducibility of a transient binary is affected by the choice of MB prescription. Unfortunately, unlike persistent systems, a clear trend isn't apparent from one prescription to another. Instead, different systems are reproduced by different MB prescriptions, and with the uncertainties in determining an average MT in these systems, we cannot use the transient binaries to reliably draw any conclusions without a clear trend. One result that can be seen from the reproducibility of the transient systems in Table 2.6 is that the systems that are most difficult to reproduce are those where the MT rate is only constrained by an upper limit. The intermediate case reproduces the largest number of observed transient systems with only EXO 0748-676 and XTE J1814-338 not being reproduced.

The wind-boosted MB simulations cannot reproduce the majority of the observed binaries regardless of whether they are persistent or transient. The wind-boost prescription gives very short lifetimes for all reproduced binaries (which makes their detection unlikely), and cannot reproduce the UCXBs. This suggests that the simulated wind-boosted case is exceeding some saturation point for MB and the systems are losing too much angular momentum too quickly.

### 2.5.1 Other effects

Irradiation may play a significant role in driving winds from the donor star (Ruderman et al., 1989), and in causing the donor star to expand to a larger radius than expected for its orbital period (Podsiadlowski, 1991). Such an increase in donor radius due to irradiation may cause cycles of increased MT rates (up to a factor of  $\sim 30$ ), followed by a decrease to below-average MT rates (e.g. Hameury et al., 1993). The detailed physics of such irradiation-driven MT cycles have not yet been established, but current work suggests that these cycles should require small convective timescales in the donor, and

thus may operate on systems with periods between 4 and 15 hours (Büning and Ritter, 2004). Irradiation-induced MT cycles could potentially produce the large observed MT rates in some of our transient and persistent systems in this period range, but should not be relevant for longer-period systems such as Sco X-1. Whether irradiation-induced MT can play a significant role depends on as-yet-undetermined details of the heating efficiency of the irradiating flux, and the fraction of time at the increased MT rate.

We have difficulty reproducing two transient systems (EXO 0748-676 and XTE J1814-338), both with orbital period near 4 hours, with any of our MB schemes. Our best MB scheme, the “intermediate” case, predicts MT rates higher than observed for these 2 systems. It is possible that irradiation-driven MT cycles might alter these systems’ evolution enough to match their observed characteristics (although such MT cycles are thought to cut off around 4 hours, Büning and Ritter 2004). An alternative possibility is that these systems may turn on as millisecond radio pulsars intermittently, during which they eject all mass transferred from their companion (Burderi et al., 2002, 2003), as the transitional millisecond pulsars appear to do (Archibald et al., 2009; Papitto et al., 2013). If so, the time-averaged MT rate onto their NSs would be lower than we calculate. There is indeed evidence that these two systems may be transitional millisecond pulsars. XTE J1814-338 is known to show accretion-induced X-ray pulsations (Markwardt and Swank, 2003). Its donor star also shows evidence of irradiation by an unknown energy source, which may be spin-down energy from a radio pulsar (Baglio et al., 2013; Wang et al., 2017). EXO 0748-676 has not shown detected X-ray pulsations (despite sensitive RXTE X-ray observations). However, a careful study during quiescence showed that no accretion disk was present, which may indicate that a transitional millisecond pulsar had turned on, and is ejecting transferred mass (Ratti et al., 2012).

## 2.6 Conclusions

In this work, we have examined how different MB prescriptions affect the evolution of LMXBs. The observational data to which we compare our simulations is given in section 2.3. By systematically studying the parameter space of interest, we cover a range of possible seed masses and periods for these binary systems. The results of comparing our simulations to the observations are given in sections 2.4 and 2.5. The key results of this work are:

- Using "weaker" MB schemes such as the default Skumanich prescription, and even the "convection boosted" case described in this work, results in an overabundance of highly massive NS accretors.
- The highest density region in our parameter space, as seen in figure 2.10, is the region of short periods and low MT rates. This high-density region is found in all MB prescriptions.
- In the default, convection boosted and intermediaite MB prescriptions, all UXCBs of interest can be reproduced. Although,  $\tau_{\max}$  is small suggesting these systems are difficult to form using this method.
- The "default" MB scheme reproduces results similar to Podsiadlowski et al. (2002). This weak MB scheme cannot reproduce some observed persistent systems in our simulations; these simulated binaries differ from observed binaries by up to an order of magnitude in MT rate.
- The "convection-boosted" prescription reproduces persistent systems much better than the default scheme, as it successfully simulates the properties of GX 9+9, 4U 1735-444 and Sco X-1. It cannot, however, reproduce the suspected super-Eddington system 2A 1822-371 (Bak Nielsen et al., 2017).

- Once we account for wind in the MB scheme, we can reach high enough MT rates to reproduce 2A 1822-371. Super-Eddington MT rates are achieved in the "intermediate" MB prescription.
- The intermediate prescription produces the largest number of observed transient LMXBs. Only EXO 0748-676 and XTE J1814-338 cannot be reproduced. These two systems only have an upper limit for mass transfer rate which may be the reason why these systems are difficult to reproduce.
- Including the effects of a non-thermal wind in our "wind boost" case results in very high MB. The high angular momentum loss results in MT rates that exceed  $1M_{\odot} \text{ yr}^{-1}$ . The "wind boost" case likely has reached and exceeded a saturation point with MB, and additional effects must be considered to dampen the angular momentum loss for this scheme.

The systematic mismatches between observed and predicted NS LMXB properties seen in previous work such as Podsiadlowski et al. (2002) are again found in our work when the default MB prescription is used. These discrepancies between observations and simulations begin to disappear, however, once we include the effects of convective turnover time and non-isothermal winds. With these changes, the MT rates approach those seen in observed systems, and our simulations more effectively reproduce the samples of persistent, and transient, binaries. With these results in mind, numerical studies of LMXBs that begin their calculations at long periods should no longer use the Skumanich prescription for MB as it does not adequately reproduce observed systems. Instead, the studies need to include additional effects in their MB schemes.

A clear extension of this work would be to include saturation effects in the MB prescription (Mestel and Spruit, 1987). One source of decreasing the MB strength that is not accounted for in this work, is the change in the magnetic field structure as the period of the system changes. It has been shown that in short period binaries a so-called 'dead zone' is produced, trapping wind mate-

rial (Mestel and Spruit, 1987; Ivanova and Taam, 2003). This trapped material cannot escape the system, reducing the angular momentum loss through MB. Additionally, the inclusion of irradiation-induced wind and more complex magnetic field structures, such as a dipolar field similar to what is done in Justham et al. (2006), is possible.

Possibilities for future analysis with the simulations produced for this work include the possibility of determining viable progenitors of observed LMXBs. Using the reproducibility search for observed systems in section 2.5, we can find a rough parameter space that produces progenitors for each of our LMXBs of interest for a given MB prescription. Finding the possible progenitors will act as a "reverse population synthesis" method, where instead of providing initial conditions, we use observed binaries and their progenitors to infer what the initial conditions may have been. The reverse population synthesis method cannot, however, be used with the simple Skumanich law, where many persistent systems are not reproduced.

## Acknowledgements

We would like to thank the anonymous referee for helpful comments. NI acknowledges support from the CRC program, funding from an NSERC Discovery grant, and acknowledges that a part of this work was performed at the KITP, which is supported in part by the NSF under grant No. NSF PHY17-48958. CH acknowledges support from an NSERC Discovery Grant, and an Accelerator Supplement. This research was enabled by the use of computing resources provided by WestGrid and Compute/Calcul Canada.

# Chapter 3

## Evolving LMXBs: CARB Magnetic Braking

Kenny. X. Van<sup>1</sup> and Natalia Ivanova<sup>1</sup>

<sup>1</sup>University of Alberta, Dept. of Physics, 11322-89 Ave, T6G 2E7, Canada;

kvan@ualberta.ca

*Received 2019 October 15; revised 2019 November 12; accepted 2019 November 13;*

*published 2019 November 27*

DOI: 10.3847/2041-8213/ab571c

### ABSTRACT

The formation of low-mass X-ray binaries (LMXBs) is an ongoing challenge in stellar evolution. One important subset of LMXBs are the binary systems with a neutron star (NS) accretor. In NS LMXBs with non-degenerate donors, the mass transfer is mainly driven by magnetic braking. Discrepancies between the observed and predicted mass transfer (MT) rates have been previously identified. Theoretical predictions of the MT rates are too low, by an order of magnitude or more. Recently, we showed that with standard magnetic braking, it is not possible to find progenitor binary systems such that they could reproduce – at any time of their evolution – most of the observed persistent NS LMXBs. In this *Letter* we present a modified magnetic braking prescription, CARB (Con-

vection And Rotation Boosted). CARB magnetic braking combines two recent improvements in understanding stellar magnetic fields and magnetized winds – the dependence of the magnetic field strength on the outer convective zone, and the dependence of the Alfvèn radius on the donor’s rotation. Using this new magnetic braking prescription, we can reproduce the observed mass transfer rates at the detected mass ratio and orbital period for all Galactic persistent NS LMXBs with detailed information on donors. For the systems where the effective temperature of the donor star is known, CARB theory agrees with observations as well.

*Unified Astronomy Theory concepts:* Binary stars (154); Stellar evolution (1599); Stellar evolutionary models (2046)

### 3.1 Introduction

Understanding the evolution of stars in binary systems relies heavily on the adopted laws of angular momentum loss which affect the change in orbital separation. One of the ways to lose angular momentum in a binary system is through magnetic braking (MB) (Verbunt and Zwaan, 1981). In this concept, the donor loses its angular momentum through a magnetized wind, and then, through tidal friction, replenishes the donor’s angular momentum using the orbital angular momentum. MB is the dominant angular momentum loss mechanism in binaries wider than a few hours in orbital period, whereas gravitational radiation dominates in close binaries (Rappaport et al., 1983). More recently, circumbinary disks have been shown to effectively remove angular momentum and reproduce ultra compact binaries (Ma and Li, 2009b). Unfortunately, circumbinary disks appear to be rare in LMXBs and there are significant uncertainties in the disk parameters (Ma and Li, 2009b). Additionally, our work includes systems with wider periods than UCXB,. As such, we will be focusing only on MB.

The choice of the adopted MB prescription has large overarching effects on the evolution of the binary – stronger MB will shrink a binary faster, resulting in a higher mass transfer (MT) rate. The most widely-used assumption in stellar simulations is the “Skumanich” MB (Skumanich, 1972); its application to binary systems is usually the form provided in Rappaport et al. (1983). The standard MB law, as well as some of its modifications, fails to reproduce the observed persistent NS LMXBs (Van et al., 2019). Examples of some modified MB schemes include those which focus on a subset of LMXBs such as Ap/Bp donors (Justham et al., 2006), or dampen the MB strength at high rotation rates (Sills et al., 2000; Ivanova and Taam, 2003).

Some advances in understanding the characteristics of the magnetized wind from a star were made recently. First, Réville et al. (2015) has included the effect of stellar rotation on the Alfvèn radius. Secondly, the convective turnover time has been linked to the strength of the surface magnetic field (Parker, 1971; Noyes et al., 1984; Ivanova, 2006). In §2, we derive the new CARB (Convection And Rotation Boosted) MB which takes into account both advances. In §3, we use the new MB to evolve the grid of progenitor binaries, in a similar manner as done in Van et al. (2019). In §4, we compare the results of the simulations with the observed persistent NS LMXBs. Finally, in §5 we summarize our key results in this *letter*.

## 3.2 Magnetic Braking

The loss of the angular momentum due to magnetic braking is derived following steps similar to those outlined in Van et al. (2019).

First, we assume spherical symmetry, which results in the angular momentum lost being

$$\dot{J}_{\text{MB}} = -\frac{2}{3}\Omega \dot{M}_W R_A^2. \quad (3.1)$$

$\dot{M}_W$  denotes the wind mass loss rate,  $\Omega$  is the rotation rate, and  $R_A$  is the Alfvèn radius. Assuming a radial magnetic field,

$$\left(\frac{R_A}{R}\right)^2 = \frac{B_s^2 R^2}{4\pi R_A^2 \rho_A v_A^2} = \frac{B_s^2 R^2}{\dot{M}_W v_A}. \quad (3.2)$$

Here  $R$  is the radius of the star,  $B_s$  is the surface magnetic field strength,  $v_a$  is Alfvèn velocity, and  $\rho_a$  is the density of the wind at the Alfvèn radius. Total mass loss with the wind is  $\dot{M}_W = 4\pi R_A^2 \rho_A v_A$ . The velocity of a normal stellar wind, when it reaches the Alfvèn radius, can be found from energy conservation, and expressed using the surface escape velocity  $v_{\text{esc}}$ :

$$\frac{v_A}{v_{\text{esc}}} = \left(\frac{R}{R_A}\right)^{1/2}. \quad (3.3)$$

In the case when the star and its attached magnetic field rotate, the regular stellar wind can also be additionally accelerated by the time it reaches the Alfvèn radius. This acceleration was tested by Matt et al. (2012) and was shown to have a non-negligible effect. Réville et al. (2015) parametrized the additional acceleration by replacing the surface escape velocity with a modified velocity, which includes the effects of rotation. Using this variable instead in Equation 3.2 gives us

$$\left(\frac{R_A}{R}\right)^3 = \frac{B_s^4 R^4}{\dot{M}_W^2} \times \frac{1}{v_{\text{esc}}^2 + 2\Omega^2 R^2 / K_2^2}, \quad (3.4)$$

where  $K_2 = 0.07$  in this equation is a constant obtained from a grid of simulations by Réville et al. (2015).  $K_2$  sets the limit where the rotation rate begins to play a significant role. In this approach, the Alfvèn radius shrinks as the rotation rate increases, weakening the angular momentum loss in fast rotating binaries. Plugging this form of the Alfvèn radius into the angular momentum equation gives a new prescription for angular momentum loss,

$$\dot{J}_{\text{MB}} = -\frac{2}{3}\Omega \dot{M}_W^{1/3} R^{14/3} B_s^{8/3} (v_{\text{esc}}^2 + 2\Omega^2 R^2 / K_2^2)^{-2/3}. \quad (3.5)$$

Substituting a convective turnover scaling relation for the magnetic field strength of the star (see Van et al., 2019, for a discussion as to why this is justified), we get the modified magnetic braking prescription used in our simulations,

$$\dot{J}_{\text{MB}} = -\frac{2}{3} \dot{M}_W^{1/3} R^{14/3} (v_{\text{esc}}^2 + 2\Omega^2 R^2 / K_2^2)^{-2/3} \times \Omega_\odot B_\odot^{8/3} \left(\frac{\Omega}{\Omega_\odot}\right)^{11/3} \left(\frac{\tau_{\text{conv}}}{\tau_{\odot,\text{conv}}}\right)^{8/3}. \quad (3.6)$$

The magnetic field strength on the surface of the Sun is on average  $B_s = 1$  G with a rotation rate and convective turnover time of  $\Omega_\odot \approx 3 \times 10^{-6}$  s<sup>-1</sup> and  $\tau_{\odot,\text{conv}} = 2.8 \times 10^6$  s, respectively. Both solar values used here were found using the same method from Van et al. (2019). The value used for  $\tau_{\odot,\text{conv}}$  is similar to those found by Ma and Li (2009a) and Landin et al. (2010) of 28.4d and 38.2d respectively. While our value deviates slightly from those found in other works, what is important is that our calculations are self-similar between different stars: the method used to calculate the normalization factor and the turnover time of each of our simulated systems is the same.

### 3.3 Evolution through the mass transfer

We follow the method described in Van et al. (2019) and test the MB on progenitor binaries seeded on a grid of periods and donor masses. The initial periods range from  $-0.4 \leq \log_{10}(P/\text{day}) \leq 4$  in steps of  $\Delta \log_{10}(P) = 0.05$ . The initial donor masses range from  $1.0 \leq M_d/M_\odot \leq 7.0$  with a variable step size. The donor mass has steps of  $\Delta M_d = 0.1M_\odot$  when  $M_d \leq 2.4M_\odot$ ,  $\Delta M_d = 0.2M_\odot$  for  $2.4 < M_d/M_\odot \leq 3$ ,  $\Delta M_d = 0.5M_\odot$  when  $3 < M_d/M_\odot \leq 5$  and  $\Delta M_d = 1.0M_\odot$  for any initial donor mass exceeding  $5M_\odot$ . The stars have initial metallicity  $Z = 0.02$ . All NSs start with a seed mass of  $M_{\text{NS}} = 1.4M_\odot$ . The chosen grid encompasses all binaries that could start the mass transfer at

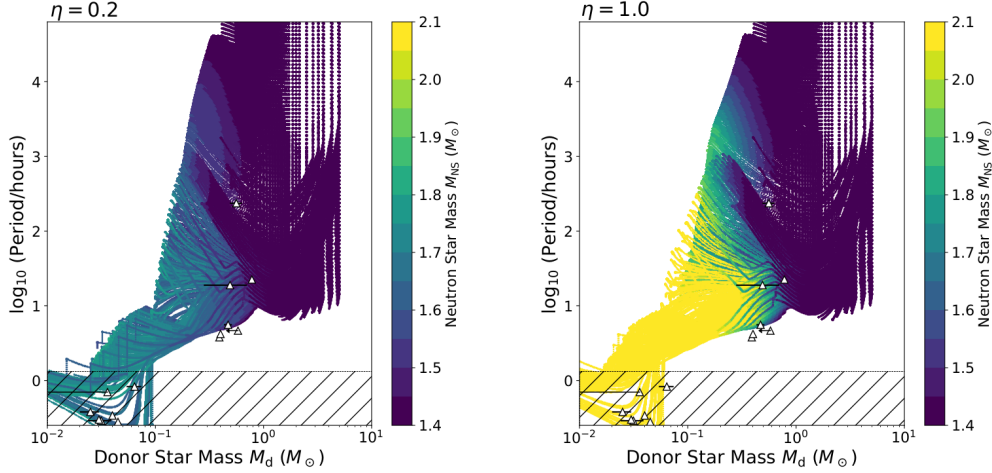


Figure 3.1: The evolution of  $M_{\text{NS}}$  during the mass transfer. The  $\eta$  value denotes the MT efficiency. The triangle symbols represent persistent LMXBs (data from Van et al., 2019).

some point of their evolution.

To evolve the initial binaries, we use the stellar code **MESA**<sup>1</sup> (Modules for Experiments in Stellar Astrophysics) revision 11701 (Paxton et al., 2011, 2013, 2015, 2018, 2019) and May 2019 release of **MESASDK**<sup>23</sup>.

Here, we refine the method described in Van et al. (2019) by taking into account the efficiency of the mass transfer. The rate of the mass gain of the NS  $\dot{M}_{\text{NS}}$  is proportional to the rate of the mass accretion  $\dot{M}_{\text{acc}}$ , but is less than that due to conversion of some accreted mass into gravitational binding energy:

$$\dot{M}_{\text{NS}} = \dot{M}_{\text{acc}} f_{\text{BE}} . \quad (3.7)$$

Here  $f_{\text{BE}}$  is the so-called binding energy factor. Depending on the equation of the state of the NS,  $f_{\text{BE}} \approx 0.85 - 0.90$  (Lattimer and Prakash, 2007). Some

<sup>1</sup><http://mesa.sourceforge.net>

<sup>2</sup><http://www.astro.wisc.edu/~townsend/static.php?ref=mesasdk>

<sup>3</sup>The modifications to MESA to include modified MB will be available on the MESA marketplace.

fraction of the material accreted onto the NS will be converted to gravitational binding energy and is controlled by  $f_{\text{BE}}$ .

In addition, not all mass transferred through  $L_1$  has to be accreted by the NS – it may be reduced by a number of effects, for example, the propeller effect is a mechanism where the magnetic field deflects away accreting material (Romanova et al., 2018). Indirect evidence for the accretion inefficiency comes from observations of millisecond pulsars. If the accretion rate was the same as the mass transfer rate  $\dot{M}_{\text{tr}}$ , many of these binaries are expected to contain high mass neutron stars. However, the observations do not support this (Antoniadis et al., 2012, 2016). An analytic description of the efficiency of mass transfer is not currently known. Antoniadis et al. (2012) calculated that accretion onto the pulsar PSR J1738+0333 had an efficiency  $\epsilon \sim 0.1 - 0.3$ , while a more recent statistical study looking at a number of pulsars estimated that their accretion efficiency was between  $\epsilon \sim 0.05 - 0.2$  (Antoniadis et al., 2016). We will combine the efficiency and the binding energy factor into one value  $\eta$ . The material accreted by the NS is less than that transferred,

$$\dot{M}_{\text{acc}} = \eta \dot{M}_{\text{tr}} . \quad (3.8)$$

In Figure 3.1 we demonstrate how the choice of  $\eta$  affects the mass of the final NSs. With  $\eta = 1$ , NSs in most systems become more massive than  $2M_\odot$ , once  $M_d < 0.4M_\odot$ . While  $M_{\text{NS}}$  is predicted to extend up to  $\approx 2.1 - 2.2M_\odot$  no NSs have accurately and reliably measured masses exceeding  $2.0M_\odot$  (Antoniadis et al., 2013; Cromartie et al., 2019; Rezzolla et al., 2018). The rarity of high mass NSs appears to contradict our results when assuming high efficiency. With  $\eta = 0.2$ , the maximum mass of the NS is of order  $M_{\text{NS}} \sim 1.8M_\odot$ . This value is within the range of  $1.1 \lesssim M_{\text{NS}}/M_\odot \lesssim 2$  for observed NSs (Özel and Freire, 2016). For our study in this *Letter*, we therefore adopt  $\eta = 0.2$ .

The efficiency factor will have a variety of effects on the binary system. The increased mass ejected from the system will increase the amount of angular momentum lost and limit how quickly  $M_{\text{NS}}$  grows. The efficiency controls how much material is accreted onto the compact object, which sets the luminosity of the system. The mass transfer efficiency is not constant throughout the entire evolution, and as a rough approximation we will estimate that the luminosity of our system can be approximated by  $L = 0.6G\dot{M}_{\text{tr}}M_{\text{NS}}/R_{\text{NS}}$ . We increase the size of our MT bins used in the analysis to compensate for the uncertainty in MT efficiency. If the  $\eta$  parameter used here were applied to the results from Van et al. (2019), the overall ability of a system to reproduce an observed LMXB would remain unchanged or decrease as the MT rate required to explain the observed X-ray luminosity may be increased.

### 3.4 Comparison with the observed population of LMXBs

It has been shown that the results of the MT simulations can be misleading in determining the legitimacy of adopted MB prescriptions if only two parameters are compared between simulated and observed systems (Pavlovskii and Ivanova, 2016). At least three parameters – for example, the period, the MT rate and the mass ratio – are necessary for determining if a given MB prescription is effective. The effective temperature of the donor could also play a significant role in discriminating the adopted MB laws (Justham et al., 2006).

It is hard to visualize the compatibility of three or more parameters in the same figure. In Figure 3.2, we show the maximum relative probability for any of the simulated MT systems to have a specific MT rate and orbital period, as well as the MT rates and orbital periods of observed persistent NS LMXBs (data is taken from Van et al., 2019). This relative probability, or frequency, is calculated using the following steps:

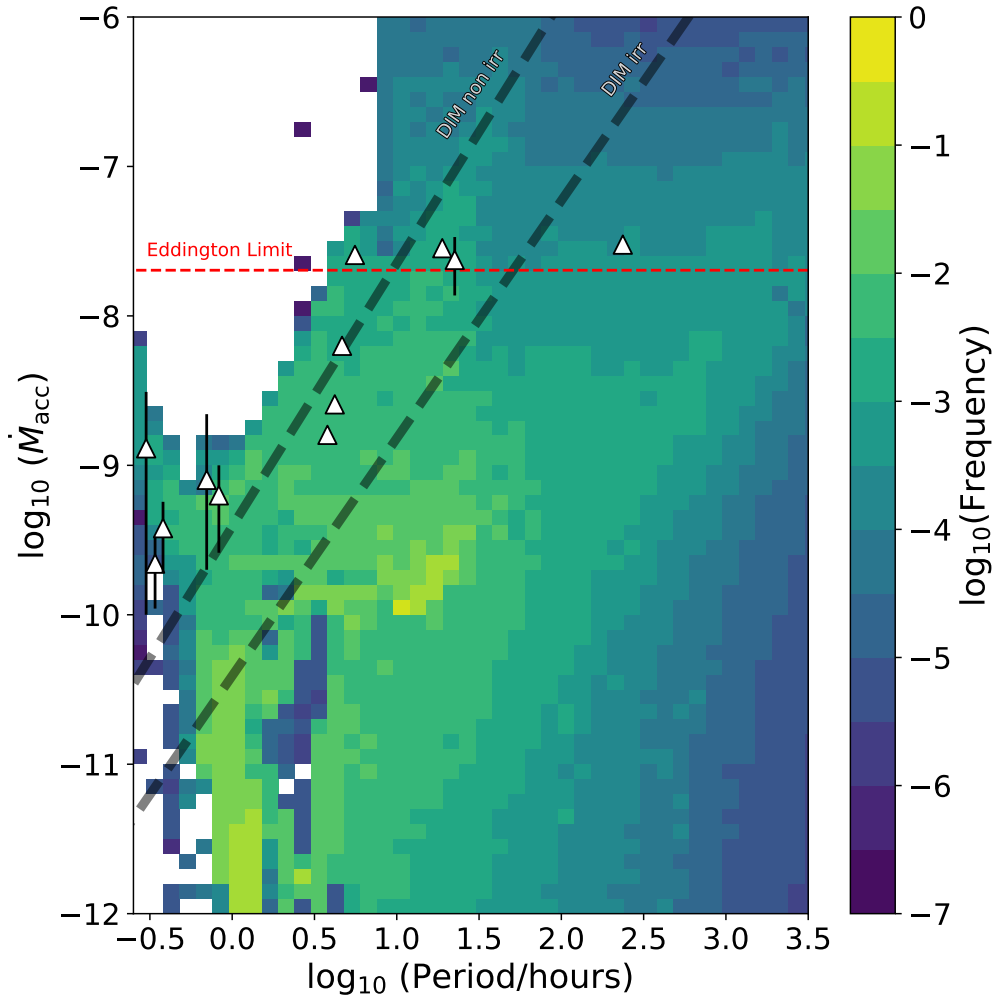


Figure 3.2: The relative probability of finding a system in a given bin in period-MT space. Each bin spans a width and height of 0.1 in  $\log_{10}(P)$  and  $\log_{10}(\dot{M}_{\text{acc}})$ . The symbols used are the same as in figure 3.1. The two grey dashed lines represent the critical MT separating persistent and transient systems for  $M_{\text{NS}} = 1.4M_{\odot}$  as described by the disk instability model (DIM) (Coriat et al., 2012). The upper line includes the effects of irradiation while the lower line does not.

1.  $\tau_{\text{tot}}^{mn}$  is the total evolutionary time of a binary system for an initial mass  $m$  and initial period  $n$ .
2.  $\tau_{ij}^{mn}$  is the amount of time the initial  $m, n$  binary spends in an observed  $i, j$  period and MT bin.
3.  $f_{ij}^{mn} = \tau_{ij}^{mn}/\tau_{\text{tot}}^{mn}$  is the frequency with which a given combination of mass and period appears in an observed bin of interest.
4.  $f_{ij} = \max(f_{ij}^{mn})$  is the maximum frequency from all the simulated binaries, and is plotted in Figure 3.2.

Within this period-MT parameter space, all of the observed persistent NS LMXBs appear to be reproducible by the simulated MT systems. This apparent match does not guarantee that the simulated systems will reproduce the observed systems when additional parameters are included.

Let us briefly describe the methodology for the comparison in 3-parameter space (for details, see Van et al., 2019). Each observed system is assigned a 3-dimensional cuboid, where the cuboid is roughly centred in the observed properties. The size of the cuboid in period is  $\delta \log_{10} P = 0.05$  and the size of the cuboid in mass ratio and MT rate depend on the uncertainty with which the observed value was determined, see Table 3.1.

System Name	$\log_{10}(P/\text{hr})$	q	$\log_{10}(\dot{M}_a)$	$\tau_{\max}$ (years)	$A_{\text{sys}}/A_{\text{tot}}$	$f_{\text{LMXB}}$
4U 0513-40	[-0.57, -0.52]	[0.01, 0.06]	[-9.0, -8.4]	$5.87 \times 10^6$	$1.72 \times 10^{-3}$	$4.38 \times 10^{-2}$
2S 0918-549	[-0.56, -0.51]	[0.01, 0.06]	[-9.6, -8.4]	$5.63 \times 10^6$	$1.72 \times 10^{-3}$	$4.38 \times 10^{-2}$
4U 1543-624	[-0.54, -0.49]	[0.01, 0.06]	[-8.9, -8.4]	$5.85 \times 10^6$	$1.54 \times 10^{-3}$	$4.38 \times 10^{-2}$
4U 1850-087	[-0.48, -0.43]	[0.01, 0.06]	[-9.8, -8.2]	$1.58 \times 10^7$	$2.92 \times 10^{-3}$	$8.82 \times 10^{-2}$
M15 X-2	[-0.44, -0.39]	[0.01, 0.06]	[-9.5, -8.9]	$2.43 \times 10^7$	$2.92 \times 10^{-3}$	$5.37 \times 10^{-2}$
4U 1626-67	[-0.17, -0.12]	[0.01, 0.06]	[-9.5, -8.4]	$7.39 \times 10^7$	$2.92 \times 10^{-3}$	$1.05 \times 10^{-1}$
4U 1916-053	[-0.10, -0.05]	[0.03, 0.08]	[-9.4, -8.7]	$6.14 \times 10^7$	$1.03 \times 10^{-3}$	$8.86 \times 10^{-2}$
4U 1636-536	[0.56, 0.61]	[0.15, 0.40]	[-8.9, -8.4]	$2.32 \times 10^7$	$5.49 \times 10^{-3}$	$5.85 \times 10^{-2}$
GX 9+9	[0.60, 0.65]	[0.20, 0.33]	[-8.5, -8.0]	$1.39 \times 10^7$	$4.46 \times 10^{-3}$	$9.11 \times 10^{-2}$
4U 1735-444	[0.65, 0.70]	[0.29, 0.48]	[-8.2, -7.7]	$1.11 \times 10^7$	$4.97 \times 10^{-3}$	$1.44 \times 10^{-2}$
2A 1822-371	[0.73, 0.78]	[0.26, 0.36]	[-7.6, -7.1]	$5.95 \times 10^6$	$6.69 \times 10^{-3}$	$7.06 \times 10^{-2}$
Sco X-1	[1.26, 1.31]	[0.15, 0.58]	[-7.8, -7.1]	$5.42 \times 10^6$	$1.20 \times 10^{-3}$	$4.32 \times 10^{-3}$
GX 349+2	[1.33, 1.38]	[0.39, 0.65]	[-7.8, -7.1]	$1.21 \times 10^7$	$4.46 \times 10^{-3}$	$4.25 \times 10^{-3}$
Cyg X-2	[2.35, 2.40]	[0.25, 0.53]	[-7.5, -7.0]	$7.99 \times 10^4$	$1.72 \times 10^{-3}$	$6.65 \times 10^{-4}$

Table 3.1: The binned properties of observed persistent NS LMXBs taken from Van et al. (2019). This table is adapted from Table 4 from Van et al. (2019). Again the periods are in hours and the mass accretion rate  $\dot{M}_a$  is in  $M_{\odot} \text{ yr}^{-1}$ . The bin ranges were chosen to span the errors in the given observed property with the bins centred on the observed values.  $\tau_{\max}$  is the maximum amount of time a given simulated system spends in the observed bin of interest.  $A_{\text{sys}}/A_{\text{tot}}$  is the fraction of our tested parameter space that can reproduce the system of interest. These two quantities give an indication to how long a simulation appears similar to an observed LMXB and how many systems could reproduce these properties.

We can find the maximum time that an individual simulation spends in a bin of interest,  $\tau_{\max}$ , and what fraction of their MT evolution they spend in the given bin,  $f_{\text{LMXB}}$ . We also can find the fractional area of the initial parameter space that reproduces the binary  $A_{\text{sys}}/A_{\text{tot}}$ . These three numbers can indicate how plausible it is to produce the observed NS LMXBs. The value of  $\tau_{\max}$  indicates how long a system can remain in this state, and thus how likely it is to be detected.  $A_{\text{sys}}/A_{\text{tot}}$  shows how stringent the initial parameter space is for reproducing a given LMXB. A larger  $A_{\text{sys}}/A_{\text{tot}}$  implies that many systems can reproduce an observed system.  $A_{\text{tot}}$  spans our entire parameter space of seed masses and periods. In our case  $A_{\text{tot}} = 29.1475$ . For example, we find that Cyg X-2 only has 2 progenitor systems, these two progenitor systems span a total area of  $A_{\text{sys}} = 0.05$  which results in  $A_{\text{sys}}/A_{\text{tot}} = 1.72 \times 10^{-3}$ .

As has been shown by Van et al. (2019), once the constraint on the mass ratio is added, none of the previously used MB prescriptions can produce all of the observed persistent NS LMXBs, despite considering all possible initial binaries. For the non-reproducible systems,  $A_{\text{sys}}/A_{\text{tot}} = 0$ . In Table 3.1 we present the results for the CARB MB prescription. It is fascinating that with the modified MB prescription, all persistent LMXBs can be reproduced.

We can further constrain the progenitors by looking at the effective temperature of the donor star. Determining the temperature of the companion is difficult, and this value is not known for most observed LMXBs. The systems where the donor's spectral type have been measured tend to be the widest LMXBs; Sco X-1, GX 349+2 and Cyg X-2. This additional fourth observed parameter will provide additional constraints to the progenitor mass and period combinations that result in binaries that can match all observed properties.

Sco X-1 was found to have a donor star that was later than K4 (Mata Sánchez et al., 2015). This gives an approximate upper limit to the donor temperature to be  $\lesssim 4800$  K. By matching our three previous properties of interest – period, mass ratio and MT – while constraining the donor temperature, we

can further limit systems that reproduce Sco X-1. An example progenitor of Sco X-1 has a  $1.1M_{\odot}$  donor with an initial period of 2.82 days. This system simultaneously matches the period, mass ratio, MT and effective temperature of Sco X-1. When this progenitor evolves to the observed mass ratio and period, the MT rate and effective temperature of the binary are  $2.3 \times 10^8 M_{\odot} \text{ yr}^{-1}$  and 4685 K respectively.

Cyg X-2 was found by Cowley et al. (1979) to have an A5-F2 donor star. A5-F2 spectral type stars have an approximate temperature range of 7000 - 8500 K. When comparing this to our MT systems, we find that the only progenitors that reproduce Cyg X-2 are binaries with an initial period between  $P \approx 2.24 - 2.51$  days and an initial donor mass of  $M = 3.5M_{\odot}$ . The mass transfer rates and effective temperatures of the 2.24 day progenitor are  $2.9 \times 10^{-8} M_{\odot} \text{ yr}^{-1}$  and 7265 K.

GX 349+2 is a system where the spectral class of the donor is given, but the literature related to this property is not in agreement. Penninx and Augusteijn (1991) found the donor of GX 349+2 to be a G5-M2 giant whereas Wachter and Margon (1996) finds the donor could be a B2 main sequence donor. Our simulated results have a temperature ranging from  $\approx 4800 - 5500$  K which correspond to a K3-G5 donor star. An example progenitor of GX 349+2 is a binary with an initial donor mass of  $M = 1.1M_{\odot}$  and a seed period of 3.98 days. This progenitor has a MT rate of  $8.2 \times 10^{-8} M_{\odot} \text{ yr}^{-1}$  and an effective temperature of 4845 K.

### 3.5 Conclusions

We revised the MB prescription to include the effect of the donor's rotation on the wind's velocity, following Matt et al. (2012) and Réville et al. (2015), as well as the effects of the donor's convective eddy turnover timescale and the donor's rotation on the generation of the surface magnetic field, following

Parker (1971); Noyes et al. (1984); Ivanova (2006); Van et al. (2019).

The new CARB MB prescription was applied to test the evolution of all binaries with a NS and non-degenerate donors that could experience the mass transfer at some point in their evolution. The modelled MT systems were compared to the observed persistent NS LMXBs. Our simulations were required to match with observations in three parameters – the MT rate, the orbital period and the mass ratio, with the effective temperature being used as a fourth parameter in select binaries. Previously, it has been shown that the most commonly used MB prescription, also known as Skumanich MB (Rappaport et al., 1983), is not capable of reproducing most of the persistent NS LMXBs with orbital periods larger than about an hour. With our modified MB, we can reproduce all observed persistent NS LMXBs.

We note that the “Intermediate” prescription considered in Van et al. (2019) reproduced all of the LMXBs of interest as well, although that description was not explicitly derived – it was created by adding ad-hoc wind boosting and ad-hoc convection boosting. Both of these factors are taken into account in a more physical way in the modified MB prescription presented here. Additionally, once the effective temperature is accounted for with the “intermediate” prescription, Sco X-1 could no longer be reproduced. The number of possible progenitors of Cyg X-2 also significantly drops, to only one system.

Our simulations do not include additional effects such as irradiation, or atypically strong magnetic fields similar to those found in Ap stars. While these effects might be invoked to explain a specific individual system, they could not be used to explain the evolution of the entire population of MT binaries. The inclusion of rotational effects on the Alfvèn radius, and magnetic field dependence on convective turnover time, resulted in CARB MB being able to reproduce all of the observed persistent NS LMXBs. We unequivocally recommend the use of the CARB MB prescription instead of the Skumanich MB, to model both Galactic and extragalactic NS LMXBs.

Once the governing angular momentum loss law is constrained, our next step will be to recover and constrain the properties of the plausible progenitor systems, and the required formation rates of these progenitors to produce the observed numbers of LMXBs. We also intend to expand our sample size to include BHs and any additional well constrained NSs available. This will be a topic of our future research.

## Acknowledgements

We would like to thank the referee for helpful comments. N.I. acknowledges that a part of this work was performed at the KITP, which is supported in part by the National Science Foundation under Grant No. NSF PHY-1748958. N.I. acknowledges support from CRC program and funding from NSERC Discovery under Grant No. NSERC RGPIN-2019-04277. K.V. acknowledges the helpful comments from Craig Heinke.

*facility:* Compute Canada

# Chapter 4

## Constraining Progenitors of Observed LMXBs Using CARB Magnetic Braking

Kenny. X. Van<sup>1</sup> and Natalia Ivanova<sup>1</sup>

<sup>1</sup>University of Alberta, Dept. of Physics, 11322-89 Ave, T6G 2E7, Canada;

kvan@ualberta.ca

*Submitted 2021 March 26*

### ABSTRACT

We present a new method for constraining the mass transfer evolution of low mass X-ray binaries (LMXBs) - a reverse population synthesis technique. This is done using the detailed 1D stellar evolution code **MESA** (Modules for Experiments in Stellar Astrophysics) to evolve a high-resolution grid of binary systems spanning a comprehensive range of initial donor masses and orbital periods. We use the recently developed Convection And Rotation Boosted (CARB) magnetic braking scheme. The CARB magnetic braking scheme is the only magnetic braking prescription capable of reproducing an entire sample of well studied persistent LMXBs – those with their mass ratios, periods and mass transfer rates that have been observationally determined. Using the reverse

population synthesis technique, where we follow any simulated system that successfully reproduces an observed LMXB backwards, we have constrained possible progenitors for each observed well-studied persistent LMXB. We also determined that the minimum number of LMXB formations in the Milky Way is 1500 per Gyr if we exclude Cyg X-2. For Cyg X-2, the most likely formation rate is 9000 LMXB per Gyr. The technique we describe can be applied to any observed LMXB with well-constrained mass ratios, period and mass transfer rate. With the upcoming GAIA DR3 containing information on binary systems, this technique can be applied to the data release to search for progenitors of observed persistent LMXBs.

*Unified Astronomy Theory concepts: models (2046)*

## 4.1 Introduction

Low mass X-ray binaries (LMXBs) are binary systems that consist of a star that is overfilling its Roche Lobe – the donor, and of a compact companion, a neutron star (NS) or a black hole (BH) – the accretor. NS LMXBs are among the most studied binary systems in astronomy, with large catalogues dedicated to their observations (e.g., Ritter and Kolb, 2003; Liu et al., 2007). The data presented in these catalogues usually include mass transfer (MT) rates, mass ratios of the two stars, binary orbital periods and, in some cases, the donors' effective temperatures inferred from observations. These properties are essential for theoretical studies of the formation and evolution of LMXBs and are regularly used to compare theoretically obtained systems to the observed ones (Bhattacharya and van den Heuvel, 1991; Podsiadlowski et al., 2002; Van et al., 2019).

There are two very different approaches to gaining insight in the theoretical studies of LMXBs. One approach is to study a specific observed system (Eggleton, 1983; Justham et al., 2006; Pavlovskii and Ivanova, 2016; Podsiadlowski

and Rappaport, 2000; Verbunt and Zwaan, 1981). The other approach is to model a larger population of binaries simultaneously, using assumptions for the initial properties of the initial systems, and their evolution. This approach is known as population synthesis and is commonly used to analyze the statistical properties of a type of system (Fragos et al., 2008; Kalogera and Webbink, 1998; Kobulnicky and Fryer, 2007; Rappaport et al., 2005). Population synthesis codes have been used to calculate formation rates for a wide range of exotic stellar systems using different initial conditions (Belczynski et al., 2018, 2020; Bruzual and Charlot, 2003). In standard population synthesis studies, initial conditions such as the initial mass distribution and the stellar birth rates control the formation and evolution of stellar systems. Depending on the type of systems studied, various other parameters may be adjusted, such as the wind mass-loss rates, accretion luminosity equations, and common envelope prescriptions. The validity of population synthesis is in the accuracy of these initial conditions and parameters or prescriptions used.

In this work, we will be employing a *reverse* population synthesis technique. Instead of applying a set of initial conditions to analyze the obtained systems during and after their evolution, we will use our simulated results to infer the initial progenitor properties.

The theoretically obtained LMXBs will be used to constrain the possible progenitor conditions of our observed systems and estimate the required formation rate of a given progenitor. In Section §4.2 we review the simulation setup – the grid of binaries we used and conditions used to evolve the systems. Section §4.3 presents the viable progenitors of each subgroup of LMXBs. Section §4.4 presents the estimates for the formation rate of the progenitor binaries. In Section §4.5 we take a closer look at the gaps in our parameter space that do not result in any observed LMXBs and discuss why these binaries aren’t seen, and we provide the predictions on where future LMXBs may be detected.

$M_d$ range	$\Delta M_d/M_\odot$	$\log_{10}(P)$ range	$\Delta \log_{10}(P/\text{day})$
0.95 – 4.00	0.05	-0.6 – 1.64	0.02
0.95 – 4.00	0.05	1.65 – 4.0	0.05
4.00 – 7.00	0.10	-0.6 – 1.64	0.02
4.00 – 7.00	0.10	1.65 – 4.0	0.05

Table 4.1: The grid sizes for mass and orbital periods for different ranges of initial donor masses and initial orbital periods.

## 4.2 Model

The detailed numerical setup of how we model a population of LMXBs was described in Van et al. (2019). Below we provide the most crucial points or changes relevant to the presented study.

### 4.2.1 Population Grid

Following Van et al. (2019) and Van and Ivanova (2019), we create an initial grid of NS LMXBs with a range of initial periods and masses while using a higher-resolution grid as compared to the previous studies. The parameters of the mesh are:

- Initial donor masses are in the range  $0.95 \leq M_d/M_\odot \leq 7.00$ .
- Initial binary period are in the range  $-0.6 \leq \log_{10}(P/\text{day}) \leq 4.0$ .

We use a non-uniform mesh density for the initial donor mass and period, see Table 4.1 for the distribution. With the adopted mesh density, we model a total of 14836 binary systems.

All donors are placed in binary systems with a NS accretor that has an initial mass of  $M_a = 1.4M_\odot$  and radius  $R_a = 11.5$  km. A binary system at any point in its evolution can also be characterized by the derived quantity  $q = M_d/M_a$ , which is the mass ratio between the donor and accretor. All donors are initially at their zero-age main sequence. For all simulations, we adopt metallicity  $Z = 0.02$ .

The simulations were performed using the one-dimensional stellar evolution code **MESA**<sup>1</sup> (Modules for Experiments in Stellar Astrophysics) revision 11701 (Paxton et al., 2011, 2013, 2015, 2018, 2019), and May 2019 release of **MESASDK** (Townsend, 2019). The wind mass loss scheme used in our donor star is the “Reimers” wind mass prescription (Reimers, 1975) with no additional boosting factors included. We also allow for the evolution of the radial velocity in our donor star.

For our binary parameters, we use a modified Eddington limit appropriate for NSs and an improved magnetic braking prescription. Both the magnetic braking prescription and the modified Eddington limit will be described in further detail in Sections 4.2.2 and 4.2.3 respectively. Beyond these changes in our simulation parameters, the other properties are done using **MESA** defaults.

The MESA EOS is a blend of the OPAL (Rogers and Nayfonov, 2002), SCVH (Saumon et al., 1995), PTEH (Pols et al., 1995), HELM (Timmes and Swesty, 2000), and PC (Potekhin and Chabrier, 2010) EOSs.

Radiative opacities are primarily from OPAL (Iglesias and Rogers, 1993, 1996), with low-temperature data from Ferguson et al. (2005) and the high-temperature, Compton-scattering dominated regime by Buchler and Yueh (1976). Electron conduction opacities are from Cassisi et al. (2007).

Nuclear reaction rates are a combination of rates from NACRE (Angulo et al., 1999), JINA REACLIB (Cyburt et al., 2010), plus additional tabulated weak reaction rates (Fuller et al., 1985; Oda et al., 1994; Langanke and Martínez-Pinedo, 2000). Screening is included via the prescriptions of Salpeter (1954); DeWitt et al. (1973); Alastuey and Jancovici (1978) and Itoh et al. (1979). Thermal neutrino loss rates are from Itoh et al. (1996).

The orbital evolution of the binary systems is governed by the total angular momentum loss through three main mechanisms. These mechanisms include angular momentum loss due to magnetic braking (see §4.2.2), through angular

---

<sup>1</sup><http://mesa.sourceforge.net>

momentum loss via mass loss from the system (see §4.2.3), and in very short period systems, angular momentum loss due to gravitational radiation (Faulkner, 1971). Our simulations do not account for any additional effects the compact object may have on the donor star, such as irradiation or tidal heating.

When the donor star overfills its Roche lobe (for a one-dimensional approximation of the Roche lobe radius, see Eggleton, 1983), the material will flow from the donor to the accretor through the  $L_1$  Lagrange point between the two stars. The rate of mass transfer (MT) is calculated using the "Ritter" prescription in **MESA** (for more information on the MT prescription, see Ritter, 1988). The details on the accretion rate and the Eddington limit will be described in section §4.2.3.

The simulated LMXBs all start with an NS already formed and the donor star at zero-age main sequence (ZAMS). All simulations continued for 10 Gyrs, or until the donor star detaches and no longer transfers mass to the NS. In some cases, the simulation would experience dynamically unstable mass transfer which **MESA** is not designed to simulate. These simulations would likely encounter numerical issues and stop. Some of the systems were initially placed at such a short period that they overfill, sometimes significantly, their Roche lobe at the start of simulations while surviving this initial MT. We did not discard these systems but discuss them separately with caution.

### 4.2.2 Magnetic Braking

We use the Convection and Rotation Boosted (CARB) magnetic braking (see Van and Ivanova, 2019, for the derivation). The angular momentum loss from a star with radius  $R$ , rotating with a rate of  $\omega$  at its surface, is:

$$\dot{J}_{\text{MB}} = -\frac{2}{3} \dot{M}_{\text{W}}^{1/3} R^{14/3} \left( v_{\text{esc}}^2 + \frac{2\Omega^2 R^2}{K_2^2} \right)^{-2/3} \times \Omega_{\odot} B_{\odot}^{8/3} \left( \frac{\Omega}{\Omega_{\odot}} \right)^{11/3} \left( \frac{\tau_{\text{conv}}}{\tau_{\odot, \text{conv}}} \right)^{8/3}. \quad (4.1)$$

$\dot{M}_{\text{W}}$  denotes the wind mass loss rate,  $v_{\text{esc}}$  is the surface escape velocity,  $\tau_{\text{conv}}$  is the convective turnover time,  $B$  is the surface magnetic field strength, and  $K_2 = 0.07$  in this equation is a constant obtained from a grid of simulations by Réville et al. (2015).  $K_2$  sets the limit to the rotation rate required to play a significant role in damping the magnetic braking. The solar values adopted to normalize Equation 4.1 are  $B_{\odot} = 1$  G for Sun's surface magnetic field strength, and  $\Omega_{\odot} \approx 3 \times 10^{-6}$  s<sup>-1</sup> for Sun's surface rotation rate. For convective turnover time we use  $\tau_{\odot, \text{conv}} = 2.8 \times 10^6$  s. This value was obtained by evolving a  $1M_{\odot}$ ,  $Z = Z_{\odot}$  star to 4.6 Gyrs and using the following equation:

$$\tau_{\text{conv}} = \int_R^{R_s} \frac{dr}{v_{\text{conv}}}. \quad (4.2)$$

$R$  and  $R_s$  are the bottom and the top of the outer convective zone respectively, while  $v_{\text{conv}}$  is the local convective velocity (for more details, see Van et al., 2019).

### 4.2.3 Accretion rate

Following Van et al. (2019) and Van and Ivanova (2019), we consider non-conservative MT, where we limit the mass accretion rate by the Eddington-limited maximum accretion rate. If the MT rate exceeds the Eddington limit, the excess is not considered to be accreted by the compact object but is counted as lost from the system with the accretor's specific angular momentum. The Eddington-limited mass accretion rate  $\dot{M}_{\text{Edd}}$  is:

$$\dot{M}_{\text{Edd}} = \frac{4\pi c R_a}{\kappa_e} \approx \frac{3.4}{1+X} \times 10^{-8} M_{\odot} \text{ yr}^{-1} \quad (4.3)$$

Here,  $\kappa_e$  is the Thomson electron scattering opacity,  $\kappa_e = 0.19(X + 1) \text{ cm}^2 \text{ g}^{-1}$ ,  $X$  is the hydrogen mass fraction in the material transferred from the donor.

In addition to the Eddington limit, we also impose MT efficiency  $\eta$  which represents a mass transfer efficiency. An analytic description of  $\eta$  is not currently known, but previous work has shown that this efficiency can range between  $\sim 0.05 - 0.3$  in pulsars. Previously, Van and Ivanova (2019) showed that an efficiency  $\eta = 1$  would result in neutron star masses consistently exceeding  $2M_{\odot}$  and an efficiency of  $\eta = 0.2$  results in a more reasonable upper mass value of  $\sim 1.8M_{\odot}$  (for an explanation see Van and Ivanova, 2019). Combining the Eddington limit and the mass transfer efficiency, the material accreted by the NS is

$$\dot{M}_{\text{NS}} = \min(\dot{M}_{\text{Edd}}, \eta \dot{M}_{\text{tr}}) \quad (4.4)$$

$\dot{M}_{\text{tr}}$  is the mass lost by the donor via its  $L_1$  Lagrange point due to Roche lobe overflow. The amount of material accreted onto the NS determines the observed luminosity of the system. It is important to note material accreted onto the disc that moves closer to the compact object but is not accreted onto the compact object itself will also contribute to the luminosity of the system. Along with MT efficiency  $\eta$  not being constant throughout the evolution, we estimate that the luminosity of our systems can be described by the equation:

$$L = \frac{0.6GM_{\text{tr}}\dot{M}_{\text{NS}}}{R_{\text{NS}}} \quad (4.5)$$

To account for these uncertainties, the sizes of our MT bins are large enough to compensate during analysis.

#### 4.2.4 Persistent Systems

To compare the simulated systems to the observed systems, we must determine if the simulated system is observable. Specifically, we only compare to the systems which are observationally classified as persistent LMXBs. To discriminate whether the modelled system would be deemed persistent or transient from observations, we use the disc instability model (DIM). The DIM states that there exists a critical mass transfer rate that separates persistent and transient systems at a given period (Meyer and Meyer-Hofmeister, 1981). In systems where the accretion is too low, the created accretion disc experiences a buildup of material. The system will then experience outbursts separated by the periods of quiescence caused by increases and decreases in temperature, and thus appears as a transient system. Conversely, if the accretion rate is high for this orbital period, the accretion disc is in a constantly bright state, appearing persistent (see Lasota, 2001, for a review of DIM). In this paper, we use the stability criteria from Coriat et al. (2012):

$$\dot{M}_{\text{crit}} = k P_{\text{hr}}^b \quad (4.6)$$

$P_{\text{hr}}$  is the orbital period of the binary system in hours. The most lenient classification that predicts the largest number of persistent systems requires an irradiated disc with a neutron star accretor. The condition for an irradiated disk instability results in the lowest  $\dot{M}_{\text{crit}}$  for any given orbital period. The condition of instability for an irradiated accretion disk is described by Equation 4.6 with  $b = 1.59$  and  $k = 2.0 \times 10^{15} \text{ g s}^{-1}$ . Any MT system that exceeds this critical transfer rate is classified in our simulations as a persistent LMXB. This MT rate is the amount of mass accreted onto the disk and is related to  $\dot{M}_{\text{RLOF}}$ , the material flowing through the  $L_1$  point.

#### 4.2.5 Relating the observed LMXBs to the simulated LMXBs

For our analysis, we split the sample of observed binaries based on the orbital period (see Table 4.2). Ultra-compact X-ray binaries (UCXBs) are LMXBs defined to have an orbital period of shorter than 80 minutes. Systems with periods less than 4 hours are often classified as short period LMXBs. Our sample only contains one binary with a period of about ten days, Cyg X-2, which we define as a long period binary. LMXBs with orbital periods ranging from tens of hours to approximately one day, which we name as *medium period* for the analysis in this paper.

To determine the progenitors of the observed LMXBs of interest, we must simultaneously match the orbital period, the MT rate, and the mass ratio of our simulated system with one of the observed systems. We consider that each observed, persistent LMXB is not a single point in this three-dimensional space, but can be represented by a cuboid. Each cuboid is centred at one of the observed LMXBs. The lengths of the cuboid edges are taken to be equal to the uncertainties in each of the observed quantities for this observed LMXB. In the case of the mass ratio and mass transfer rates, these are the observed errors in each quantity while the length of  $\log_{10}(P)$  represents a reasonable range for the value. See Table 4.2 for details on the adopted cuboids in the period, mass ratio, and MT rate space. These centres of each cuboid and the errors in each dimension are taken from Van and Ivanova (2019).

For LMXBs with additional observed properties, we can further constrain the number of possible progenitors. In the case of Sco X-1 and Cyg X-2, there are observation values for the effective temperatures of the donor star. Observations by Mata Sánchez et al. (2015) found that the donor star in Sco X-1 was later than a K4. This observation constrains the donor star's effective temperature to have an upper limit of  $T_{\text{eff}} \lesssim 4800$  K. Cyg X-2, on the other

System Name	$\log_{10}(P/\text{day})$	$q$	$\log_{10}(\dot{M}_{\text{tr}})$	$\tau_{\text{max}}$ (years)	$A_{\text{sys}}/A_{\text{tot}}$
UCXB					
4U 0513-40	[-1.95, -1.90]	[0.01, 0.06]	[-9.0, -8.4]	$1.08 \times 10^7$	$1.37 \times 10^{-3}$
2S 0918-549	[-1.94, -1.89]	[0.01, 0.06]	[-9.6, -8.4]	$1.12 \times 10^7$	$1.41 \times 10^{-3}$
4U 1543-624	[-1.92, -1.87]	[0.01, 0.06]	[-8.9, -8.4]	$1.44 \times 10^7$	$1.44 \times 10^{-3}$
4U 1850-087	[-1.86, -1.81]	[0.01, 0.06]	[-9.8, -8.2]	$2.34 \times 10^7$	$1.69 \times 10^{-3}$
M15 X-2	[-1.82, -1.77]	[0.01, 0.06]	[-9.5, -8.9]	$3.22 \times 10^7$	$1.76 \times 10^{-3}$
4U 1626-67	[-1.55, -1.50]	[0.01, 0.06]	[-9.5, -8.4]	$9.33 \times 10^7$	$2.25 \times 10^{-3}$
4U 1916-053	[-1.48, -1.43]	[0.03, 0.08]	[-9.4, -8.7]	$5.82 \times 10^7$	$7.40 \times 10^{-4}$
Short period					
4U 1636-536	[-0.82, -0.77]	[0.15, 0.40]	[-8.9, -8.4]	$2.53 \times 10^7$	$4.05 \times 10^{-3}$
GX 9+9	[-0.78, -0.73]	[0.20, 0.33]	[-8.5, -8.0]	$1.66 \times 10^7$	$3.91 \times 10^{-3}$
4U 1735-444	[-0.73, -0.68]	[0.29, 0.48]	[-8.2, -7.7]	$1.07 \times 10^7$	$4.23 \times 10^{-3}$
2A 1822-371	[-0.65, -0.60]	[0.26, 0.36]	[-7.6, -7.1]	$6.15 \times 10^6$	$5.32 \times 10^{-3}$
Medium period					
Scorpius X-1	[-0.12, -0.07]	[0.15, 0.58]	[-7.8, -7.1]	$9.42 \times 10^6$	$1.66 \times 10^{-3}$
GX 349+2	[-0.05, 0.00]	[0.39, 0.65]	[-7.8, -7.1]	$1.58 \times 10^7$	$4.37 \times 10^{-3}$
Long period					
Cyg X-2	[0.97, 1.02]	[0.25, 0.53]	[-7.8, -7.0]	$8.36 \times 10^5$	$2.30 \times 10^{-3}$

Table 4.2: The binned properties of the observed LMXBs used to compare to simulated systems and diagnostic properties used to analyze the results. The binned properties are period in days, mass transfer rate in  $\dot{M}_{\text{tr}}$  is in  $M_{\odot} \text{ yr}^{-1}$  and the mass ratio. The bin ranges are centred on the observed values and span the errors in the given observed property. The two diagnostic properties are the maximum amount of time a given simulated system spends in the observed bin of interest,  $\tau_{\text{max}}$  and  $A_{\text{sys}}/A_{\text{tot}}$  is the fraction of our tested parameter space that can reproduce the system of interest. These two quantities indicate how long a simulation appears similar to an observed LMXB and how many systems could reproduce these properties. The period, mass ratio and mass transfer rate bins are taken from Table 4 from Van et al. (2019).

hand, is better constrained as the observations by Cowley et al. (1979), which limit the effective temperature to  $7000 \lesssim T_{\text{eff}}/\text{K} \lesssim 8500$ . With these additional observed quantities, we can compare the effective temperature of our simulated systems to these observed constraints to limit the viable progenitors.

#### 4.2.6 Progenitor search

To analyze the progenitor population, we start with finding the total observed time  $\tau_{\text{observed}}$ , which is defined as the total amount of time that a seed progenitor

binary spends while appearing similar to any of the observed binaries, e.g., it passes through any of the cuboids. We then find the amount of time a simulated binary spends as a persistent binary predicted by Equation 4.6,  $\tau_{\text{persistent}}$ . Their ratio is:

$$f_{\text{obs}} = \frac{\text{Time matching observed system}}{\text{Time satisfying persistent condition}} = \frac{\tau_{\text{observed}}}{\tau_{\text{persistent}}}, \quad (4.7)$$

The amount of time our simulations spend as a persistent system exceeds the amount of time it appears similar to any of the observed binaries. This ratio gives us an idea of how likely a progenitor can produce an observed system. If a progenitor has a very high ratio, this means that the system spends a significant fraction of its persistent lifetime appearing similar to an observable LMXB. We will also define an additional parameter  $f_{\text{obs},i}$ :

$$f_{\text{obs},i} = \frac{\text{Time matching a specific observed system}}{\text{Time satisfying persistent condition}} \quad (4.8)$$

Using this definition  $f_{\text{obs},i} \leq f_{\text{obs}}$ . We will use  $f_{\text{obs},i}$  in figures where we will be looking at progenitors of a single observed LMXB and  $f_{\text{obs}}$  for figures where we determine the progenitor of multiple LMXBs.

### 4.3 Analysis

We present the progenitors of the observed systems in Figure 4.1. While the initial parameter space spans a significant range in mass and period, the viable progenitors are constrained to a small area of the parameter space. Specifically, only the binary systems with the initial donor masses between  $0.95M_{\odot}$  and  $4.5M_{\odot}$  and with the orbital periods between 0.4 days and 16 days have been found to contribute to any of the existing persistent LMXBs. The progenitors of the individual types of LMXBs form distinct groups. Below, we will examine each of them in detail.

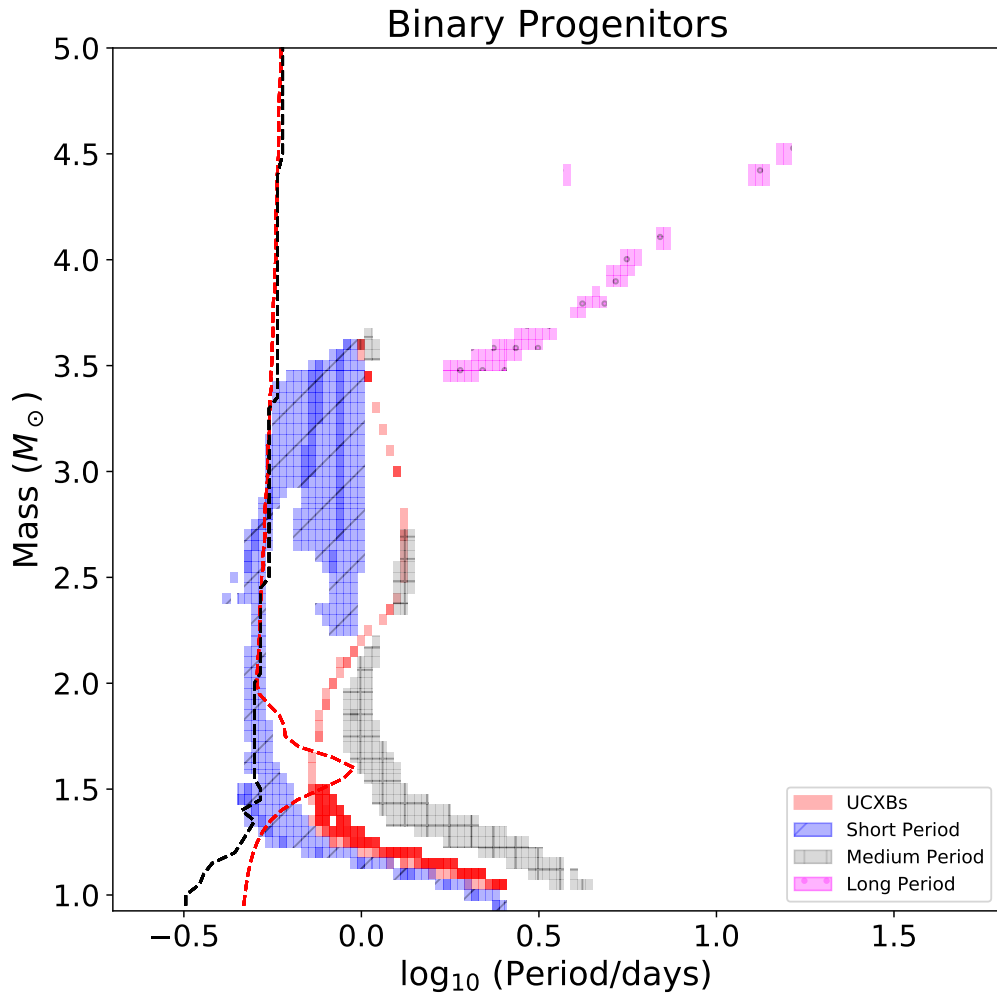


Figure 4.1: The progenitors of the observed LMXBs split into distinct classes based on the periods of the currently observed systems as denoted in Table 4.2. Some observed systems share common progenitors, to show this, the individual grid points are semitransparent. The black dashed line denotes the shortest initial period with which the initial binary would start as a detached system. The red dashed line denotes the shortest initial period which the detached binary can have when the progenitor is 10 million years old. The systems on the left of the black dashed line started their evolution while having an initial Roche lobe overflow.

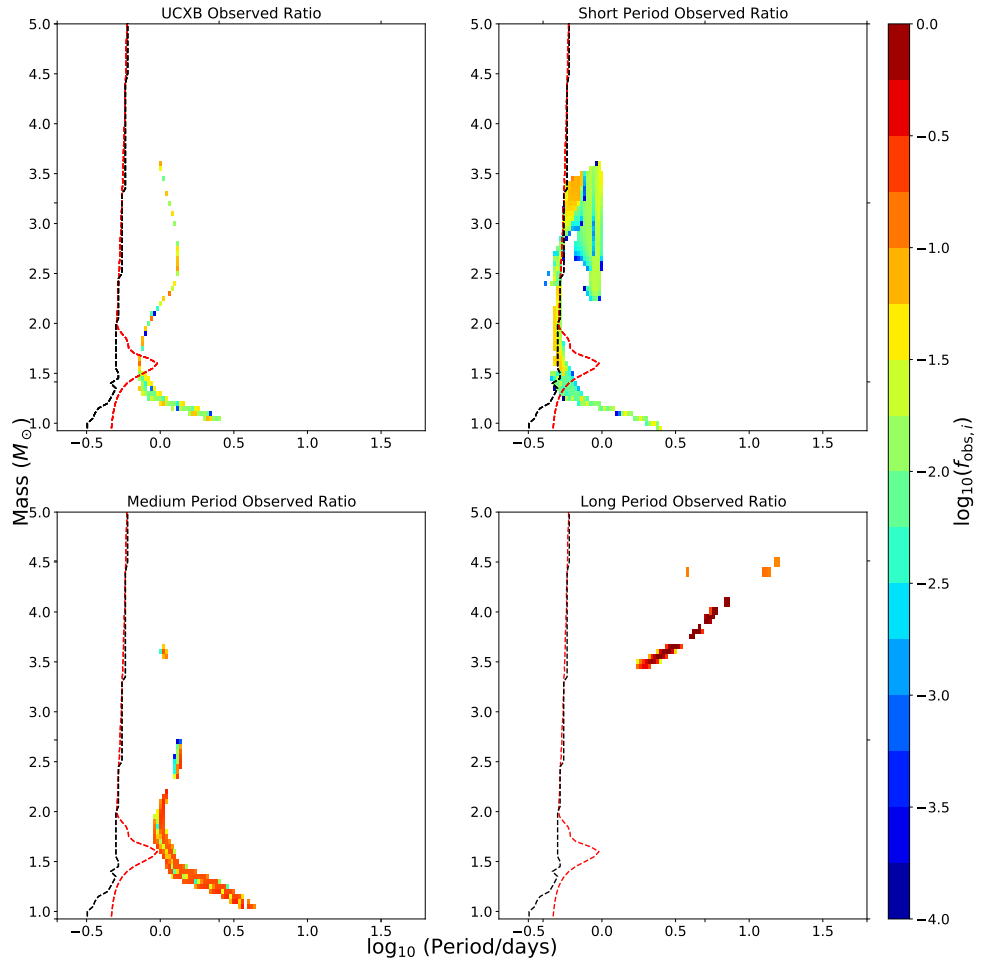


Figure 4.2: The progenitors of the four types of the observed LMXB. The colour shows  $f_{\text{obs},i}$ , the fraction of time the modelled system shows up as one of the observed LMXB, as compared to the time it can be observed as any persistent LMXB, see Equation 4.7). The black and the red dashed lines are as in Figure 4.1.

We anticipate that in a field binary, an NS formation is unlikely to take place at the same time when the companion is at its ZAMS. Some companions have already evolved from their MS, while others are still in the pre-main sequence stage. For that reason, we also analyze the constraints on the progenitor space due to the minimum period which a binary could have when the progenitor-donor is 10 million years old (an NS could have been created between 7 and 25 million years after the two stars started their formation, depending on the initial mass of the initially more massive star). Specifically, at the age of 10 million years, only stars more massive than  $2M_{\odot}$  have reached the ZAMS (see Figure 4.1). At the same time, pre-MS stars with about  $1.6M_{\odot}$  separate the stars with radiative and convective outer zones, resulting in a bump in the plausible initial periods.

### 4.3.1 Ultra Compact Systems

By splitting our sample of observed binaries into the period ranges given in Table 4.2, we can determine if there are specific ranges in our parameter space that reproduce a subset of the observed systems. The progenitors which reproduce the observed UCXBs are shown in Figure 4.2.

In LMXB evolution, for each donor and accretor combination, there is a critical value of the initial orbital period known as the bifurcation period. The bifurcation period separates the binaries where mass transfer leads to shrinking orbital separations and those where the orbital period increases, at least until the donor detaches and MT no longer occurs. The progenitors of UCXBs in the field accordingly are considered to have the initial periods below the bifurcation period for their companions (Nelson et al., 1986; Nelson and Rappaport, 2003; Podsiadlowski et al., 2002). The bifurcation periods' values are also a function of the accepted magnetic braking. Our results for UCXBs progenitors are in complete agreement with their standard formation scenario.

The entire group of UCXBs progenitors comes from a very narrow portion

of the parameter space with very few viable initial periods for a given initial donor mass. The initial period has the largest possible range for donors with lower masses, spanning up to  $\log_{10}(P/\text{days}) \approx 0.2$ . As the mass increases, this period range decreases to  $\log_{10}(P/\text{days}) \approx 0.02$ . From the maximum amount of time spent in an observed bin listed in Table 4.2, we see that the modelled systems spend a significant amount of time appearing similar to the observed UXCBs. Having a large  $f_{\text{obs}}$  is expected, as these binaries are highly evolved systems near the end of the donor stars' life, and the evolution of UCXBs slows down almost exponentially with time.

The two UCXBs, 4U 1626-67 and 4U 1916-053 have longer detected periods than the other five ultra-compact systems. These two systems have been found to require more complex stellar evolution, such as enhanced angular momentum loss at shorter periods, an evolved main sequence donor with finely tuned initial parameters for either magnetic braking, or common envelope evolution (Heinke et al., 2013; Podsiadlowski et al., 2002). Our progenitors that successfully reproduce 4U 1626-67 and 4U 1916-053 are all main sequence stars that have not evolved enough to produce a significant amount of helium in their cores. Our formation channel is an alternative evolutionary channel, where the updated magnetic braking results in the donor star having a sufficiently short period such that gravitational radiation drives high enough MT prior to MT stopping. In our simulations, reproducing these two UCXBs also requires fine-tuning in the sense that the initial progenitor space is very small, and only donors more massive than  $1.50M_{\odot}$  have contributed.

### 4.3.2 Short Period

The progenitors of the short period systems span a much larger period and mass range than the ultra-compact systems, with a larger fraction of the progenitor space resulting in an observed binary (see Figure 4.2). Initial donor masses that form our short period systems range from  $0.9M_{\odot}$  to  $3.6M_{\odot}$ , with the periods

between 0.45 day and 2.5 days ( $-0.34 \leq \log_{10}(P/\text{days}) \leq 0.40$ ). Unlike the UCXB systems, there is no clear pattern or structure in the initial parameter space needed to reproduce all of the observed short LMXBs. Plotting the progenitors for each observed short LMXB system individually demonstrates their distinct differences (see Figure 4.3).

The progenitors of 4U 1636-536 and GX 9+9 appear to belong to very confined progenitor groups. The masses are confined to  $2.25 \leq M/M_\odot \leq 3.60$  and  $2.55 \leq M/M_\odot \leq 3.60$ , respectively, and the initial periods spans are  $-0.12 \leq \log_{10}(P/\text{days}) \leq 0$  and  $-0.18 \leq \log_{10}(P/\text{days}) \leq -0.04$ , respectively. These two LMXBs, 4U 1636-53 and GX 9+9, share progenitors with initial masses ranging from  $2.70 \leq M/M_\odot \leq 3.55$  and  $\log_{10}(P/\text{days}) = -0.06$ .

The progenitors of 4U 1735-444 are split into two distinct groups based on the mass, with the higher mass group ranging from  $2.50 \lesssim M/M_\odot \leq 3.50$  and the lower mass group spanning  $0.95 \leq M/M_\odot \leq 1.50$ . The overall period range of these progenitors span  $-0.38 \leq \log_{10}(P/\text{days}) \leq 0.38$ . For more massive progenitor systems, the fraction of systems appearing similar to 4U 1735-444 is higher, but the time they spend in this state ranges from  $10^4$  years to  $10^8$  years. The lower mass progenitors have a smaller range between  $10^4$  and  $10^6$  years.

The progenitor binaries of 2A 1822-371 are very similar to the progenitors of 4U 1735-444 and form the group that is adjoined to the progenitors of 4U 1735-444 at similar initial orbital periods. Their masses range  $0.95 \leq M/M_\odot \leq 2.90$  and the periods range  $-0.34 \leq \log_{10}(P/\text{days}) \leq 0.40$ . For both 4U 1735-444 and 2A 1822-371 (but especially for the latter one), many progenitors may not exist in nature: the donors either experience RLOF at ZAMS or when the NS was formed (see Figure 4.3). Observationally determining the effective temperature of the donors could greatly constrain the possible progenitors, as the higher mass donors group have higher temperatures at  $T_{\text{eff}} \sim 5000K$  than the low mass donors with  $T_{\text{eff}} \sim 3900K$ .

A key attribute that can be seen in Figure 4.3 is the smooth transition from one observed LMXB’s progenitors to another with overlap between systems. The higher mass progenitors with  $M \approx 2.5M_{\odot}$  can, depending on the period of the binary system, produce all four of our short period LMXBs. At this initial donor mass 4U 1735-44 can be reproduced with an initial separation of  $\log_{10}(P/\text{days}) = -0.36$ . As the initial period increases to  $-0.32 \leq \log_{10}(P/\text{days}) \leq -0.28$ , we effectively reproduce 2A 1822-37.

### 4.3.3 Medium Period

The progenitors of medium period LMXBs form a narrow strip in the initial period for each initial mass that spans over a large region of the periods (see Figure 4.2). Separating the progenitors of the two observed medium period LMXBs in Figure 4.4, we see that Sco X-1 has the continuous range of possible progenitor masses, up to about  $2 M_{\odot}$ , whereas GX 349+2 can have more massive progenitors, but not continuous in all masses above  $2 M_{\odot}$ . The progenitors of Sco X-1 span nearly the same mass range as the low mass portion of GX 349+2 at slightly shorter, while almost adjacent, periods. Specifically, the Sco X-1 progenitors have initial mass and period ranges of  $1.05 \leq M/M_{\odot} \leq 1.95$  and  $-0.04 \leq \log_{10}(P/\text{days}) \leq 0.56$ . The low mass progenitors of GX 349+2 have similar masses,  $1.05 \leq M/M_{\odot} \leq 2.20$ . GX 349+2 has two gaps in the progenitor parameter space, one at  $2.25 \leq M/M_{\odot} \leq 2.30$  and another between  $2.75 \leq M/M_{\odot} \leq 3.55$ . The lower mass gap is due to these systems not reaching the observed period, instead, these progenitors converge to an ultra-compact separation. The gap between  $2.70 M_{\odot}$  and  $3.55 M_{\odot}$  is due to the simulated binary not reaching sufficiently high mass transfer rates.

We anticipate that Sco X-1 is more limited in our parameter space than GX 349+2 as we used the additional constraint on the donor’s effective temperature. Without the effective temperature constraint, the mass range for Sco X-1 progenitors extends up to  $2.55 M_{\odot}$ , while with the effective temperature

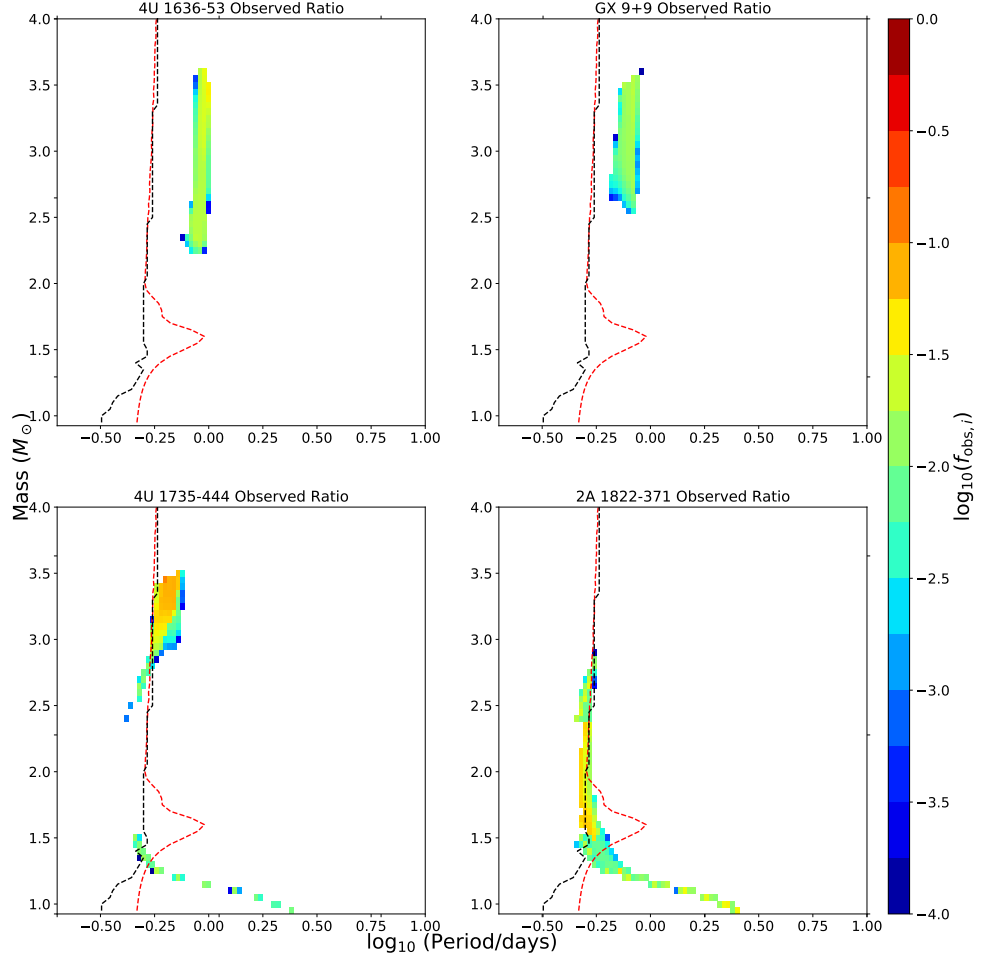


Figure 4.3: The short period systems from Figure 4.2 split into the individual systems. The colour shows  $f_{\text{obs}}$ , the fraction of time the modelled system shows up as one of the observed LMXB, as compared to the time it can be observed as any persistent LMXB. The black and the red dashed lines are as in Figure 4.1.

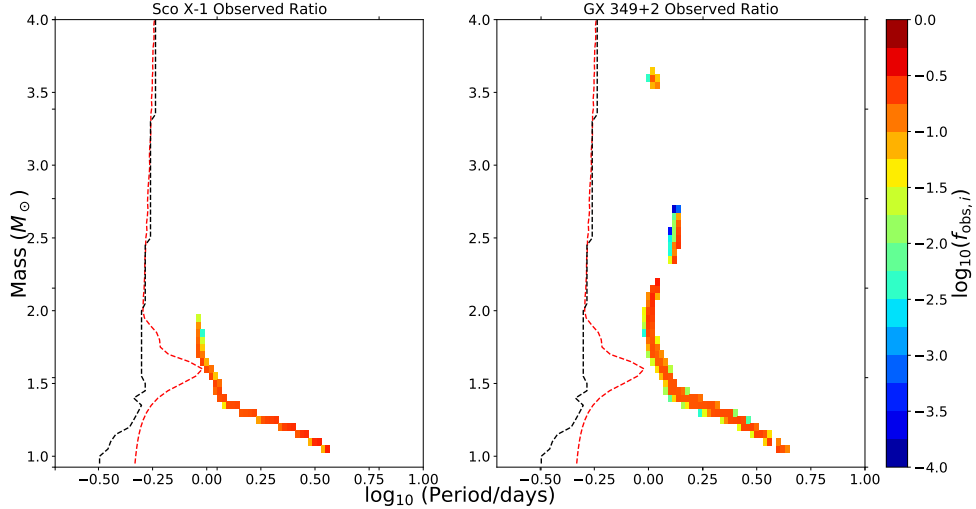


Figure 4.4: The ratio between observed and persistent times of the two medium period LMXBs. Similar to Figure 4.1, the black and red dashed lines show the shortest period where an initial binary would start as a detached system and the shortest initial period which the detached binary can have when the progenitor is 10 million years old respectively.

constraint, the upper mass limit remains at  $2.0M_{\odot}$ . We discuss effective temperature more in section 4.3.5. If the effective temperature would be measured for the donor in GX 349+2, the mass of its progenitors could be constrained more, and either high mass or low mass formation channel could be ruled out.

The progenitors of GX 349+2 with the initial masses  $2.35 \leq M/M_{\odot} \leq 2.70$  and the period of  $\log_{10}(P/\text{days}) = 0.12$  overlap with the progenitors of the UCXB 4U 1626-67, implying that GX 349+2 may evolve to a UCXB system. This small parameter space is the only initial parameter space with progenitors resulting in two LMXB systems with drastically different parameters.

#### 4.3.4 Long Period

Cygnus X-2 is the only system in the long period category of our observed LMXBs. It is also one of the LMXBs with the observed effective temperature. This binary system stands out as there is a significant jump in the period from GX 349+2 to Cyg X-2. The progenitor parameter space area that can

produce Cyg X-2 is comparable to the other observed systems (see Figure 4.2). However, the maximum amount of time a simulated system spends in the appropriate bin (been similar to the observed LMXB) is much shorter. Specifically, the longest living binary spends less than  $10^6$  years in the bin. The progenitor's initial space has less of a clear pattern, unlike the LMXBs we discussed previously. While that space form almost a strip, with the initial period increasing as the initial donor mass increases, there are gaps in the masses for plausible progenitors. The gaps in our progenitor space with initial masses below  $M = 4.0M_{\odot}$  do not reach sufficiently high mass transfer rates whereas the systems with  $M \geq 4.0M_{\odot}$  have mass transfer rates that exceed  $10^{-7}M_{\odot}\text{yr}^{-1}$  when at the appropriate mass ratio and period values. There is also an outlier at  $M = 4.4M_{\odot}$  and  $\log_{10}(P/\text{days}) = 0.58$ . It has been previously proposed that Cyg X-2 requires an intermediate-mass donor star (Podsiadlowski and Rappaport, 2000), and our results fully confirm that only this formation scenario can work.

#### 4.3.5 Effective Temperature

For Sco X-1 and Cyg X-2, we have an additional fourth physical parameter, the effective temperature, to limit the number of possible progenitors. Sco X-1 was found to have a donor star that has a spectral class later than K4 giving an approximate upper limit of  $T_{\text{eff}} \lesssim 4800$  K (Mata Sánchez et al., 2015). Cyg X-2, on the other hand, ranges between an A5 to F2 spectral type, giving it a temperature range of 7000 – 8500 K (Cowley et al., 1979). The inclusion of effective temperature as an additional constrain has significant effects on the possible progenitor systems, as can be seen in Figure 4.5.

In Sco X-1, the inclusion of effective temperature limits the overall progenitor mass to be below  $M_i \lesssim 2.0M_{\odot}$ , and narrows the width in the possible initial periods at a given mass. As Sco X-1 is only constrained by an upper limit, the progenitors that are excluded due to the effective temperature are

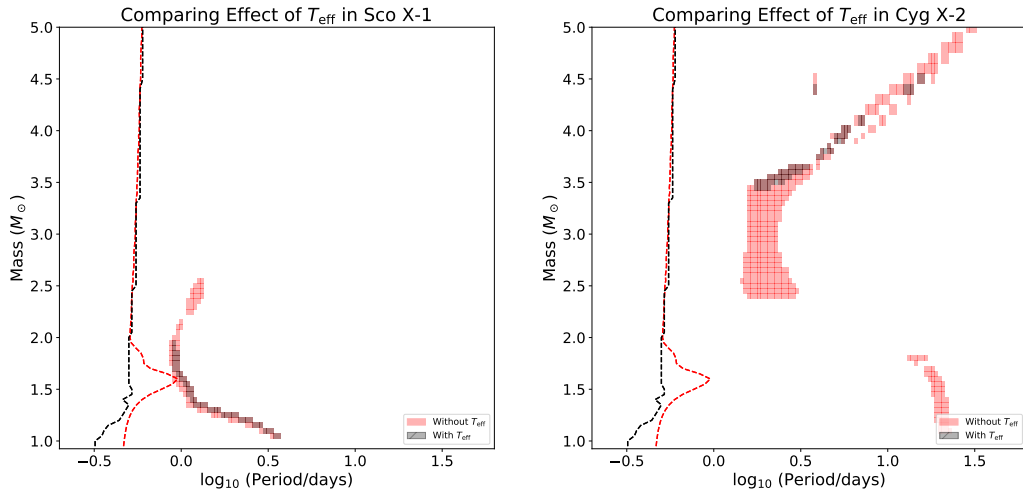


Figure 4.5: The progenitors of Sco X-1 and Cyg X-2 when the effective temperature is excluded in black and included in red. The black and red dashed lines are identical to those in Figure 4.1.

systems where the temperature exceeds the upper limit found by Mata Sánchez et al. (2015). The effective temperature plays a significantly larger role in limiting the progenitors of Cyg X-2 as seen in Figure 4.5. Without the effective temperature, the number of viable progenitors for Cyg X-2 drastically increases and the viable initial masses can span the entire parameter space. Due to the defined range in  $T_{\text{eff}}$  for Cyg X-2, the excluded progenitors can have a wide range of possible values. The cluster of progenitors at  $\log_{10}(P/\text{days}) \approx 1.3$  at lower masses results in LMXBs that appear similar to Cyg X-2 but the donor stars of these systems have significantly lower effective temperatures at  $T_{\text{eff}} \approx 4500K$ . The progenitors below  $M_i \leq 3.5M_{\odot}$  also do not reach sufficiently high temperatures with  $T_{\text{eff}}$  decreasing with progenitor mass. The progenitors with initial masses exceeding  $M_i \geq 4.0M_{\odot}$  on the other hand, consistently exceed the observed temperature with values of  $T_{\text{eff}} \geq 9000$  K. The effective temperature of Cyg X-2 is a very restrictive property that requires fine-tuning the initial parameters to match the observed value.

System Name	$\log_{10}(\dot{M}_a)$
4U 1636-536	[-9.50, -7.50]
GX 9+9	[-9.25, -7.50]
4U 1735-444	[-8.95, -7.50]
2A 1822-371	[-8.35, -7.00]
Sco X-1	[-8.45, -7.00]
GX 349+2	[-8.45, -7.00]
Cyg X-2	[-8.40, -6.90]

Table 4.3: This table shows the extended mass transfer rate bins we use to determine the effect of our bin choices. The mass transfer rate is in units of  $M_\odot \text{ yr}^{-1}$ . The lower bound of our mass transfer rate is set to either  $-9.5$  or  $10\%$  the observed value, whichever is higher. The upper limit is then set to  $-7.5$  or  $0.5$  dex above the observed value. The asymmetry in the limits is due to the Eddington limit which we do not expect most of these systems to exceed.

### 4.3.6 Wider Bins

To determine the effect of the uncertainties in observed properties, we extend the size of our observed bins to encompass more significant errors. In particular, we focus on testing the period values for UCXBs and probe how varying the mass transfer rate changes our results. For UCXBs, we combine our bins to be  $-2 \lesssim \log_{10}(P/\text{day}) \lesssim -1.4$ ,  $0.01 \lesssim q \lesssim 0.08$ , and  $-12 \lesssim \log_{10}(\dot{M}_a) \lesssim -7.5$ . For our non-UCXB systems, we only vary the anticipated mass transfer rates. The extended values are given in Table 4.3.

The progenitors that can create the LMXBs within the extended bins are shown in Figure 4.6. The most significant changes, as compared to our standard bins, can be seen in the progenitors of UCXBs and the short period systems. There is little change in the medium and no changes to the long period progenitors. In the case of UCXBs, previous studies and our narrower bins predict that UCXBs could only be produced by systems with initial periods near the bifurcation period (Podsiadlowski et al., 2002). Using the wider bins, the possible progenitors extend well beyond the area near the bifurcation period and have significant overlap with short period progenitors.

Examining the evolution of the models with high initial masses  $M \geq 2.0M_\odot$ ,

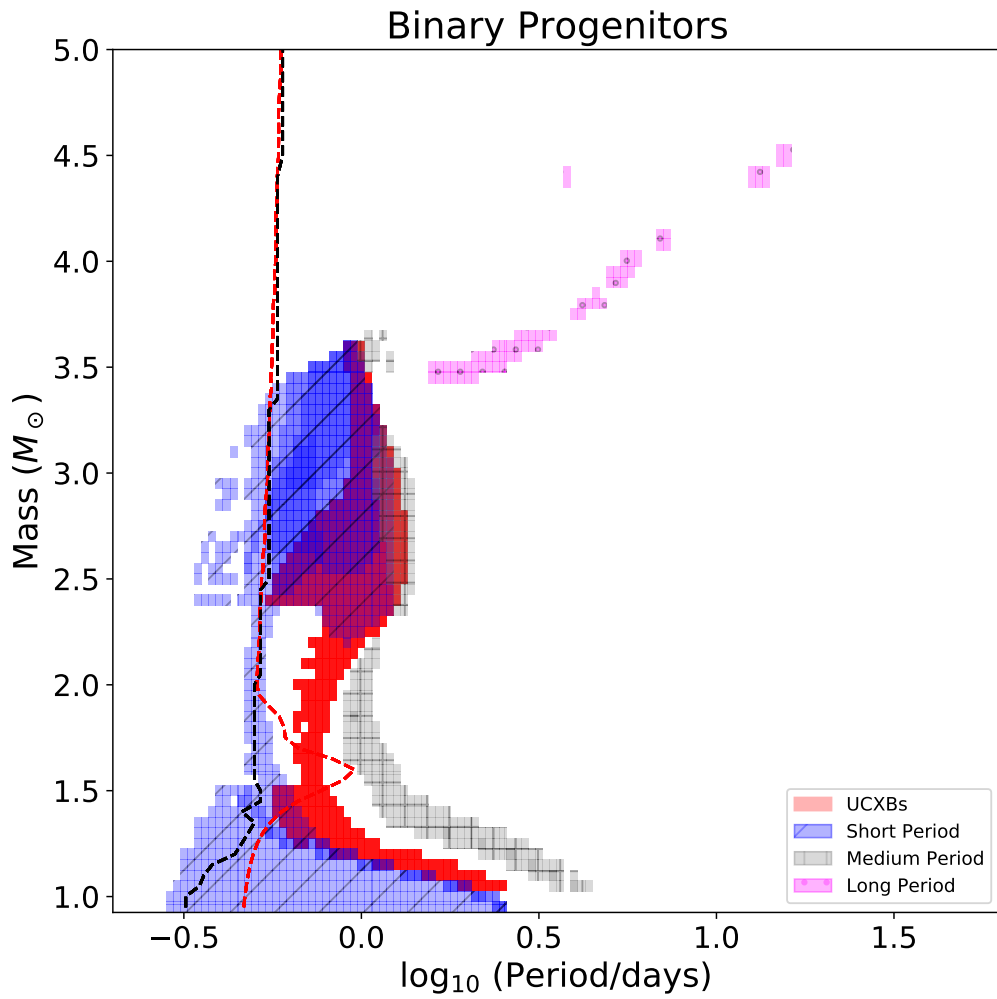


Figure 4.6: A similar figure to Figure 4.1 but using the wider bins for the observable quantities. The red and black dashed lines are the same as those described in Figure 4.1.

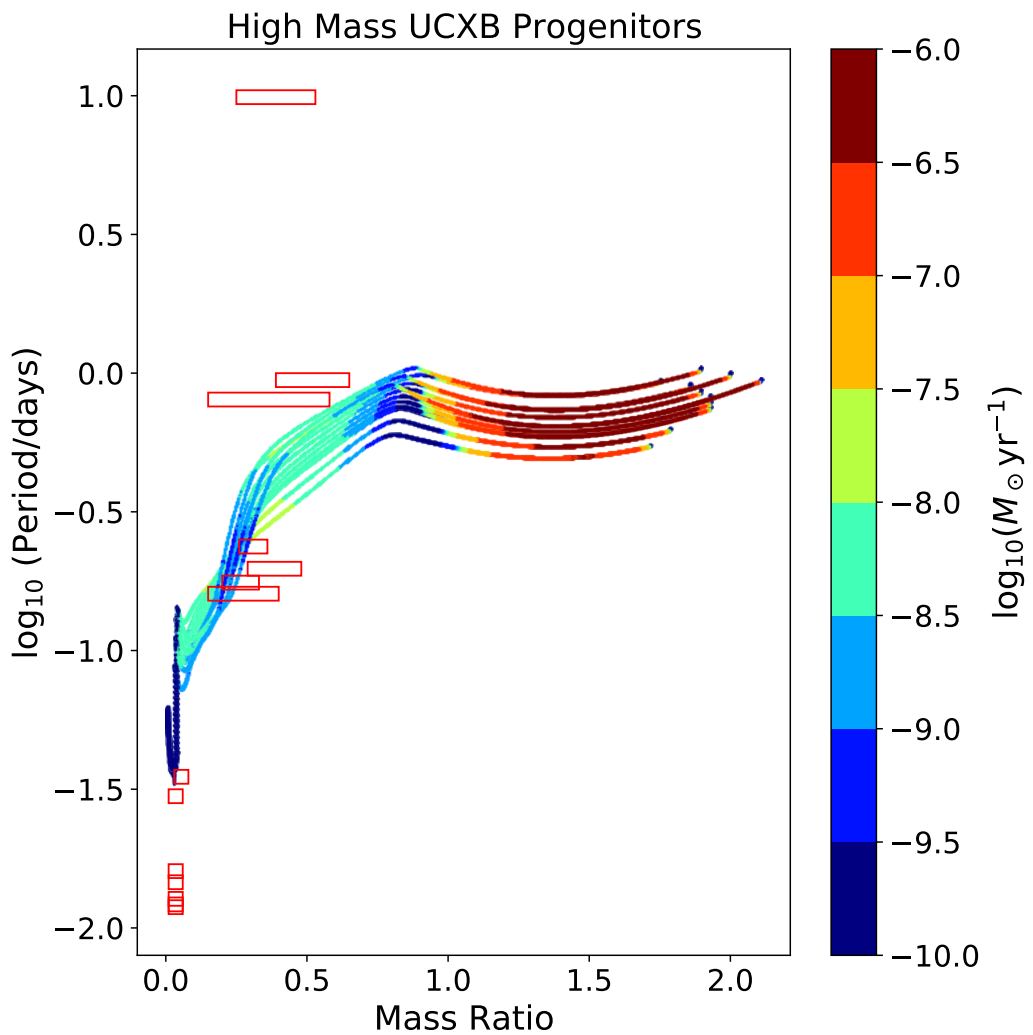


Figure 4.7: A sample of the high mass progenitors of UCXB systems found when using the wider bins. The red squares show the locations of the observed LMXBs using the wider bins. The colour bar shows the mass transferred  $M_{\text{tr}}$

we find that they can reach appropriately low mass ratios to match with observed UCXBs. However, the mass transfer rates drop below  $\log_{10}(\dot{M}_{\text{acc}}) = -10$  when the simulated binary reaches ultra-compact periods and no longer satisfies the condition for a persistent LMXB using Equation 4.6. These simulations instead reproduce transient UCXBs, which are outside the scope of this work. Additionally, these binaries can only shrink to periods of  $\log_{10}(P/\text{days}) - 1.6$  prior to expanding to longer periods as seen in Figure 4.7.

Similarly, when examining the progenitors with initial masses below  $M < 2.0M_{\odot}$  also reach appropriate low mass ratios and periods to match with UCXBs but similar to the high mass progenitors, do not reach sufficiently high mass transfer rates to satisfy Equation 4.6. Again, the mass transfer rates drop below  $\log_{10}(\dot{M}_{\text{acc}}) = -10$  resulting in the simulated systems better matching with transient UCXBs. This can be seen in Figure 4.8.

For the short period LMXBs, the extended MT bin results in a significant widening of the viable progenitors' initial periods. The new progenitors produce systems with periods and mass ratios similar to the observed systems, but the mass transfer rates greatly exceed our standard bins. The observed mass transfer rate appears to be the main constraint in reproducing short period LMXBs.

## 4.4 Rate Estimates

In this Section, we will discuss the progenitor formation rates. Unfortunately, due to the small number of observations, only an estimate can be done. We consider each of the existing observations as a binomial process. In a simple case, if all the progenitors would be formed only in one “bin”  $ij$ , the total number of systems  $N_{\text{f},ij}$  that needs to be formed per unit of time  $T$  for each given observed system  $k$  is related to the expected number of observations  $N_{\text{obs}}^k$

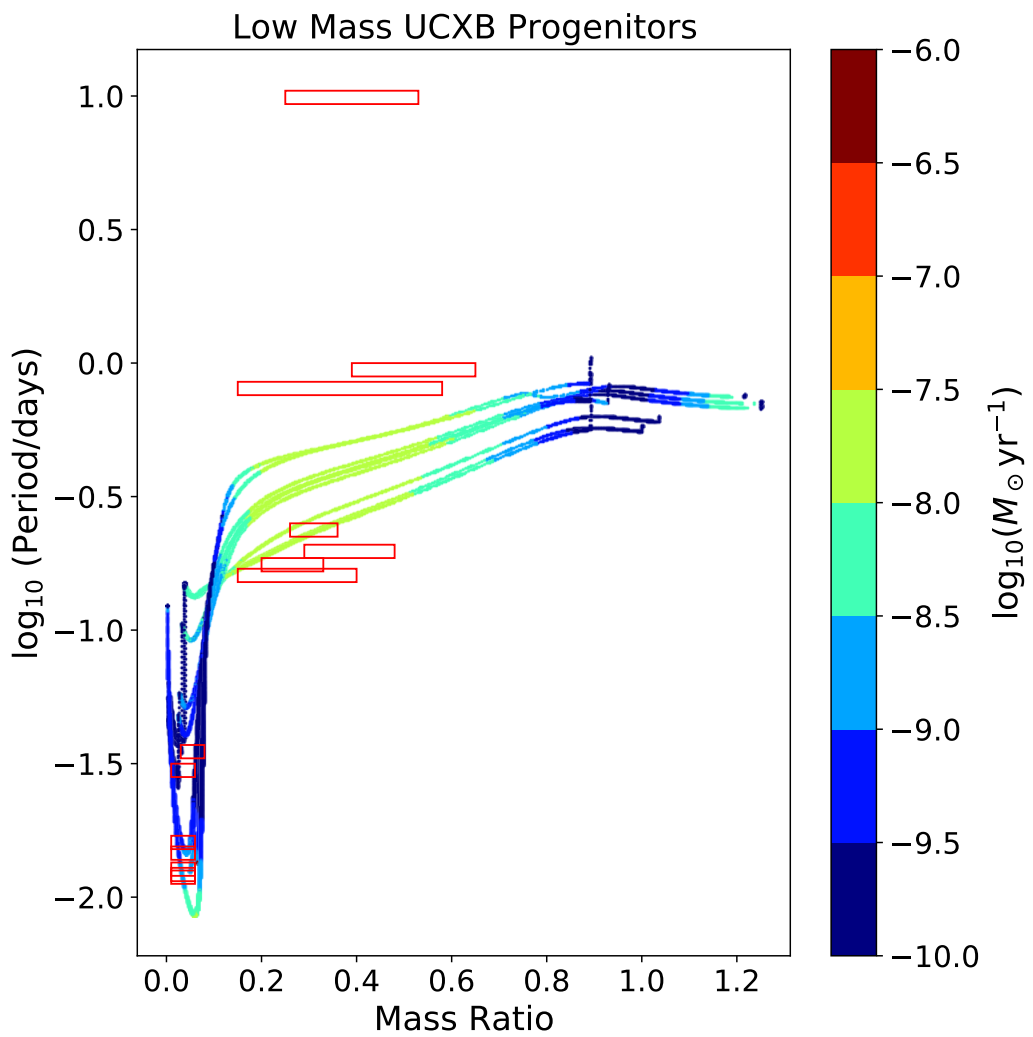


Figure 4.8: A sample of the low mass progenitors of UCXB systems found when using the wider bins. The red squares and colour bar are the same as in Figure 4.7.

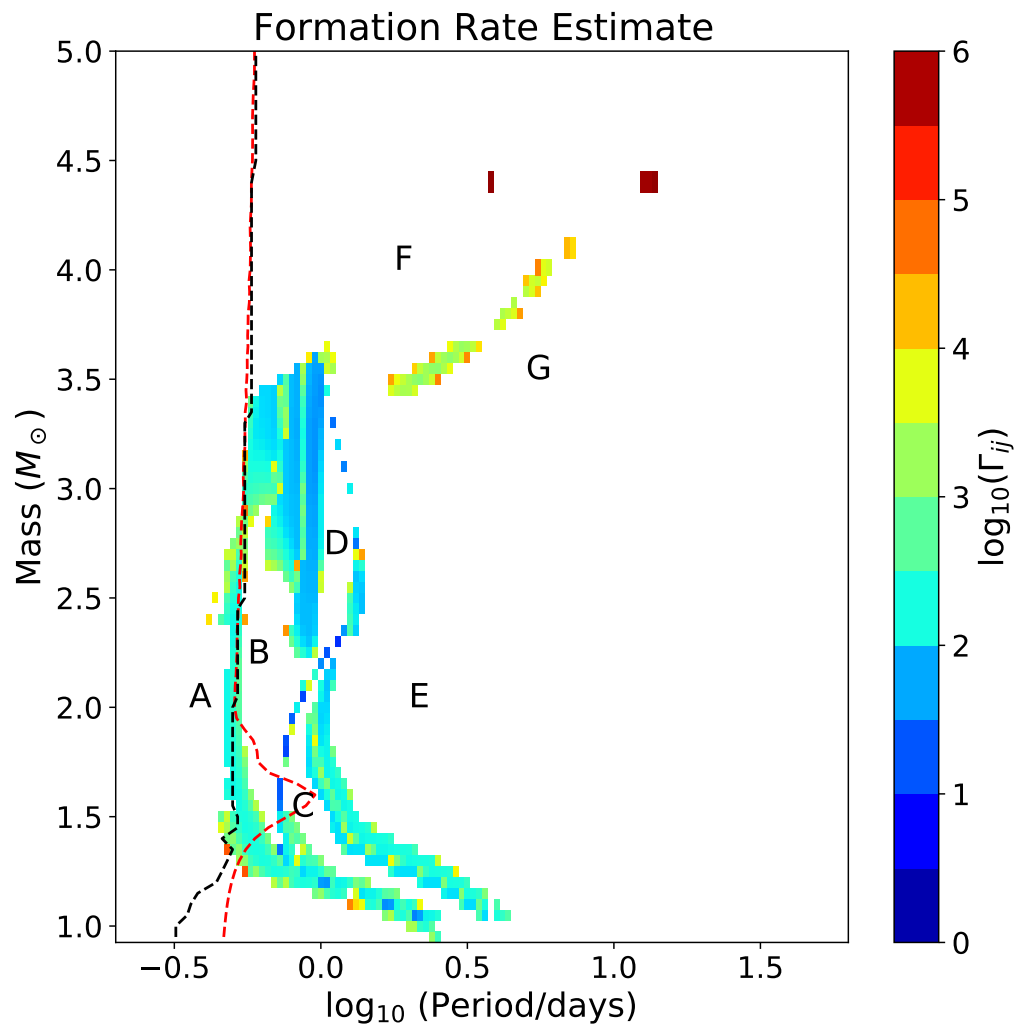


Figure 4.9: The minimum formation rate of the observed LMXBs, (see Equation 4.9). The labelled sections in the plot denote specific regions of the parameter space where the simulations do not overlap with any observed LMXBs.

System Name	$\log_{10}(P_i)$	$M_i$	$\Gamma_{\min}$	$\Gamma_{\text{avg}}$
UCXB				
4U 0513-40	0.08	1.2	92	363
2S 0918-549	-0.12	1.4	89	216
4U 1543-624	0.38	1.05	69	432
4U 1850-087	0.16	1.15	43	124
M15 X-2	0.36	1.05	31	96
Combined 5 UCXBs	0.28	1.1	123	203
4U 1626-67	0.06	2.3	11	339
4U 1916-053	0.12	2.6	17	760
Short period				
4U 1636-536	0.0	3.4	40	736
GX 9+9	-0.08	3.3	60	530
4U 1735-444	-0.16	3.45	93	2879
2A 1822-371	-0.32	1.75	163	1317
Medium period				
Sco X-1	-0.02	1.65	106	317
GX 349+2	0.04	2.2	63	1039
Long period				
Cyg X-2	0.34	3.5	1196	170631
Combined				
With Cyg X-2	–	–	2827	125913
Without Cyg X-2	–	–	1452	8766

Table 4.4: The table shows the initial period and mass resulting in the minimum formation rate. The subscripts min and avg denote the minimum and average. The rate  $\Gamma$  in units of systems per Gyr as calculated using equation 4.9. The period is the initial orbital period of the progenitor binary in  $\log_{10}(\text{days})$  and the mass,  $M_i$ , is the initial mass of the donor in  $M_\odot$ . The two combined rows at the bottom shows the average minimum and maximum calculated formation rates when we randomly select a progenitor for our observed LMXBs.

as

$$N_{\text{obs}}^k = N_{\text{f},ij}^k \frac{\tau_{ij}^k}{T} = \Gamma_{ij}^k \tau_{ij}^k . \quad (4.9)$$

Here  $ij$  are the seed mass and period combination that produces the system  $k$ ,  $\tau_{ij}^k$  is the time spent in the observed bin of interest, and  $\Gamma_{ij}^k = N_{\text{f},ij}^k/T$  is the formation rate of a given observed system  $k$  from the bin  $ij$ . In Figure 4.9 we present  $\Gamma_{ij}^k$  for each progenitor bin (calculations are made assuming that each  $N_{\text{obs}}^k = 1$ ). If the bin produces two or more observed binaries, we provide the value of the formation rate that is associated with the largest  $\tau_{ij}^k$ .

For each observed system  $k$ , with the adopted expected observation number  $N_{\text{obs}}^k = 1$ , we can find the bin that produces the binary with the longest  $\tau_{ij}^k$ . Suppose all  $k$ -LMXB formations result from the progenitors coming from this bin only. In that case, the associated total formation rate will be the smallest of various realizations of LMXBs total formations rates, produced either individually or by any combination, of all the bins that produce the system  $k$ . These formation rates,  $\Gamma_{\min}^k$ , are provided in Table 4.4.

In the case when  $m$  initial bins, with equal areas, are equally plausibly forming the observed system  $k$ , the binomial distribution can be written as

$$N_{\text{obs}}^k = N_{\text{f}}^k \frac{1}{m} \sum_m \frac{\tau_{ij}^k}{T} = \Gamma_{\text{av}}^k \frac{1}{m} \sum_m \tau_{ij}^k . \quad (4.10)$$

$\Gamma_{\text{av}}^k$  is the average formation rate of a given observed system  $k$  from all possible bins  $ij$ . Our bins are not equally sized. In the case when the progenitors are formed in  $m$  initial bins, and the probability of creation of the progenitor-system  $k$  is uniformly distributed over the initial parameter space in mass and period,

$$N_{\text{obs}}^k = \Gamma_{\text{av}}^k \frac{1}{\Delta A^k} \sum_m \tau_{ij}^k dA_{ij}^k . \quad (4.11)$$

Here  $\Delta A^k = \sum_m dA_{ij}^k$  is the total size of the progenitor region that produces

the observed system, and  $dA_{ij}^k$  is the size of the specific bin. The average formation rates  $\Gamma_{\text{av}}^k$  that take into account the sizes of the specific bins are provided in Table 4.4.

We note of course that there is no guarantee that the seed binaries are uniformly distributed in mass and period space, after a supernova event, and after likely a common envelope event, which both strongly affected their previous evolution and birth masses and periods, and hence the average formation rates are just for a reference, to understand the possible spread in the expected formation rates, as compared to the minimum formation rates of the same systems. In general, both the minimum and average formations rates do not vary strongly between the different type of LMXBs, except for Cyg X-2. Below we analyze these numbers for individual observed systems, as well as for the population as a whole.

#### 4.4.1 UCXBs

We find that the average formation rates for UCXBs are the lowest among all type of LMXBs. This is expected, as UCXBs with the observed parameters can live for a long time. For example, to produce systems similar to M15 X-2, an average formation rate of 96 systems per Gyr can explain its existence, the smallest average rate amongst our calculations. The progenitors that lead to the minimum formation rates are different for all the UCXBs with no clear trend in the initial properties that produce the minimum rate for the observed LMXBs.

The five UCXBs with the shortest period are very similar to each other. Anticipating this similarity, we consider a cuboid that encompasses all five systems and obtain the formation rates using for this cuboid that  $N_{\text{obs}} = 5$ . The cuboid spans a period range of  $-1.95 \leq \log_{10}(P/\text{day}) \leq -1.77$ , mass ratio of  $0.01 \leq q \leq 0.06$  and mass transfer rate of  $-9.8 \leq \log_{10}(\dot{M}_{\text{acc}}/M_{\odot}\text{yr}^{-1}) \leq -8.2$ . Due to the combined UCXB cuboid spanning a wider range in both period

and mass transfer rate, the amount of time a simulation spends in this bin of interest is increased, resulting in a lower required formation rate. The minimum formation rate for the combined 5 systems is 123 systems per Gyr, and the average formation rate of 203 per Gyr. This is the rate required to form all 5 systems.

Among our observed UCXBs, a subset of them are detected within globular clusters. 4U 0513-40, 4U 1850-087, and M15 X-2 are observed within globular clusters and because of this, we note additional caveats in regards to the calculated formation rate. Unlike UCXBs in a low density environment, UCXBs in a high density environment like a globular cluster may be formed through dynamical encounters or physical collisions (Verbunt, 1987; Ivanova et al., 2005, 2008). Bildsten and DeLooye (2004) calculated the expected UCXB formation rate through dynamical encounters as one per  $2 \times 10^6$  years per  $10^7 M_\odot$  of globular clusters. This roughly translates to  $\sim 500$  UCXBs formed in  $10^9$  years per  $10^7 M_\odot$  if the formation rate remains largely constant. It is unclear if the formation rate within globular clusters can be compared to the values we have calculated in Table 4.4.

Two UCXBs with the longest periods, 4U 1626-67 and 4U 1916-053, stand apart. To form them, a new evolutionary channel is required. It appeared that the minimum number of formations of progenitor systems required to explain their observations is the lowest on overall, only about a dozen in the Galaxy per Gyr. The average formation rate for 4U 1626-67 is similar to the other UCXBs, but 4U 1916-053 is the largest among UCXBs. For both of these higher period UCXBs, the lowest formation rate progenitors come from systems with initial periods  $M_i \lesssim 1.4 M_\odot$  with higher calculated rates coming from binaries where the initial mass  $M_i \gtrsim 1.5 M_\odot$ .

#### 4.4.2 Short and Medium Period

The formation rates for short and medium period LMXBs are comparable to that of UCXBs. The minimum formation rates are between 40 and 163 systems per Gyr. The average rates are a factor of 2-3 larger than for UCXBs ranging from  $300 - 3000$  systems per Gyr. This suggests that whatever process in nature creates the progenitor binaries that later appear as short or medium LMXBs, more of such progenitors might be necessary to be created than for UCXB progenitors, albeit not dramatically. There is a possible trend in the value for the minimum formation rate for short period systems, such that the calculated rate is larger for longer period LMXBs. Medium period LMXBs do not follow that trend, however.

#### 4.4.3 Long Period

The observed binary Cyg X-2 is the most anomalous system in the calculations. The progenitor mass, the progenitor period, and the required progenitor formation rates are all significantly higher than any other system. With the average progenitor rate of  $\Gamma_{\min} \gtrsim 1.7 \times 10^5$  systems per Gyr, the formation rate needed to make Cyg X-2 is nearly two orders of magnitude larger than any other observed LMXB. The minimum formation rate is substantially more reasonable,  $\Gamma_{\min} = 1196$  per Gyr. The high value of the minimum formation rate indicates that this system was unlikely formed by a random progenitor that can make Cyg X-2 (see Figure 4.2), and has likely been formed by the progenitor resulting in the minimum rate, specifically, with the initial mass of  $M = 3.5M_{\odot}$  and the initial orbital period of  $\log_{10}(P/\text{days}) = 0.34$ . As is discussed below in section 4.5, systems formed in the parameter space near this point would create LMXBs that are overall similar, but a bit different, to Cyg X-2. It is also plausible that Cyg X-2 is just a random realization of such progenitors, and is not itself indicative of a specific intensive pre-LMXB formation

channel. As shown in section 4.3.5, effective temperature plays a significant role in constraining the progenitors of high initial mass or high initial period binaries. From Figure 4.9 we see the general trend that as the initial progenitor mass increases, the calculated rate also increases. Additionally, the progenitors of Cyg X-2 appear to have an optimal initial period for each given mass such that the formation rate is the lowest at that period and is increasing as the progenitor deviates more from the initial period.

#### 4.4.4 Combined Rates

The summed minimum rate required to produce the observed sample of LMXBs is only about 3000 binaries per Gyr. In comparison, the average rate is not very useful as it is dominated by Cyg X-2 and requires significantly more systems per Gyr, most of which are donors with initial masses above  $3.5M_{\odot}$ . The obtained formation rates encompass many orders of magnitude, making it difficult to make predictions of the actual formation rate.

Beyond UCXBs, it is unlikely that every observed LMXB is produced using the progenitor that results in the lowest rate. To obtain a more realistic value, we randomly select one successful progenitor per observed LMXB to determine a combined rate. We do this random calculation 10000 times to find a distribution of possible values. The randomized calculated rates are presented in the bottom two rows of Table 4.4. Unfortunately, randomly selecting a progenitor for each system (and hence using the whole range of possible rates) led to the predicted rate being dominated by the progenitor of Cygnus X-2. We reiterate that the formation rates calculated for Cygnus X-2 are significantly larger than those required for other observed LMXBs with the minimum rate being an order of magnitude larger than any other calculated rate and the average being two orders of magnitude larger (see Table 4.4). In both cases where we calculate a rate with and without Cygnus X-2, the minimum number of formed pre-LMXB systems is on a similar order of magnitude with a

Region	
A	Difficult to produce progenitor LMXBs.
B	Should produce LMXBs with $-0.75 \lesssim \log_{10}(P/\text{days}) \lesssim -0.25$ , $q \lesssim 1, \log_{10}(\dot{M}/M_\odot \text{ yr}^{-1}) \sim -7.5$
C	Should produce LMXBs similar to Sco X-1.
D	Early portion of evolution short lived. End of evolution has no mass transfer.
	Intermediate portion should be detectable with $\log_{10}(\dot{M}/M_\odot \text{ yr}^{-1}) \sim -8.5$
E	High mass ratio progenitors do not satisfy condition from equation 4.6 for persistent systems.
	Low mass ratio systems should be observable.
F and G	High mass transfer rates result in short lived binaries.

Table 4.5: A summary of the different regions of our parameter space and a summary of how observable a system from this region is.

few thousand systems formed per Gyr. This value is larger than the absolute minimum progenitor formation rate as it is calculated by randomly selecting progenitors. While the total number of systems that are formed with an NS can be much higher than our minimum number, as these systems do not need to be limited to the progenitor space, we stress that the minimum number that we have obtained (2827 with Cygnus X-2 and 1452 without Cygnus X-2) is the minimum number of successful NS binaries formation events that can explain the observed population of LMXBs generated by randomly selecting progenitors. Our average values (125913 with Cygnus X-2 and 8766 without Cygnus X-2) are more likely to represent the formation rate that nature has to provide.

## 4.5 Unobserved Systems

Only part of the entire parameter space leads to the production of the observed LMXBs, see Figures 4.1 and 4.9. That space is not continuous, and there are gaps in the parameter space – the binaries originating from those gaps did not

produce a binary comparable to the sample of observed LMXBs we considered. In this Section, we investigate what happens to the binaries that started their evolution in the “gaps”. To take a closer look, we split the “unsuccessful” parameter space into seven distinct regions, see Figure 4.9. Region “A” denotes the portion of parameter space where the progenitor binaries will start with very short periods,  $P_i \lesssim 0.5$  days. The three regions between the UCXB, short period, and medium LMXBs are denoted by “B”, “C”, and “D”. Regions “F” and “G” represent regions with initial periods  $P \lesssim 10$  days and  $P \gtrsim 10$  days with high initial masses,  $M_i \gtrsim 3.0M_\odot$  respectively. The region “E” is for seed systems with a long initial period and initial masses below  $3.0M_\odot$ . Below, we examine these regions to determine if these LMXBs have properties that result in systems that, in theory, could be observable.

#### 4.5.1 Region “A”: Short Initial Periods

The short initial period region of our parameter space is primarily on the left of the black dashed line in Figures 4.1 and 4.9, with only a small part of this region located to the right of the dashed line, for donors with  $M_i \lesssim 1.3M_\odot$ . To reiterate, the black dashed line denotes the initial periods for which the simulated system with this donor mass is at its RLOF at the start of the simulation. Any system with a shorter initial period overfills the Roche lobe at the donor’s ZAMS. For the binaries with  $M_i \lesssim 1.3M_\odot$ , there is a portion of the parameter space where the system has to evolve from ZAMS to start the mass transfer, and we will focus on this parameter space.

In Figure 4.10, we show the sample of the systems with the short initial periods and low masses. The simulated systems that have progenitors in this region of our parameter space result in binaries that only partially match with observed LMXBs. In general, the simulated systems have mass transfer rates that exceed the observed rates of 4U 1636-536, GX 9+9 and 4U 1735-444. 2A 1822-371 on the other hand, has sufficiently high mass transfer rates to match

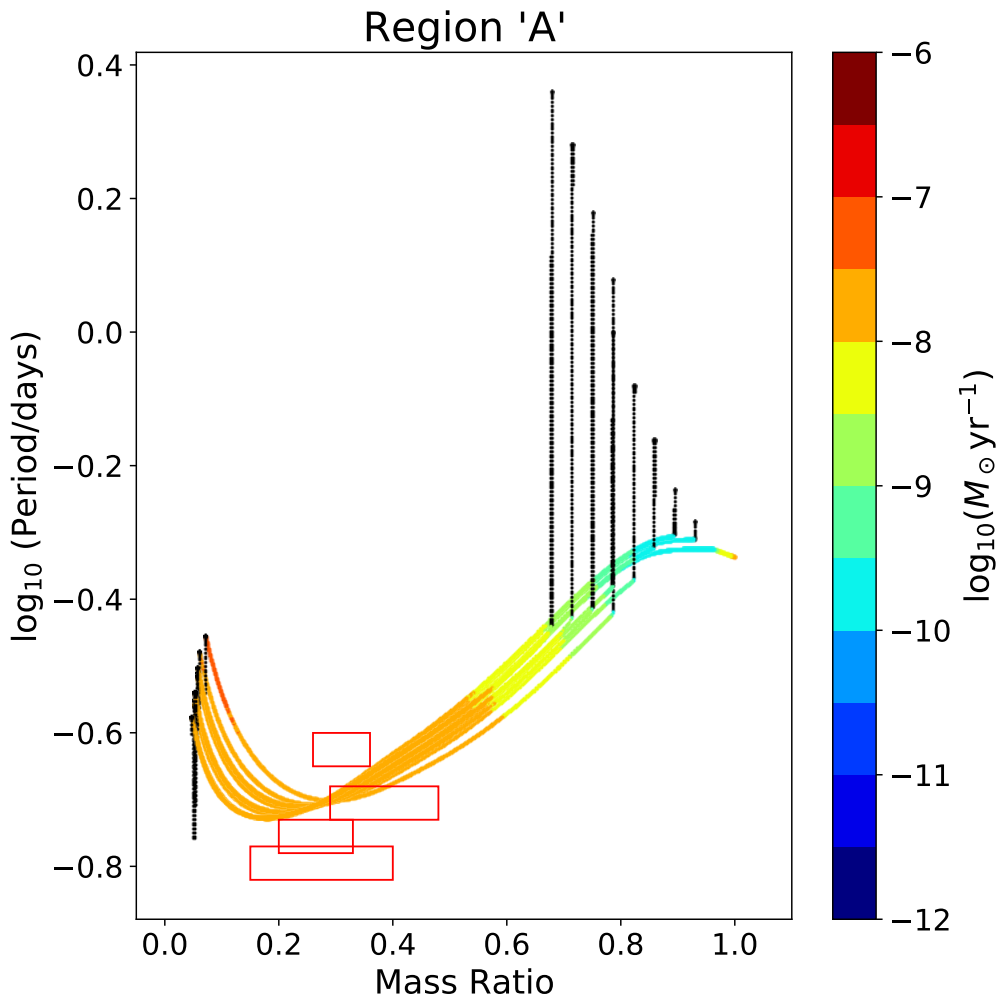


Figure 4.10: A subset of simulated systems with a short initial period,  $P_i \lesssim 0.5$  days. The color of the lines indicates the mass transfer rate of a given simulation at that point. The red boxes show the mass ratio and period bins of the four observed short period LMXBs in Table 4.2. The black points show portions of the evolution where the binary does not experience RLOF.

with the simulated systems, but the observed period of 2A 1822-371 exceed the simulated periods. These short initial period, low initial mass progenitors produce LMXBs that have high mass transfer rates similar to 2A 1822-371 and similar mass ratios, but with shorter periods. Additionally, these simulated systems spend between  $10^7$  to  $10^8$  years transferring mass. We can make an estimate of a formation rate required to produce one observable LMXB with  $\log_{10}(P/\text{days}) \sim -0.7$ ,  $q \sim 0.3$  and  $-7.5 \leq \log_{10}(M_\odot \text{ yr}^{-1}) \leq -9$  using Equation 4.9. With the number of possible progenitors in this region of our parameter space resulting in a system with similar properties, we calculate a progenitor formation rate of a few hundred per  $10^9$  years. Therefore, we may expect that there are observable binaries that have not been detected in this region of the parameter space. The limiting factor in our ability to detect these systems would be the formation rate of the progenitors.

#### 4.5.2 Region "B": $M_i \sim 1.5M_\odot$ , $P_i \sim 1 \text{ day}$

This region of our parameter space is denoted by the letter "B" in Figure 4.9 and lies between the progenitors of UCXBs and 2A 1822-371. The evolutionary tracks of the subset of the progenitor binaries can be seen in Figure 4.11. The simulated systems initially experience high mass transfer rates, exceeding  $\log_{10}(\dot{M}/M_\odot \text{ yr}^{-1}) \gtrsim -7$ , with their orbital period remains almost unchanged and is around  $\log_{10}(P/\text{days}) \sim -0.3$  until the mass ratio flips. This initial phase of evolution is very short-lived and is therefore difficult to detect. Once the systems have reached a mass ratio of  $\sim 1$ , the evolution slows down, and the binaries are now long-lived. During this phase the mass transfer rate ranges between  $-7.5 \leq \log_{10}(\dot{M}/(M_\odot \text{ yr}^{-1})) \leq -9$ , while the orbital period of the binary decreases from  $\sim 10$  hours to  $\sim 2$  hours. During this long period of evolution, the mass transfer rate consistently satisfies the condition for a persistent LMXB and should be observable. A binary with a period  $\sim 8$  hours and mass ratio  $\sim 0.5$  spend approximately  $10^7$  years transferring mass

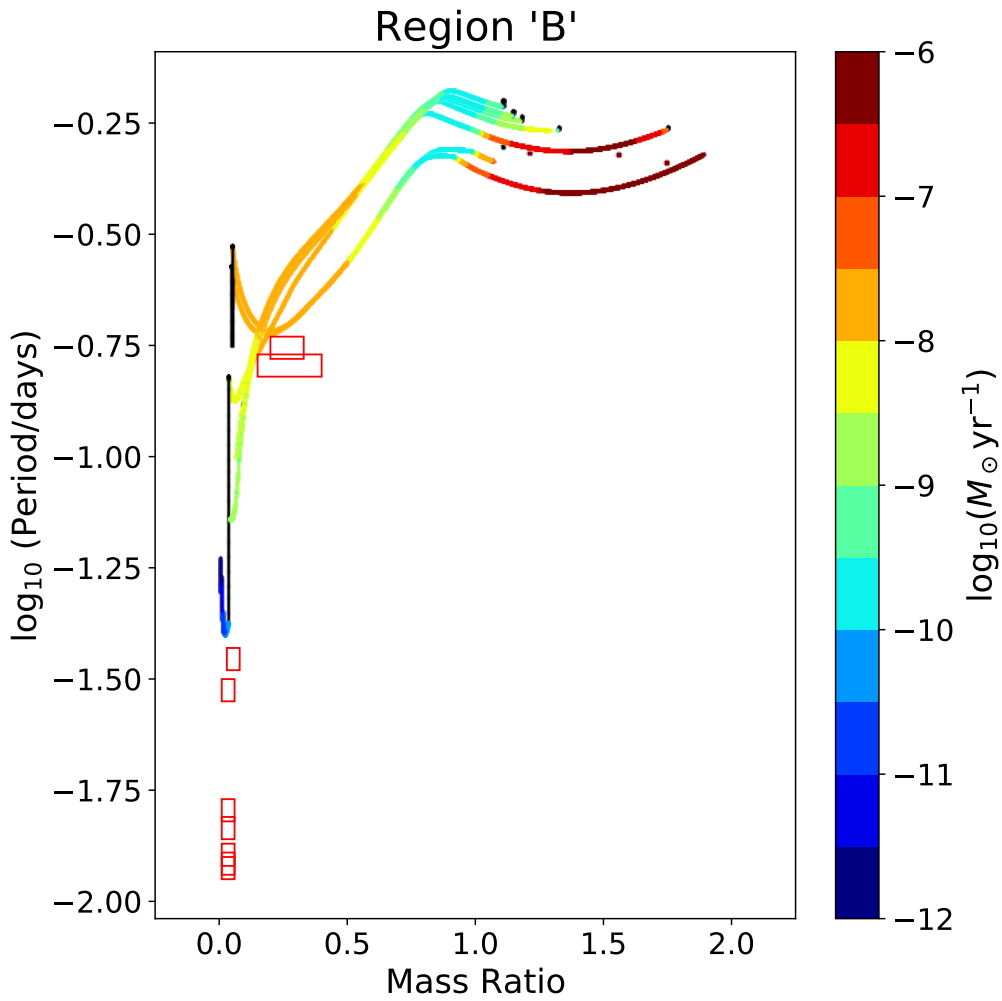


Figure 4.11: A subset of simulated systems from the region denoted as "B" in Figure 4.9.

$\log_{10}(\dot{M}/(M_\odot \text{ yr}^{-1})) \approx -8$ . This results in a minimum required formation rate of a few hundred systems per Gyr in this region of the parameter space.

#### 4.5.3 Region "C": $M_i \sim 2.0 M_\odot$ , $P_i \lesssim 0.5 \text{ days}$

The simulations in region "C" of our parameter space have initial periods that exceed the bifurcation period but are not long enough to produce the medium period systems. The simulated systems in this region of our parameter space have very low mass transfer rates in the early stages and the end of their

evolution, but significantly higher mass transfer rates in the middle of the evolution with the binary eventually detaching at the end of its evolution (see Figure 4.12). These simulated systems all converge in a similar region of the parameter space with orbital period,  $P \sim 15$  hr with mass ratios in the range of  $0.2 \lesssim q \lesssim 0.8$  and mass transfer rate  $\log_{10}(\dot{M}/M_\odot \text{ yr}^{-1}) \sim -7.7$ . These properties would result in an LMXB that is very similar to Sco X-1, but with a shorter period. The example systems that are shown in Figure 4.12, all spend on the order of  $10^7$  years in a persistent state with mass transfer rates exceeding  $10^{-8} M_\odot \text{ yr}^{-1}$ . Similar to Sco X-1, we would also predict a formation rate on the order of a few hundred systems per Gyr if the mass ratio bin remained wide. Further constraining the mass ratio to a range between  $0.4 \lesssim q \lesssim 0.7$  where the mass transfer rate is highest at  $\log_{10}(\dot{M}/M_\odot \text{ yr}^{-1}) \sim -7.5$ , the formation rate would need to increase to a few thousand systems per Gyr.

#### 4.5.4 Region “D”: $M_i \sim 3.0 M_\odot$ , $P_i \sim 1$ day

This region of our parameter space is denoted by the letter “D” in Figure 4.9 and lies between the progenitors of UCXBs and GX 9+9. The evolutionary tracks of this subset of progenitors can be seen in Figure 4.13 and appears very similar to those in Figure 4.11 with these two regions forming a self-similar family of evolutionary tracks. These simulated systems also initially experience mass transfer rates that exceed  $\log_{10}(\dot{M}/M_\odot \text{ yr}^{-1}) \gtrsim -7$  while the orbital period remains at around  $P \approx 1$  day with their orbital period remains almost unchanged and is around  $\log_{10}(P/\text{days}) \sim -0.2$ . This high mass transfer rate is short-lived and difficult to detect until the systems reach a mass ratio of  $\sim 1$ , where mass transfer slows down and the binaries are now long-lived. Despite the mass transfer rate slowing down, they still remain large enough to be considered as persistent. The mass transfer rates decrease to values between  $-8.0 \lesssim \log_{10}(\dot{M}/M_\odot \text{ yr}^{-1}) \lesssim -9.0$  while the period decreases from  $\sim 1$  day to  $\sim 2$  hours. Following the simulations in region “B”, these progenitors also

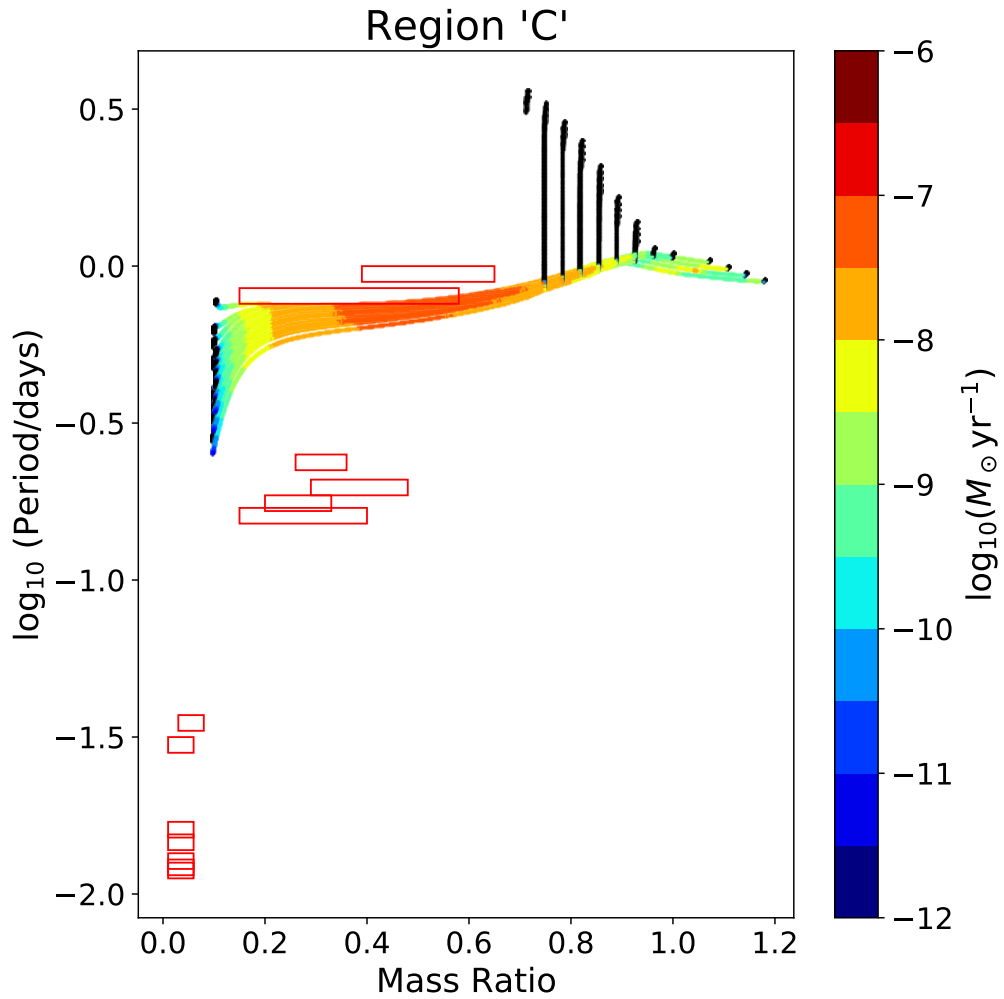


Figure 4.12: A subset of simulated systems from the region denoted as "C" in Figure 4.9. The red boxes show the bins for the UCXB and short period observed binaries.

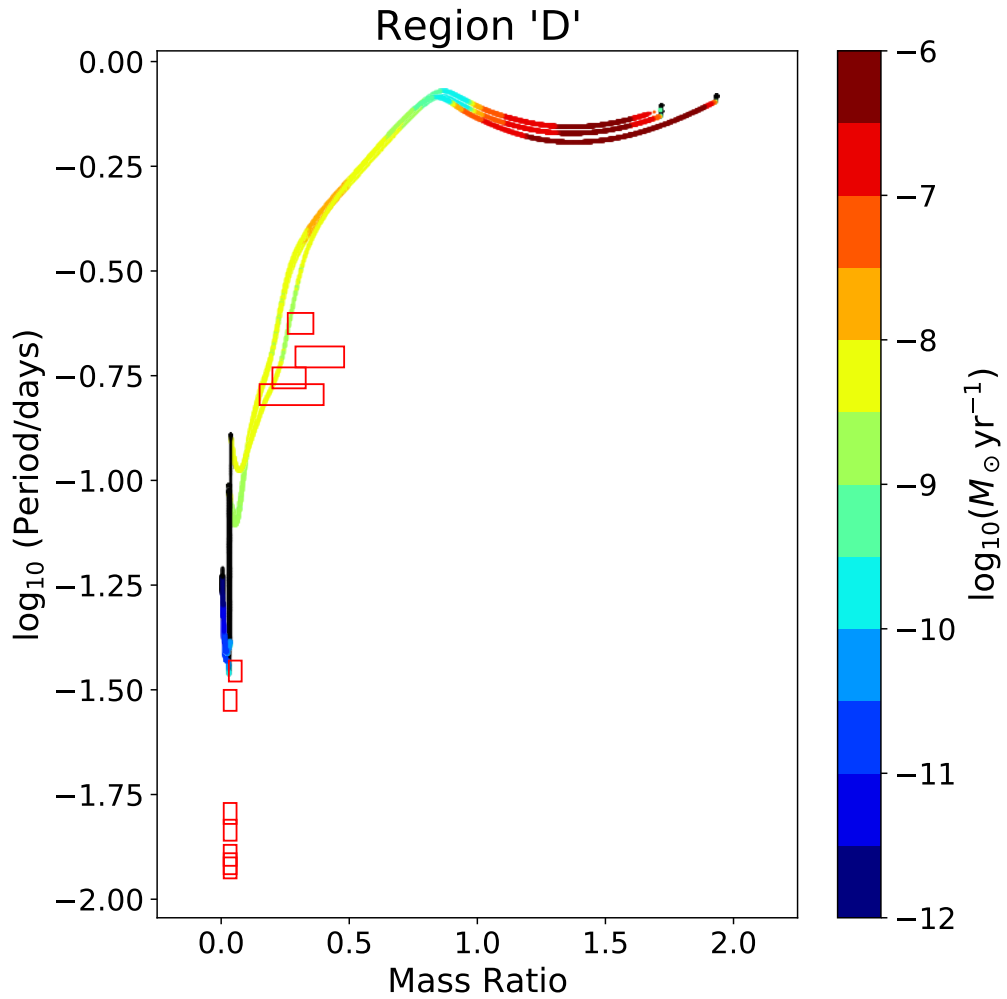


Figure 4.13: A subset of simulated systems from the region denoted as “D” in Figure 4.9. The red boxes show the bins for the UCXB and short period observed binaries.

finish their evolution by detaching and becoming unobservable.

#### 4.5.5 Region “E”: $P_i \gtrsim 1.5$ days, $M_i \lesssim 3.0M_\odot$

The binaries with  $P_i \gtrsim 1.5$  days and  $M_i \lesssim 3.0M_\odot$  are in region “E”, see Figure 4.14. Binaries with high initial masses and long initial periods are covered in region “G”. These binaries initiate RLOF when the periods shrink to  $\sim 1.3$  days and during mass transfer the mass ratio decreases from 1 to  $\sim 0.1$  prior to detaching. The orbital period remains well constrained during this time at  $\sim 1$  day. The mass transfer rates of these binaries are above the critical value necessary to be deemed a persistent system in accordance with Equation 4.6. The key difference between these simulated systems and the viable progenitors of Sco X-1 and GX 349+2 is that the simulated systems in region “E” have periods that are too large to match with our medium period systems. The simulated systems spend  $\sim 5 \times 10^6$  years with  $\log_{10}(P/\text{day}) \sim 1$  day,  $0.2 \leq q \leq 0.7$  and  $-9 \lesssim \log_{10}(\dot{M}/M_\odot \text{ yr}^{-1}) \lesssim -7$  suggesting a very high minimum formation rate of a few thousand systems in this observable region per Gyr.

#### 4.5.6 Regions “F” and “G”: High Initial Mass

For binaries with high initial donor masses in region “F” and “G”, these systems initially experience rapid mass transfer over  $10^{-7} M_\odot \text{ yr}^{-1}$ . With such significant mass transfer rates, the binary rapidly evolves to lower mass ratios, larger orbital periods, and smaller MT rates. Using Equation 4.6, we find that once the orbital period is a few days or more, to be classified as a persistent binary, the required mass transfer rate must be  $\log_{10}(\dot{M}/M_\odot \text{ yr}^{-1}) \gtrsim -7$ . However, a binary can not live long at such a high MT rate. These conflicting properties – a short time while having a “persistent” MT rate and longer time while “transient” – are the likely reasons why persistent binaries with large

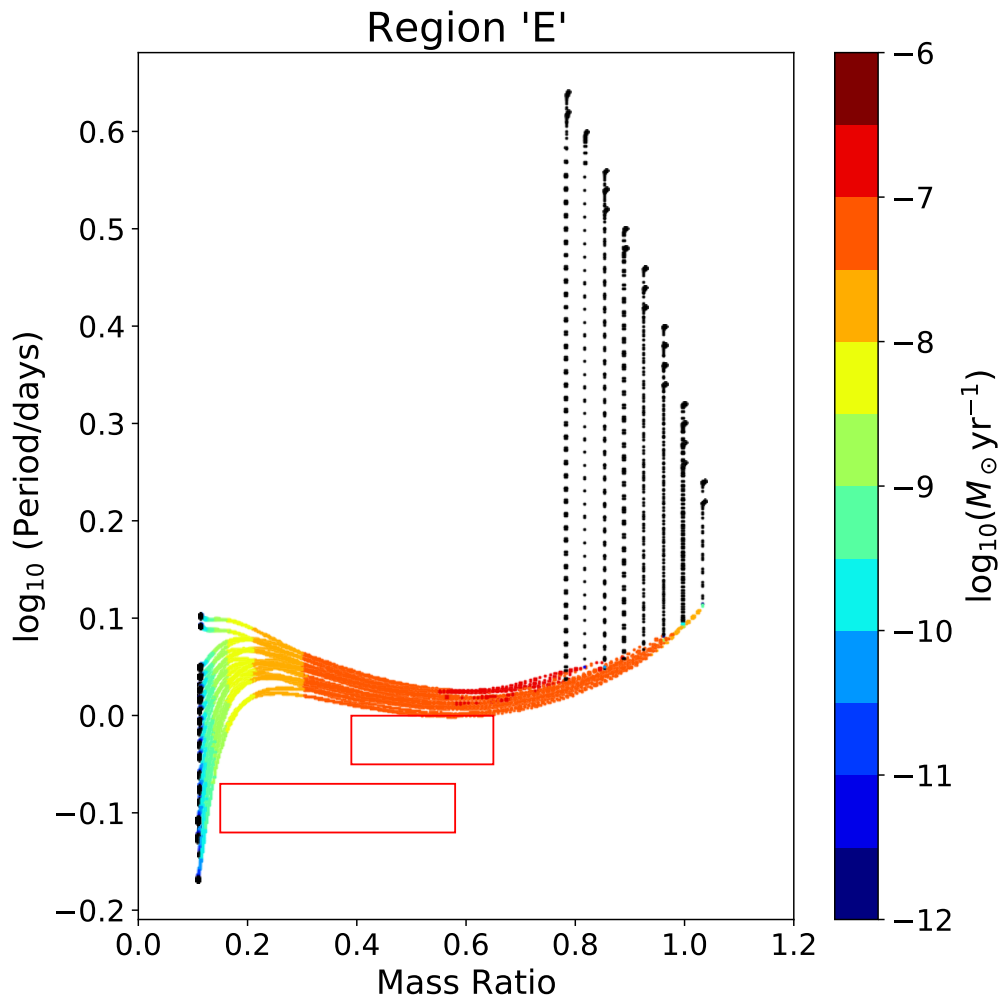


Figure 4.14: A subset of our parameters space such that the progenitor binaries have initial periods longer than 1.5 days and initial masses less than  $3.0 M_\odot$  (region “E”). The red boxes show the mass ratio and periods of the two observed medium period LMXBs in Table 4.2.

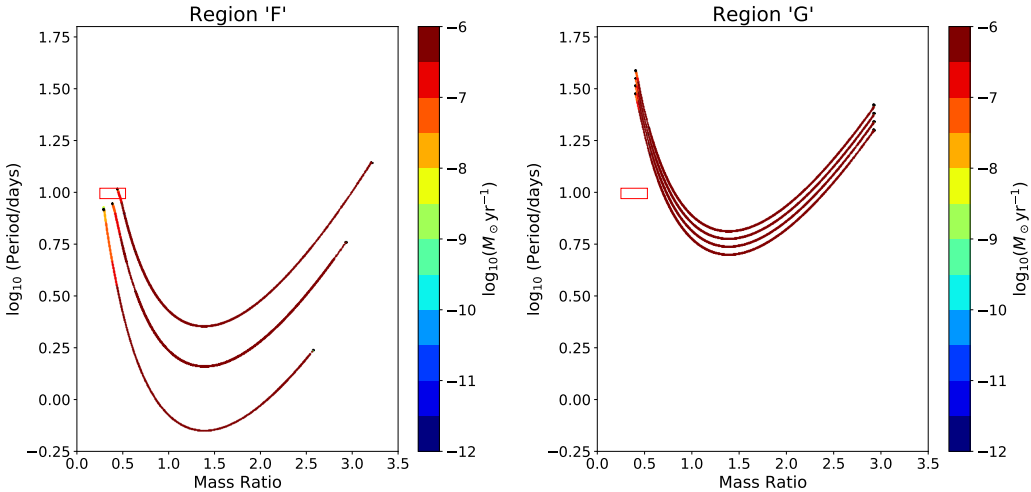


Figure 4.15: A subset of simulated systems with the initial donor masses exceeding at least  $3.5M_{\odot}$ , and more massive than Cygnus X-2 progenitors for each given initial orbital period.

orbital periods are difficult to detect.

#### 4.5.7 Uniform Initial Parameter Space Hypothesis

As follows from the considerations for various “unobserved” regions above, there are regions that can also produce persistent systems. We do not have good guidance on the initial distribution of the seed binaries, which are themselves the results of the primordial binaries being evolved through a supernova, and likely a common envelope event. However, at the very least, we can test what happens if the seed binaries were formed uniformly in  $\log_{10} P - M$  parameter space. We considered the random uniform birth of seed binaries in the  $\log_{10} P - M$  parameter space. Further, we check if they can be observed (at the same fixed moment of time) based on their lifetimes as persistent systems. We made 1000 realizations that would consist of 14 persistent LMXBs. Out of our 1000 random realizations, over half don’t produce any persistent systems that match with an observed LMXB. On average,  $\lesssim 0.6$  LMXB in such realizations would be consistent with the observed sample of the persistent LMXBs. The

maximally consistent realization resulted in 3 LMXBs similar to the observed sample. Out of our 1000 realizations, 16 random progenitor sets result in 3 LMXBs similar observed sample. Averaging over these 16 sets, 2.3 matched with short periods systems, 0.3 matched with medium period and 0.4 matched with long systems. None of our random samples could reproduce an UCXB. The other persistent systems produced in these sets are most commonly found to originate from the regions ‘B’, ‘D’, ‘F’ and ‘G’. Using this random sampling with 1000 realizations, we produce zero progenitor systems from the region ‘C’ in our parameter space. The modelled but unobserved persistent LMXBs come from relatively high mass donors  $M_i \gtrsim 2.5M_{\odot}$ . This suggests that uniform distribution of donors in mass in pre-LMXB binaries, after a supernova and presumably a common envelope event, is not likely in nature.

## 4.6 Conclusion

Using the CARB MB from Van and Ivanova (2019) we obtained the possible progenitors of the observed persistent LMXBs with known orbital periods, mass ratio, and mass transfer rates. This was done by searching through the entire space of theoretically possible MT systems to infer possible initial conditions of the observed ones. Our results show that the viable progenitors of the observed LMXBs are located in a small part of the plausible parameter space, see Figure 4.9. The pattern of the progenitors’ origins splits the persistent LMXBs that we analyze into distinct groups based on their currently observed periods.

Using these progenitors, we can calculate the minimum and the average formation rates, using the amount of time each progenitor spends appearing similar to an observed LMXB. The minimum formation rate is the value calculated using the simulated system that spends the largest amount of time matching an observed LMXB whereas the average formation rate uses random distribution among all plausible progenitors. The minimum formation rates

for nearly all observed LMXBs are in the range of a few dozens to a hundred systems per Gyr in the Milky Way, while the average formation rates are in the range of a hundred to a few thousand systems per Gyr in the Milky Way. Cyg X-2 is an outlier with a significantly higher range than all other systems. Without Cyg X-2, we find that the absolute minimum number of pre-LMXB binaries that needs to be formed per Gyr in the Milky Way to explain the observed sample of persistent LMXBs is about 1500 per Gyr. At the same time, a most expected number of seed binaries formation is about 9000 LMXBs per Gyr.

The key properties of the progenitors are as follows:

- All UCXB systems have progenitors slightly below the bifurcation period. This period range is very narrow with the obtained minimum formation rates ranging between 11 to 92 systems per Gyr and the average formation rates ranging from 96 to 760 systems per Gyr.
- Short period LMXBs with periods on the order of a few hours have initial progenitor periods shorter than the bifurcation period with initial masses ranging from  $\sim 1M_{\odot}$  to  $\sim 3.5M_{\odot}$ . The short period LMXBs have the minimum formation rates similar to UCXBs, but our calculations predict the average formation rates much larger than for UCXBs. The average formation rates range between 530 and 2879 progenitor systems per Gyr.
- Medium period LMXBs with periods ranging from tens of hours to approximately a day have initial periods slightly larger than the bifurcation period at lower masses, and share common progenitors with UCXBs at masses exceeding  $\sim 2M_{\odot}$ . The minimum formation rates for medium period systems are very similar to UCXBs and short period systems, ranging from 63 to 106 systems per Gyr. The average formation rates are also similar, ranging from 317 to 1039 systems per Gyr.

- Cyg X-2, our only LMXB with an observed period on the order of tens of days, is an outlier. Unlike the other LMXBs we tested, progenitor space for Cyg X-2 lacks a clear structure. The rates necessary to reproduce Cyg X-2 are significantly higher than any other LMXB and dominates our calculations with the minimum formation rate ranging from  $\sim 1200$  to  $\sim 1.4 \times 10^6$ , and the average rate of over  $1.7 \times 10^5$  systems per Gyr. The high calculated formation rate indicates that Cyg X-2 is difficult to reproduce.

Of equal importance as our results showing the viable progenitors to observed LMXBs, is finding gaps in our progenitor parameter space where no observed systems have been detected. The main regions of interest are regions "B", "C", and "D" in Figure 4.9. These progenitors' properties lie between the systems that produce observed LMXBs but have not resulted in any observable systems. This implies one of two possibilities, these progenitor properties are difficult to create in nature and no observed LMXBs exist, or these systems exist and simply have not been observed. Based on the properties of the systems from these progenitor regions, we have identified some observed LMXBs with partial observations that may match our simulations, examples of such systems are given in Table 4.6.

Testing the scenario where seed binaries are uniformly formed in our parameter space, we check if this random distribution results in observable persistent LMXBs. Randomly generating 1000 realizations of progenitor systems that result in 14 persistent LMXBs, we find that over half don't produce any persistent systems that match with an observed LMXB and none of our 1000 realizations produce any UCXBs. Our random sampling also produces no progenitors from region 'C' in our parameter space. The random sampling suggests that the unobserved persistent LMXBs would likely come from higher mass donors  $M_i \gtrsim 2.5M_\odot$  and so we can conclude that LMXBs seed binaries can not be formed uniformly in the donor mass. To explain the observed number of

System	$\log_{10}(P)$	$\log_{10}(\dot{M}_a)$	Region
4U 1746-37	-0.67	-9.0	D
2A 0521-720	-0.47	-7.4	B
4U 1624-49	-0.06	-8.3	C

Table 4.6: Examples of possible LXMBs that would be produced in the gaps in our progenitor space. All three systems lack an observation for mass ratio and the mass transfer rates are approximate values. The mass transfer rate is in units of  $\log_{10}(M_\odot \text{ yr}^{-1})$ . The period is in units of  $\log_{10}(\text{day})$ . References: A09 - Agrawal and Misra (2009), B04 - Bałucińska-Church et al. (2004), B09 - Balman (2009), C12 - Coriat et al. (2012), L05 - Lommen et al. (2005), L07 - Liu et al. (2007), S01 - Sidoli et al. (2001), X09 - Xiang et al. (2009)

UCXBs, the initial distribution of periods of LMXB seed binaries can not be uniform either.

Further observations of these systems to constrain the properties and, more importantly, determine an approximate value for mass ratio would confirm if the proposed systems in Table 4.6 match our simulations. Additionally, if we had more systems with well-constrained periods, mass transfer rates and mass ratios, we would be able to further compare our simulated results to observed LMXBs. As the number of observed LMXBs with defined mass ratios, periods and mass transfer rates increases, any progenitor in our parameter space that fails to match with an observed system implies that binaries with that specific initial mass-period configuration are not likely formed from the primordial binaries. With the upcoming Gaia DR3 containing binary systems, we expect the number of observed LMXBs we can compare to will greatly increase, allowing us to probe the progenitor parameter space more effectively.

# Chapter 5

## Conclusion

Nata: keep the same tense, past tense. As you have done that. Do not change from past to present in this section, especially in the same sentence.

Through this work, I have thoroughly shown the weaknesses of the commonly used Skumanich magnetic braking prescription and propose two alternative prescriptions, a boosted Skumanich and CARB magnetic braking, that are more physically motivated. I was able to use these two magnetic braking schemes to produce comprehensive grids of simulated LMXBs to show their effectiveness. However, the most effective form of the boosted Skumanich was created by adding ad-hoc wind and convection terms. These two factors are taken into account more physically when formulating the CARB prescription. For CARB magnetic braking, I was also able to calculate possible progenitor formation rates.

### 5.1 Modified Skumanich

In Chapter 2 I derived a modified Skumanich magnetic braking scheme which could be scaled to include the effects of convection and additional winds. By generating a large grid of simulated LMXBs using the modified Skumanich

prescription I was able to compare the results to the observed LMXBs seen in Tables 2.4 and 2.5. The key result from this work was that the commonly used magnetic braking prescription, the Skumanich prescription, cannot effectively reproduce the sample of observed LMXBs. I found that using the default prescription, there were systematic mismatches between simulated and observed mass transfer rates up an order of magnitude. When the effects of isothermal winds or convective turnover times were accounted for in the magnetic braking scheme, the mass transfer rates began to approach the observed values and the simulated results more effectively reproduced the observed LMXBs. These results clearly showed that additional physics should be accounted for when determining the angular momentum loss due to magnetic braking in LMXBs.

## 5.2 CARB Magnetic Braking

The most effective form of the boosted Skumanich prescription was the “intermediate” case which used an ad-hoc wind and convection boosting. In Chapters 3 and 4, I derived an improved magnetic braking prescription that explicitly accounts for these effects. Using improvements in determining the effects of stellar rotation on the Alfvèn radius and linking the convective turnover time to the strength of the surface magnetic field I derived an improved magnetic braking scheme. This magnetic braking scheme which I called CARB magnetic braking, was used in numerical simulations to produce a grid of simulated results. This grid was compared to observed persistent LMXBs and was able to effectively reproduce the sample of systems. Additionally, I also showed that the effects of mass transfer efficiency must be included in these simulations otherwise an over-abundance of NSs with  $M \geq 2.0M_{\odot}$  will be produced.

Using the CARB magnetic braking scheme I conducted a rigorous parameter space search and inferred possible progenitor conditions. The simulated results showed that the progenitors of observed persistent LMXBs span a small part of

our plausible progenitor space. By using the amount of time a given simulated spends appearing similar to an observed LMXB I was able to calculate the minimum and average formation rates. The calculated minimum formation rate per Gyr in the Milky Way to reproduce the sample of observed LMXBs is about 2500 systems per Gyr with the progenitors of Cyg X-2 dominating this value with a calculated rate of 1200 systems per Gyr.

Another key result in our progenitor search for observed LMXBs was the gaps in our parameter space that resulted in no observed systems. The main points of interest were the gaps between the viable progenitors in regions “B”, “C” and “D” in Figure 4.9. These regions are found between progenitors of well studied, observed LMXBs which implied one of two possibilities, either that these systems are difficult to produce and no observable LMXBs from these regions exist, or these systems exist and have not been observed. Table 4.6 gave examples of LMXBs with properties that match with the simulated systems produced from these gaps in our progenitor space but at the time of writing, the mass ratio of these LMXBs had not been determined making it impossible to confirm if these observed binaries match with simulations.

### 5.3 Future Work

With the CARB magnetic braking derived, tested and confirmed to effectively reproduce the sample of observed persistent LMXBs, expanding the LMXBs tested would be the clear next step. Whether this is in testing transient binaries or moving towards black hole LMXBs, both systems are an additional opportunity to test the effectiveness of the prescription. A table showing a set of well studied BH LMXBs is shown in Appendix C.1. In the near future when the Gaia binary catalogue is released with data release 3 (Gaia Collaboration et al., 2020), there will be an abundance of well studied LMXBs. This deluge of systems will require well constructed pipelines and tools to explore the

data set. Applying the CARB magnetic braking scheme to this dataset would help both in testing the prescription and in better refining the progenitor rate value. Currently, a major limiting case is the number of observed LMXBs being compared, as this number increases, the effectiveness of the progenitor rate calculation improves. Beyond theory, we have provided three LMXBs with properties that are candidates for the parameter space gaps. Follow-up observations of these binaries to determine the mass ratios of these systems would help populate the progenitor parameter space.

# Appendix A

## Custom MESA Routines

In the appendix I include the changes I made to `MESA` to include the additional physics in my research. To use these changes or additions, the user must make changes to the appropriate subroutine in `run_binary_extras.f` and properly point to these subroutines within the simulation. These changes were applied to `MESA` versions 10398 and 11701, but should be applicable to other versions of `MESA` as well. With continuous development of the `MESA` code, some variable names may change from one version to another but the overall physics should be applicable.

### A.1 Implementation of Eddington Limit

```
1 subroutine mdot_edd_routine(binary_id, mdot_edd, ierr)
2     use const_def, only: dp
3     integer, intent(in) :: binary_id
4     real(dp), intent(out) :: mdot_edd
5     integer, intent(out) :: ierr
6     type (binary_info), pointer :: b
7     ierr = 0
8     call binary_ptr(binary_id, b, ierr)
9     if (ierr /= 0) then
10        write(*,*) 'failed in binary_ptr'
```

```

11         return
12     end if
13
14     ! changing mdot_edd from default MESA from BH to NS
15     ! x_ctrl(5) is the radius of the NS
16
17     ! mdot_edd = 4*pi*cight*b% s1% x_ctrl(5)/&
18     !           (0.2*(1+b% s1% surface_h1))
19     ! hard coding in the radius of 11.5km into the
20     ! equation results in the next line.
21     mdot_edd = 2.1666d18 / (1.d0 + b% s1% surface_h1)
22 end subroutine mdot_edd_routine

```

## A.2 Boosted Skumanich Magnetic Braking

```

1 subroutine jdotted_mb_routine(binary_id, ierr)
2     integer, intent(in) :: binary_id
3     integer, intent(out) :: ierr
4     integer :: k, nz
5     type (binary_info), pointer :: b
6     type (star_info), pointer :: s
7     real(dp) :: turnover_time, envelope_edge
8     real(dp) :: dr, tot_r, mb, jdotted_mb
9     real(dp) :: eta, wind_fac, saturate_fac
10    real(dp) :: tt_boost, wind_boost
11    real(dp) :: vel_ratio, tau_lim
12    real(dp) :: rsun4, two_pi_div_p3, rad4
13    ierr = 0
14    call binary_ptr(binary_id, b, ierr)
15    if (ierr /= 0) then
16        write(*,*) 'failed in binary_ptr'
17        return
18    end if

```

```

19
20     s => b% s_donor
21     nz = s% nz
22     eta = s% x_ctrl(1)
23     wind_fac = s% x_ctrl(2)
24     vel_ratio = s% x_ctrl(3)
25     tau_lim = s% x_ctrl(4)
26     saturate_fac = s% x_ctrl(5)
27
28     tot_r = 0.0
29     turnover_time = 0.0
30     envelope_edge = 0.0
31     envelope_edge = max( s% conv_mx1_bot_r , s% conv_mx2_bot_r )
32
33     do k = nz, 1, -1
34         if (s% mixing_type(k) == convective_mixing) then
35             if ( s% r(k) .gt. envelope_edge) then
36                 if (k < s% nz) then
37                     dr = (s% r(k) - s% r(k + 1))
38                 else
39                     dr = (s% r(k) - s% R_center)
40                 end if
41                 if (s% conv_vel(k) .gt. vel_ratio * s% csound(k)
42                     .and. s% tau(k) .gt. tau_lim) then
43                     turnover_time = turnover_time + (dr/s% conv_vel(k))
44                     tot_r = tot_r + dr
45                 end if
46             else
47                 turnover_time = turnover_time
48                 tot_r = tot_r + dr
49             end if
50         end if
51     end do
52
53     ! b% jdot_mb = 0

```

```

54    rsun4 = rsun*rsun*rsun*rsun
55    two_pi_div_p3 = (2.0*pi/b% period)*(2.0*pi/b% period)*&
56                                (2.0*pi/b% period)
57
58    mb = -3.8d-30*b% m(b% d_i)*rsun4* &
59        pow_cr(min(b% r(b% d_i),b% rl(b% d_i))/rsun ,
60        b% magnetic_braking_gamma)* &
61        two_pi_div_p3
62
63    ! use the formula from rappaport , verbunt , and joss .
64    ! apj , 275 , 713–731. 1983.
65    if (b% have_radiative_core(b% d_i) .or. b% keep_mb_on) &
66
67        ! 2.8d6 is turnover time in seconds for a MESA
68        ! model using initial mass of 1.0 solar masses ,
69        ! solar metalicity , at age 4.6 Gyr. This is
70        ! approximately turnover time of the Sun.
71
72    wind_boost = (b% mdot_system_wind(b% d_i) / (-1.6d12)) ** wind_fac
73    tt_boost = (turnover_time / 2.8d6 ) ** eta
74
75    jdot_mb = (wind_boost) * (tt_boost) * mb
76
77    ! taking the period of the sun to be 24 days
78    ! => 10 * P < Psun , P < 2.4 days
79    ! 2.4 days = 207360 seconds
80    if (b% period < 207360) then
81
82        ! use the formula from Ivanova & Taam 2003 for quickly rotating stars
83        rad4 = b% r(b% d_i) * b% r(b% d_i) * b% r(b% d_i) * b% r(b% d_i)
84        b% jdot_mb = (-6.0d30 * rad4 / rsun4) * 10 ** (1.7) * &
85                                (2073600 / b% period) ** saturate_fac) * &
86                                tt_boost * wind_boost
87    else
88        b% jdot_mb = jdot_mb

```

```

89     end if
90
91     if (b% evolve_both_stars .and. b% include_accretor_mb .and. &
92         (b% have_radiative_core(b% a_i) .or. b% keep_mb_on)) then
93         b% jdot_mb = b% jdot_mb - &
94             3.8d-30*b% m(b% a_i)*rsun4* &
95             pow_cr(min(b% r(b% a_i),b% rl(b% a_i))/rsun,
96             b% magnetic_braking_gamma)* &
97             two_pi_div_p3
98     end if
99 end subroutine jdot_mb_routine

```

### A.3 CARB Magnetic Braking

```

1
2 subroutine jdot_mb_routine(binary_id, ierr)
3     integer, intent(in) :: binary_id
4     integer, intent(out) :: ierr
5     integer :: k, nz
6     type (binary_info), pointer :: b
7     type (star_info), pointer :: s
8     real(dp) :: turnover_time, tt_temp, tt_temp_scaled
9     real(dp) :: tt_old, tt_diff
10    real(dp) :: vel, vel_ratio, vel_diff
11    real(dp) :: upper_lim, lower_lim, scaled_vel
12    real(dp) :: eps_nuc_lim, eps_nuc
13    real(dp) :: dr, tau_lim, delta_mag_chk
14    real(dp) :: rsun4, two_pi_div_p3, two_pi_div_p2, K2
15    real(dp) :: tt_ratio, tt4
16    real(dp) :: rot_ratio, rot4
17    real(dp) :: rad4
18    real(dp) :: v_esc2, v_mod2
19    real(dp) :: alfvén_no_R, R_alfven

```

```

20     real(dp) :: jdot_mb_old , jdot_mb_new
21     real(dp) :: conv_env_r , conv_env_m , sonic_cross_time , mag_field
22     common/ old_var/ tt_old
23     logical :: conv_env_found
24     ierr = 0
25     call binary_ptr(binary_id , b , ierr)
26     if ( ierr .ne. 0) then
27       write(*,*) 'failed in binary_ptr'
28       return
29     end if
30
31     ! write (*,*) " "
32     ! write (*,*) "===== "
33     ! write (*,*) 'doing jdot'
34     ! write (*,*) "===== "
35     ! write (*,*) " "
36
37 ! INITIALIZE THE VARIABLES
38
39     s => b% s_donor
40     nz = s% nz
41     vel_ratio = s% x_ctrl(1)
42     tau_lim = s% x_ctrl(2)
43
44     conv_env_found = .false.
45
46     turnover_time = 0.0
47     tt_temp = 0.0
48     tt_temp_scaled = 0.0
49
50     eps_nuc_lim = 1.0d-2
51     vel_diff = 0.0
52     scaled_vel = 0.0
53
54 ! INITIAL TURNOVER TIME CALCULATION

```

```

55      ! beginning of do loop to calculate convective turnover time
56      do k = nz, 1, -1
57
58      eps_nuc = s% eps_nuc(k)
59      ! check if the cell we are looping through
60      ! satisfies our convection criteria
61      if ((s% gradr(k) .gt. s% grada(k)) .and.
62          (eps_nuc .lt. eps_nuc_lim)) then
63          ! toggle the boolean to begin integration
64          conv_env_found = .true.
65      end if
66
67      ! only enter this portion if the convective boolean is true
68      ! this loop will go from the innermost cell that is convective to
69      ! the surface. This is to try and smooth through any numeric issues
70      ! with convective zones appearing and disappearing in MESA.
71      if (conv_env_found) then
72
73          ! loop to calculate the size of the cell, the innermost cell
74          ! needs special consideration as it is above the core
75          if (k .lt. s% nz) then
76              dr = (s% r(k) - s% r(k + 1))
77          else
78              dr = (s% r(k) - s% R_center)
79          end if
80
81          ! determine the convective velocity inside each given cell
82          if (s% mixing_type(k) == convective_mixing) then
83
84              ! need to ensure that the convective velocity is within
85              ! our defined limits, if they are outside of these limits
86              ! set them to be the max/min value allowed.
87              vel = s% conv_vel(k)
88              lower_lim = vel_ratio * s% csound(k)
89              upper_lim = 1.0 * s% csound(k)

```

```

90
91         if (vel .lt. lower_lim) then
92             vel = lower_lim
93         else if (vel .gt. upper_lim) then
94             vel = upper_lim
95         end if
96
97         ! if the cell isn't defined by MESA to be convective take the
98         ! convective velocity to be equal to sound speed
99     else
100        vel = s% csound(k)
101    end if
102
103    ! Final check involving the opacity of the given cell. If the
104    ! cell isn't near the surface (low tau) then include it in our
105    ! integration
106    if (s% tau(k) .gt. tau_lim) then
107        sonic_cross_time = sonic_cross_time + (dr / s% csound(k))
108        conv_env_r = conv_env_r + dr
109        conv_env_m = conv_env_m + s% dm(k)
110        tt_temp = tt_temp + (dr / vel)
111    end if
112    end if
113
114 end do ! end of do loop to calculate convective turnover time
115
116 ! reset the boolean just in case
117 conv_env_found = .false.
118
119 ! TURNOVER TIME CHECK, THIS IS TO TRY AND AVOID LARGE CHANGES
120
121 ! simply set the turnover time to the internal variable calculated above
122 turnover_time = tt_temp
123
124 if (s% model_number .gt. 1) then

```

```

125      ! calculate the variables used to check if our system is rapidly
126      ! evolving
127      tt_diff = abs(tt_old - tt_temp) / tt_old
128      delta_mag_chk = s% dt / tt_old
129
130      ! write (*,*) "tt_diff = ", tt_diff
131      ! write (*,*) "delta_mag = ", delta_mag_chk
132      ! write (*,*) "turnover_time = ", turnover_time
133      ! write (*,*) "tt_old = ", tt_old
134
135      ! check if timesteps are very small or if the relative
136      ! change is very large
137      if (tt_diff .gt. delta_mag_chk) then
138          write (*,*) "large change, adjusting accordingly"
139          turnover_time = tt_old + (tt_temp - tt_old) &
140                          * min((s% dt / tt_old), 0.5)
141          mag_field = (turnover_time / 2.8d6) * (2073600. / b% period)
142
143      end if ! end of timestep/relative change check
144  end if
145
146      ! remember the current values to be used as comparison in the next step
147
148      tt_old = turnover_time
149
150 ! MAGNETIC BRAKING CALCULATION
151
152      b% jdot_mb = 0
153      rsun4 = pow4(rsun)
154
155      call check_radiative_core(b)
156
157      two_pi_div_p3 = (2.0*pi/b% period)*(2.0*pi/b% period)*(2.0*pi/b% period)
158      two_pi_div_p2 = (2.0*pi/b% period)*(2.0*pi/b% period)
159

```

```

160      K2 = 0.07 * 0.07
161
162      ! use the formula from rappaport , verbunt , and joss .
163      ! apj , 275 , 713–731. 1983.
164      if (b% have_radiative_core(b% d_i) .or. b% keep_mb_on) then
165
166          jdot_mb_old = -3.8d-30*b% m(b% d_i)*rsun4* &
167              pow_cr(min(b% r(b% d_i) , b% rl(b% d_i)) &
168                  /rsun ,b% magnetic_braking_gamma)* &
169                  two_pi_div_p3
170
171          tt_ratio = turnover_time / 2.8d6
172          tt4 = pow4(tt_ratio)
173          ! write (*,*) "tt4 = ", tt4
174
175          rot_ratio = (2073600. / b% period )
176          rot4 = pow4(rot_ratio)
177          ! write (*,*) "rot4 = ", rot4
178
179          rad4 = pow4(b% r(b% d_i))
180          ! write (*,*) "rad4 = ", rad4
181
182          v_esc2 = 2.0 * standard_cgrav * b% m(b% d_i) / b% r(b% d_i)
183          v_mod2 = v_esc2 + 2.0 * two_pi_div_p2 * b% r(b% d_i) *&
184              b% r(b% d_i) / K2
185          ! write (*,*) "G = ", standard_cgrav
186          ! write (*,*) "M = ", b% m(b% d_i)
187          ! write (*,*) "R = ", b% r(b% d_i)
188          ! write (*,*) "v_esc2 = ", v_esc2
189          ! write (*,*) "v_mod2 = ", v_mod2
190
191          alfven_no_R = rad4 * rot4 * tt4 / (b% mdot_system_wind(b% d_i) *&
192              b% mdot_system_wind(b% d_i)) * (1.0 / v_mod2)
193
194          R_alfven = b% r(b% d_i) * alfven_no_R **(1.d0/3.d0)

```

```

195
196     jdot_mb_new = (2.0/3.0) * (2.0*pi/b% period) * &
197             b% mdot_system_wind(b% d_i) * R_alfven * R_alfven
198     ! write (*,*) "jdot_mb_new = ", jdot_mb_new
199     ! write (*,*) "jdot_mb_old = ", jdot_mb_old
200
201     b% jdot_mb = jdot_mb_new
202
203 end if
204
205 if (b% point_mass_i == 0 .and. b% include_accretor_mb .and. &
206     (b% have_radiative_core(b% a_i) .or. b% keep_mb_on)) then
207     b% jdot_mb = b% jdot_mb - &
208             3.8d-30*b% m(b% a_i)*rsun4* &
209             pow_cr(min(b% r(b% a_i),b% rl(b% a_i))/&
210             rsun,b% magnetic_braking_gamma)* &
211             two_pi_div_p3
212 end if
213
214 s% xtra1 = turnover_time
215 s% xtra2 = mag_field
216 s% xtra3 = conv_env_r
217 s% xtra4 = conv_env_m
218 s% xtra5 = sonic_cross_time
219
220 end subroutine jdot_mb_routine

```

# Appendix B

## Sample MESA `inlist` Files

Simulations within MESA are run with `inlist` files, these files are read sequentially. If a variable is used multiple times, every subsequent use of the variable overwrites the previous input. The sample `inlist` files shown here are examples of uses from within the main body of the text. All parameters not listed in the sample `inlist` use the MESA default values.

### B.1 Boosted Skumanich Sample

```
1 &binary_job
2
3     inlist_names(1) = 'inlist1'
4
5     !which_for_pgstar = 0 ! 0 means none; < 0 means all; i > 0 means star
6     evolve_both_stars = .false.
7     warn_binary_extra = .false.
8
9
10 / ! end of binary_job namelist
11
12 &binary_controls
13     terminal_interval = 10
```

```

14     write_header_frequency = 5
15     initial_period_in_days = ! period
16
17     use_other_jdot_mb = .true.
18     use_other_mdot_edd = .true.
19     terminate_if_initial_overflow = .false.
20     limit_retention_by_mdot_edd = .true.
21     use_es_opacity_for_mdot_edd = .true.
22
23     max_explicit_abs_mdot = 1d100
24     fm = 0.01d0
25     fa = 0.01d0
26     fr = 0.10d0
27     fj = 0.001d0
28
29     m1 = ! donor mass
30     m2 = 1.4
31     max_tries_to_achieve = 50
32     magnetic_braking_gamma = 4.0
33
34 / ! end of binary_controls namelist

```

```

1 &star_job
2
3 ! start a run from a saved model
4 load_saved_model = .false.
5
6 ! setting intial model number
7 set_initial_model_number = .true.
8 initial_model_number = 0
9
10 ! setting initial age
11 set_initial_age = .false.
12

```

```

13 ! set_initial_dt = .true.
14 ! years_for_initial_dt = 1d5
15
16 change_v_flag = .true.
17 new_v_flag = .true.
18
19 ! change_rotation_flag = .true.
20 ! new_rotation_flag = .true.
21
22 change_lnPgas_flag = .true.
23 new_lnPgas_flag = .true.
24 warn_run_star_extras = .false.
25
26
27 / !end of star_job namelist
28
29
30 &controls
31
32 x_ctrl(1) = ! velocity ratio
33 x_ctrl(2) = ! opacity limit
34 x_ctrl(3) = ! wind factor
35 x_ctrl(4) = ! turnover time factor
36 x_ctrl(5) = ! rotation factor
37 x_ctrl(6) = ! saturation factor
38
39 terminal_interval = 10
40 write_header_frequency = 5
41
42 ! maximum number of profiles
43 max_num_profile_models = -1
44
45 ! profile intervals
46 profile_interval = 10000
47

```

```

48     history_interval = 1
49
50     hot_wind_scheme = 'Reimers'
51     cool_wind_RGB_scheme = 'Reimers'
52     Reimers_scaling_factor = 1.0
53     smooth_convective_bdy = .true.
54     alt_scale_height_flag = .true.
55     min_dxm_Eulerian_div_dxm_removed = -1
56     mass_change_full_on_dt = 1d-99
57     mass_change_full_off_dt = 1d-99
58     wind_boost_full_off_L_div_Ledd = 1d99
59     wind_boost_full_on_L_div_Ledd = 1d99
60
61     max_age = 1d10
62
63 /! end of controls namelist

```

## B.2 CARB MB Sample

```

1 &binary_job
2
3     inlist_names(1) = 'inlist1'
4
5     evolve_both_stars = .false.
6     warn_binary_extra = .false.
7
8 / ! end of binary_job namelist
9
10 &binary_controls
11     terminal_interval = 10
12     write_header_frequency = 5
13     initial_period_in_days = ! initial period
14

```

```

15   use_other_jdot_mb = .true.
16   use_other_mdot_edd = .true.
17   terminate_if_initial_overflow = .false.
18   limit_retention_by_mdot_edd = .true.
19   use_es_opacity_for_mdot_edd = .true.

20
21   max_explicit_abs_mdot = 1d100
22   fm = 0.01d0
23   fa = 0.01d0
24   fr = 0.10d0
25   fj = 0.001d0
26   mass_transfer_beta = 0.8d0

27
28   m1 = ! initial donor mass
29   m2 = 1.4
30   max_tries_to_achieve = 50
31   cur_mdot_frac = 0.5
32   magnetic_braking_gamma = 4.0

33
34 / ! end of binary_controls namelist

```

```

1 &star_job
2
3 ! setting intial model number
4 set_initial_model_number = .true.
5 initial_model_number = 0
6
7 ! setting initial age
8 set_initial_age = .false.

9
10
11 change_v_flag = .true.
12 new_v_flag = .true.

13

```

```

14 change_lnPgas_flag = .true.
15 new_lnPgas_flag = .true.
16 warn_run_star_extras = .false.
17
18
19 / !end of star_job namelist
20
21
22 &controls
23
24 x_ctrl(1) = ! velocity ratio
25 x_ctrl(2) = ! tau limit
26
27 terminal_interval = 20
28 write_header_frequency = 10
29
30 ! maximum number of profiles
31 max_num_profile_models = -1
32
33 ! profile intervals
34 profile_interval = 10000
35 history_interval = 1
36
37 hot_wind_scheme = 'Reimers'
38 cool_wind_RGB_scheme = 'Reimers'
39 Reimers_scaling_factor = 1.0
40 smooth_convective_bdy = .true.
41 alt_scale_height_flag = .true.
42 min_dxm_Eulerian_div_dxm_removed = -1
43 mass_change_full_on_dt = 1d-99
44 mass_change_full_off_dt = 1d-99
45 wind_boost_full_off_L_div_Ledd = 1d99
46 wind_boost_full_on_L_div_Ledd = 1d99
47
48 use_dedt_form_of_energy_eqn = .true.

```

```
49      use_gold tolerances = .true.  
50  
51  
52 ! when to stop  
53   max_age = 1d10  
54  
55 /! end of controls namelist
```

# Appendix C

## Black Hole Table

The methods and techniques used in this thesis to study NS LMXBs can be extended to study black hole (BH) LMXBs as well. Below is a preliminary table of well studied BH LMXBs. Extending this research to study BH LMXBs requires varying the accretor mass as well as the donor mass increasing the size of the parameter space.

Source	Flags	$M_d$	Mass Ratio	Period	Average Mass Transfer
		( $M_\odot$ )	( $M_d/M_a$ )	(Hours)	( $M_\odot \text{ yr}^{-1}$ )
MAXI J1659-152	T	—	—	2.414	$3.54 \times 10^{-10}$
SWIFT J1357.2-0933	T	—	—	2.8	$3.56 \times 10^{-11}$
SWIFT J1753.5-0127	Per	—	—	3.2	$2.38 \times 10^{-09}$
XTE J1118+480	T	7.3	0.024	4.1	$7.90 \times 10^{-12}$
4U 2030+40	Per	2.4	0.23	4.8	$3.64 \times 10^{-08}$
MAXI J1836-194	T	—	—	4.9	$1.04 \times 10^{-09}$
XTE J1859+226	T	10.83	0.25	6.6	$7.52 \times 10^{-10}$
XTE J1650-500	T	4.72	0.25	7.7	$5.56 \times 10^{-11}$
4U 1957+115	Per	—	—	9.33	$2.84 \times 10^{-09}$
MAXI J1305-704	T	—	—	9.74	$6.54 \times 10^{-10}$
SWIFT J174510.8-262411	T	—	—	21	$3.13 \times 10^{-10}$
4U 1543-475	T	9.4	0.28	26.8	$7.67 \times 10^{-10}$
XTE J1550-564	T	10.39	0.034	37	$2.12 \times 10^{-09}$
4U 0538-641	Per	6.95	0.532	40.9	$2.00 \times 10^{-07}$
GX 339-4	T	—	—	42.1	$1.55 \times 10^{-08}$
GS 1354-64	T	7.47	0.12	61.1	$6.64 \times 10^{-09}$
GRO J1655-40	T	5.4	0.38	62.9	$2.86 \times 10^{-09}$
SAX J1819.3-2525	T	6.4	0.45	67.6	$2.31 \times 10^{-09}$
4U 0540-697	Per	10.91	0.343	93.8	$2.29 \times 10^{-07}$

4U 1956+350	Per	12.4	1.294	134.3	$3.88 \times 10^{-09}$
1E 1740.7-2942	Per	—	—	305.52	$9.81 \times 10^{-09}$
GRS 1915+105	Per	12.4	0.058	314.4	$1.59 \times 10^{-07}$
GRS 1758-258	Per	—	—	442.8	$1.13 \times 10^{-08}$
XTE J0421+560	T	—	—	465.84	$4.55 \times 10^{-11}$

Table C.1: A similar table to Table 2.3 showing BH LMXBs. Unlike the NS LMXBs which were aggregated from different sources, all of the observed BH LMXBs in this table are taken from Tetarenko et al. (2016)

# Bibliography

- H. A. Abt. Normal and abnormal binary frequencies. ARA&A, 21:343–372, January 1983. doi: 10.1146/annurev.aa.21.090183.002015.
- H. A. Abt and S. G. Levy. Multiplicity among solar-type stars. ApJS, 30: 273–306, March 1976. doi: 10.1086/190363.
- V. K. Agrawal and R. Misra. X-ray spectral evolution of the extragalactic Z source LMC X-2. MNRAS, 398:1352–1360, September 2009. doi: 10.1111/j.1365-2966.2009.15014.x.
- A. Alastuey and B. Jancovici. Nuclear reaction rate enhancement in dense stellar matter. ApJ, 226:1034–1040, December 1978. doi: 10.1086/156681.
- L. A. Almeida, H. Sana, W. Taylor, R. Barbá, A. Z. Bonanos, P. Crowther, A. Damineli, A. de Koter, S. E. de Mink, C. J. Evans, M. Gieles, N. J. Grin, V. Hénault-Brunet, N. Langer, D. Lennon, S. Lockwood, J. Maíz Apellániz, A. F. J. Moffat, C. Neijssel, C. Norman, O. H. Ramírez-Agudelo, N. D. Richardson, A. Schootemeijer, T. Shenar, I. Soszyński, F. Tramper, and J. S. Vink. The Tarantula Massive Binary Monitoring. I. Observational campaign and OB-type spectroscopic binaries. A&A, 598:A84, February 2017. doi: 10.1051/0004-6361/201629844.
- D. Altamirano, A. Patruno, C. O. Heinke, C. Markwardt, T. E. Strohmayer, M. Linares, R. Wijnands, M. van der Klis, and J. H. Swank. Discovery of a

205.89 Hz Accreting Millisecond X-ray Pulsar in the Globular Cluster NGC 6440. ApJ, 712:L58–L62, March 2010. doi: 10.1088/2041-8205/712/1/L58.

C. Angulo, M. Arnould, M. Rayet, P. Descouvemont, D. Baye, C. Leclercq-Willain, A. Coc, S. Barhoumi, P. Aguer, C. Rolfs, R. Kunz, J. W. Hammer, A. Mayer, T. Paradellis, S. Kossionides, C. Chronidou, K. Spyrou, S. degl’Innocenti, G. Fiorentini, B. Ricci, S. Zavatarelli, C. Providencia, H. Wolters, J. Soares, C. Grama, J. Rahighi, A. Shotter, and M. Lamehi Rachti. A compilation of charged-particle induced thermonuclear reaction rates. Nuclear Physics A, 656:3–183, August 1999. doi: 10.1016/S0375-9474(99)00030-5.

J. Antoniadis, M. H. van Kerkwijk, D. Koester, P. C. C. Freire, N. Wex, T. M. Tauris, M. Kramer, and C. G. Bassa. The relativistic pulsar-white dwarf binary PSR J1738+0333 - I. Mass determination and evolutionary history. MNRAS, 423(4):3316–3327, Jul 2012. doi: 10.1111/j.1365-2966.2012.21124.x.

J. Antoniadis, P. C. C. Freire, N. Wex, T. M. Tauris, R. S. Lynch, M. H. van Kerkwijk, M. Kramer, C. Bassa, V. S. Dhillon, T. Driebe, J. W. T. Hessels, V. M. Kaspi, V. I. Kondratiev, N. Langer, T. R. Marsh, M. A. McLaughlin, T. T. Pennucci, S. M. Ransom, I. H. Stairs, J. van Leeuwen, J. P. W. Verbiest, and D. G. Whelan. A Massive Pulsar in a Compact Relativistic Binary. Science, 340:448, April 2013. doi: 10.1126/science.1233232.

John Antoniadis, Thomas M. Tauris, Feryal Ozel, Ewan Barr, David J. Champion, and Paulo C. C. Freire. The millisecond pulsar mass distribution: Evidence for bimodality and constraints on the maximum neutron star mass. arXiv e-prints, art. arXiv:1605.01665, May 2016.

A. M. Archibald, I. H. Stairs, S. M. Ransom, V. M. Kaspi, V. I. Kondratiev, D. R. Lorimer, M. A. McLaughlin, J. Boyles, J. W. T. Hessels, R. Lynch,

J. van Leeuwen, M. S. E. Roberts, F. Jenet, D. J. Champion, R. Rosen, B. N. Barlow, B. H. Dunlap, and R. A. Remillard. A Radio Pulsar/X-ray Binary Link. Science, 324:1411, June 2009. doi: 10.1126/science.1172740.

M. Aurière, R. Konstantinova-Antova, C. Charbonnel, G. A. Wade, S. Tsvetkova, P. Petit, B. Dintrans, N. A. Drake, T. Decressin, N. Lagarde, J. F. Donati, T. Roudier, F. Lignières, K. P. Schröder, J. D. Landstreet, A. Lèbre, W. W. Weiss, and J. P. Zahn. The magnetic fields at the surface of active single G-K giants. A&A, 574:A90, February 2015. doi: 10.1051/0004-6361/201424579.

M. Bachetti, F. A. Harrison, D. J. Walton, B. W. Grefenstette, D. Chakrabarty, F. Fürst, D. Barret, A. Beloborodov, S. E. Boggs, F. E. Christensen, W. W. Craig, A. C. Fabian, C. J. Hailey, A. Hornschemeier, V. Kaspi, S. R. Kulkarni, T. Maccarone, J. M. Miller, V. Rana, D. Stern, S. P. Tendulkar, J. Tomsick, N. A. Webb, and W. W. Zhang. An ultraluminous X-ray source powered by an accreting neutron star. Nature, 514(7521):202–204, October 2014. doi: 10.1038/nature13791.

M. C. Baglio, P. D’Avanzo, T. Muñoz-Darias, R. P. Breton, and S. Campana. The long-term evolution of the X-ray pulsar XTE J1814-338: A receding jet contribution to the quiescent optical emission? A&A, 559:A42, November 2013. doi: 10.1051/0004-6361/201322442.

A.-S. Bak Nielsen, A. Patruno, and C. D’Angelo. The X-ray pulsar 2A 1822-371 as a super-Eddington source. MNRAS, 468:824–834, June 2017. doi: 10.1093/mnras/stx491.

Ş. Balman. A Study of the Low-Mass X-Ray Binary Dip Sources XB 1916 - 053, XB 1323 - 619, X 1624 - 490 and 4U 1746 - 371 Observed with INTEGRAL. AJ, 138:50–62, July 2009. doi: 10.1088/0004-6256/138/1/50.

M. Bałucińska-Church, M. J. Church, and A. P. Smale. The orbital period of the dipping, bursting, globular cluster X-ray source XB 1746-371 from Rossi X-ray Timing Explorer observations. MNRAS, 347:334–338, January 2004. doi: 10.1111/j.1365-2966.2004.07218.x.

A. J. Bayless, E. L. Robinson, R. I. Hynes, T. A. Ashcraft, and M. E. Cornell. The Structure of the Accretion Disk in the Accretion Disk Corona X-ray Binary 4U 1822-371 at Optical and Ultraviolet Wavelengths. ApJ, 709:251–262, January 2010. doi: 10.1088/0004-637X/709/1/251.

K. Belczynski, A. Askar, M. Arca-Sedda, M. Chruslinska, M. Donnari, M. Giersz, M. Benacquista, R. Spurzem, D. Jin, G. Wiktorowicz, and D. Beltoni. The origin of the first neutron star - neutron star merger. A&A, 615: A91, July 2018. doi: 10.1051/0004-6361/201732428.

K. Belczynski, J. Klencki, C. E. Fields, A. Olejak, E. Berti, G. Meynet, C. L. Fryer, D. E. Holz, R. O’Shaughnessy, D. A. Brown, T. Bulik, S. C. Leung, K. Nomoto, P. Madau, R. Hirschi, E. Kaiser, S. Jones, S. Mondal, M. Chruslinska, P. Drozda, D. Gerosa, Z. Doctor, M. Giersz, S. Ekstrom, C. Georgy, A. Askar, V. Baibhav, D. Wysocki, T. Natan, W. M. Farr, G. Wiktorowicz, M. Coleman Miller, B. Farr, and J. P. Lasota. Evolutionary roads leading to low effective spins, high black hole masses, and O1/O2 rates for LIGO/Virgo binary black holes. A&A, 636:A104, April 2020. doi: 10.1051/0004-6361/201936528.

D. Bhattacharya and E. P. J. van den Heuvel. Formation and evolution of binary and millisecond radio pulsars. Phys. Rep., 203:1–124, January 1991. doi: 10.1016/0370-1573(91)90064-S.

Sudip Bhattacharyya, Tod E. Strohmayer, Craig B. Markwardt, and Jean H. Swank. The Discovery of a Neutron Star with a Spin Frequency of 530 Hz in A1744-361. ApJ, 639:L31–L34, March 2006. doi: 10.1086/501438.

Lars Bildsten and Christopher J. Deloye. Ultracompact Binaries as Bright X-Ray Sources in Elliptical Galaxies. ApJ, 607(2):L119–L122, June 2004. doi: 10.1086/421844.

G. Bruzual and S. Charlot. Stellar population synthesis at the resolution of 2003. MNRAS, 344(4):1000–1028, October 2003. doi: 10.1046/j.1365-8711.2003.06897.x.

J. R. Buchler and W. R. Yueh. Compton scattering opacities in a partially degenerate electron plasma at high temperatures. ApJ, 210:440–446, December 1976. doi: 10.1086/154847.

P. Bult, A. Patruno, and M. van der Klis. Coherent Timing of the Accreting Millisecond Pulsar NGC 6440 X-2. ApJ, 814:138, December 2015. doi: 10.1088/0004-637X/814/2/138.

A. Büning and H. Ritter. Long-term evolution of compact binaries with irradiation feedback. A&A, 423:281–299, August 2004. doi: 10.1051/0004-6361:20035678.

L. Burderi, F. D’Antona, and M. Burgay. PSR J1740-5340: Accretion Inhibited by Radio Ejection in a Binary Millisecond Pulsar in the Globular Cluster NGC 6397. ApJ, 574:325–331, July 2002. doi: 10.1086/340891.

L. Burderi, T. Di Salvo, F. D’Antona, N. R. Robba, and V. Testa. The optical counterpart to SAX J1808.4-3658 in quiescence: Evidence of an active radio pulsar? A&A, 404:L43–L46, June 2003. doi: 10.1051/0004-6361:20030669.

B. W. Carroll and D. A. Ostlie. An introduction to modern astrophysics and cosmology. July 2006.

J. Casares, G. Dubus, T. Shahbaz, C. Zurita, and P. A. Charles. VLT spectroscopy of XTE J2123-058 during quiescence: the masses of the two com-

ponents. *MNRAS*, 329:29–36, January 2002. doi: 10.1046/j.1365-8711.2002.04964.x.

J. Casares, R. Cornelisse, D. Steeghs, P. A. Charles, R. I. Hynes, K. O’Brien, and T. E. Strohmayer. Detection of the irradiated donor in the LMXBs 4U 1636-536 (=V801 Ara) and 4U 1735-444 (=V926 Sco). *MNRAS*, 373: 1235–1244, December 2006. doi: 10.1111/j.1365-2966.2006.11106.x.

S. Cassisi, A. Y. Potekhin, A. Pietrinferni, M. Catelan, and M. Salaris. Updated Electron-Conduction Opacities: The Impact on Low-Mass Stellar Models. *ApJ*, 661:1094–1104, June 2007. doi: 10.1086/516819.

D. Chakrabarty and E. H. Morgan. The two-hour orbit of a binary millisecond X-ray pulsar. *Nature*, 394:346–348, July 1998. doi: 10.1038/28561.

Deepto Chakrabarty. High-Speed Optical Photometry of the Ultracompact X-Ray Binary 4U 1626-67. *ApJ*, 492:342–351, January 1998. doi: 10.1086/305035.

P. A. Charles, D. C. Jones, and T. Naylor. An emission-line object in the core of M15. *Nature*, 323:417–419, October 1986. doi: 10.1038/323417a0.

Wen-Cong Chen. Formation of Scorpius X-1 induced by anomalous magnetic braking of Ap/Bp stars. *A&A*, 606:A60, October 2017. doi: 10.1051/0004-6361/201630239.

R. Chini, V. H. Hoffmeister, A. Nasseri, O. Stahl, and H. Zinnecker. A spectroscopic survey on the multiplicity of high-mass stars. *MNRAS*, 424(3): 1925–1929, August 2012. doi: 10.1111/j.1365-2966.2012.21317.x.

D. J. Christian and J. H. Swank. The Survey of Low-Mass X-Ray Binaries with the Einstein Observatory Solid-State Spectrometer and Monitor Proportional Counter. *ApJS*, 109:177–224, March 1997. doi: 10.1086/312970.

E. J. M. Colbert and R. F. Mushotzky. The Nature of Accreting Black Holes in Nearby Galaxy Nuclei. ApJ, 519:89–107, July 1999. doi: 10.1086/307356.

M. Coriat, R. P. Fender, and G. Dubus. Revisiting a fundamental test of the disc instability model for X-ray binaries. MNRAS, 424:1991–2001, August 2012. doi: 10.1111/j.1365-2966.2012.21339.x.

R. Cornelisse, M. M. Kotze, J. Casares, P. A. Charles, and P. J. Hakala. The origin of the tilted disc in the low-mass X-ray binary GR Mus (XB 1254-690). MNRAS, 436:910–920, November 2013. doi: 10.1093/mnras/stt1654.

T. J. L. Courvoisier, A. N. Parmar, A. Peacock, and M. Pakull. The Discovery of 3.9 Hour Periodic Dips in the X-Ray Intensity of XB 1254-690. ApJ, 309: 265, October 1986. doi: 10.1086/164598.

A. P. Cowley, D. Crampton, and J. B. Hutchings. The halo population X-ray source Cygnus X-2. ApJ, 231:539–550, Jul 1979. doi: 10.1086/157216.

J. P. Cox and R. T. Giuli. Principles of stellar structure . 1968.

H. T. Cromartie, E. Fonseca, S. M. Ransom, P. B. Demorest, Z. Arzoumanian, H. Blumer, P. R. Brook, M. E. DeCesar, T. Dolch, J. A. Ellis, R. D. Ferdman, E. C. Ferrara, N. Garver-Daniels, P. A. Gentile, M. L. Jones, M. T. Lam, D. R. Lorimer, R. S. Lynch, M. A. McLaughlin, C. Ng, D. J. Nice, T. T. Pennucci, R. Spiewak, I. H. Stairs, K. Stovall, J. K. Swiggum, and W. W. Zhu. Relativistic Shapiro delay measurements of an extremely massive millisecond pulsar. Nature Astronomy, page 439, Sep 2019. doi: 10.1038/s41550-019-0880-2.

R. H. Cyburt, A. M. Amthor, R. Ferguson, Z. Meisel, K. Smith, S. Warren, A. Heger, R. D. Hoffman, T. Rauscher, A. Sakharuk, H. Schatz, F. K. Thielemann, and M. Wiescher. The JINA REACLIB Database: Its Recent Up-

dates and Impact on Type-I X-ray Bursts. ApJS, 189:240–252, jul 2010. doi: 10.1088/0067-0049/189/1/240.

A. D’Aì, R. Iaria, T. Di Salvo, A. Riggio, L. Burderi, and N. R. Robba. Chandra X-ray spectroscopy of a clear dip in GX 13+1. A&A, 564:A62, April 2014. doi: 10.1051/0004-6361/201322044.

A. D’Aì, T. Di Salvo, R. Iaria, J. A. García, A. Sanna, F. Pintore, A. Riggio, L. Burderi, E. Bozzo, T. Dauser, M. Matranga, C. G. Galiano, and N. R. Robba. GRO J1744-28: an intermediate B-field pulsar in a low-mass X-ray binary. MNRAS, 449:4288–4303, June 2015. doi: 10.1093/mnras/stv531.

P. D’Avanzo, S. Campana, J. Casares, G. L. Israel, S. Covino, P. A. Charles, and L. Stella. Doppler tomography of the transient X-ray binary Centaurus X-4 in quiescence. A&A, 444:905–912, December 2005. doi: 10.1051/0004-6361:20053517.

V. De Falco, L. Kuiper, E. Bozzo, D. K. Galloway, J. Poutanen, C. Ferrigno, L. Stella, and M. Falanga. The 2015 outburst of the accretion-powered pulsar IGR J00291+5934: INTEGRAL and Swift observations. A&A, 599:A88, March 2017. doi: 10.1051/0004-6361/201629575.

N. Degenaar, J. M. Miller, F. A. Harrison, J. A. Kennea, C. Kouveliotou, and G. Younes. High-resolution X-Ray Spectroscopy of the Bursting Pulsar GRO J1744-28. ApJ, 796:L9, November 2014. doi: 10.1088/2041-8205/796/1/L9.

H. E. DeWitt, H. C. Grabske, and M. S. Cooper. Screening Factors for Nuclear Reactions. I. General Theory. ApJ, 181:439–456, April 1973. doi: 10.1086/152061.

A. Dieball, C. Knigge, D. R. Zurek, M. M. Shara, K. S. Long, P. A. Charles, D. C. Hannikainen, and L. van Zyl. An Ultracompact X-Ray Binary in the

Globular Cluster M15 (NGC 7078). ApJ, 634:L105–L108, November 2005.  
doi: 10.1086/498712.

P. Eggleton. Evolutionary Processes in Binary and Multiple Stars. July 2006.

P. P. Eggleton. Approximations to the radii of Roche lobes. ApJ, 268:368, May 1983. doi: 10.1086/160960.

P. P. Eggleton, J. Faulkner, and B. P. Flannery. An Approximate Equation of State for Stellar Material. Astronomy and Astrophysics, Vol. 23, p. 325 (1973), 23:325, 1973. URL <http://adsabs.harvard.edu/abs/1973A&A...23..325E>.

M. C. Engel, C. O. Heinke, G. R. Sivakoff, K. G. Elshamouty, and P. D. Edmonds. A 2.15 hr Orbital Period for the Low-mass X-Ray Binary XB 1832-330 in the Globular Cluster NGC 6652. ApJ, 747:119, March 2012. doi: 10.1088/0004-637X/747/2/119.

J. Faulkner. Ultrashort-Period Binaries, Gravitational Radiation, and Mass Transfer. I. The Standard Model, with Applications to WZ Sagittae and Z Camelopardalis. ApJ, 170:L99, December 1971. doi: 10.1086/180848.

J. W. Ferguson, D. R. Alexander, F. Allard, T. Barman, J. G. Bodnarik, P. H. Hauschildt, A. Heffner-Wong, and A. Tamai. Low-Temperature Opacities. ApJ, 623:585–596, apr 2005. doi: 10.1086/428642.

T. Fragos, V. Kalogera, K. Belczynski, G. Fabbiano, D. W. Kim, N. J. Brassington, L. Angelini, R. L. Davies, J. S. Gallagher, A. R. King, S. Pellegrini, G. Trinchieri, S. E. Zepf, A. Kundu, and A. Zezas. Models for Low-Mass X-Ray Binaries in the Elliptical Galaxies NGC 3379 and NGC 4278: Comparison with Observations. ApJ, 683:346–356, August 2008. doi: 10.1086/588456.

T. Fragos, B. D. Lehmer, S. Naoz, A. Zezas, and A. Basu-Zych. Energy Feedback from X-Ray Binaries in the Early Universe. ApJ, 776:L31, October 2013. doi: 10.1088/2041-8205/776/2/L31.

Chris L. Fryer, Krzysztof Belczynski, Grzegorz Wiktorowicz, Michal Dominik, Vicky Kalogera, and Daniel E. Holz. Compact Remnant Mass Function: Dependence on the Explosion Mechanism and Metallicity. ApJ, 749:91, April 2012. doi: 10.1088/0004-637X/749/1/91.

G. M. Fuller, W. A. Fowler, and M. J. Newman. Stellar weak interaction rates for intermediate-mass nuclei. IV - Interpolation procedures for rapidly varying lepton capture rates using effective log (ft)-values. ApJ, 293:1–16, jun 1985. doi: 10.1086/163208.

Gaia Collaboration, A. G. A. Brown, A. Vallenari, T. Prusti, J. H. J. de Bruijne, C. Babusiaux, and M. Biermann. Gaia Early Data Release 3: Summary of the contents and survey properties. arXiv e-prints, art. arXiv:2012.01533, December 2020.

Duncan K. Galloway, Deepto Chakrabarty, Edward H. Morgan, and Ronald A. Remillard. Discovery of a High-Latitude Accreting Millisecond Pulsar in an Ultracompact Binary. ApJ, 576:L137–L140, September 2002. doi: 10.1086/343841.

Duncan K. Galloway, Craig B. Markwardt, Edward H. Morgan, Deepto Chakrabarty, and Tod E. Strohmayer. Discovery of the Accretion-powered Millisecond X-Ray Pulsar IGR J00291+5934. ApJ, 622:L45–L48, March 2005. doi: 10.1086/429563.

N. Grevesse and A. Noels. La composition chimique du Soleil. In B. Hauck, S. Paltani, and D. Raboud, editors, Perfectionnement de l'Association Vaudoise des Chercheurs en Physique, pages 205–257, 1993.

J. M. Hameury, A. R. King, J. P. Lasota, and F. Raison. Structure and evolution of X-ray heated compact binaries. A&A, 277:81–92, September 1993.

W. E. Harris. A New Catalog of Globular Clusters in the Milky Way. ArXiv e-prints, December 2010.

C. O. Heinke, P. G. Jonker, R. Wijnands, and R. E. Taam. Constraints on Thermal X-Ray Radiation from SAX J1808.4-3658 and Implications for Neutron Star Neutrino Emission. ApJ, 660:1424–1427, May 2007. doi: 10.1086/513140.

C. O. Heinke, N. Ivanova, M. C. Engel, K. Pavlovskii, G. R. Sivakoff, T. F. Cartwright, and J. C. Gladstone. Galactic Ultracompact X-Ray Binaries: Disk Stability and Evolution. ApJ, 768:184, May 2013. doi: 10.1088/0004-637X/768/2/184.

W. Herschel. Catalogue of 500 New Nebulae, Nebulous Stars, Planetary Nebulae, and Clusters of Stars; With Remarks on the Construction of the Heavens. Philosophical Transactions of the Royal Society of London Series I, 92:477–528, 1802.

M. S. Hjellming and R. F. Webbink. Thresholds for rapid mass transfer in binary systems. I - Polytropic models. ApJ, 318:794–808, July 1987. doi: 10.1086/165412.

G. Hobbs, D. R. Lorimer, A. G. Lyne, and M. Kramer. A statistical study of 233 pulsar proper motions. MNRAS, 360:974–992, July 2005. doi: 10.1111/j.1365-2966.2005.09087.x.

L. Homer, P. A. Charles, T. Naylor, J. van Paradijs, M. Auriere, and L. Koch-Miramond. Periodic UV modulation of X1850-087: a double degenerate binary in the globular cluster NGC 6712? MNRAS, 282:L37–L46, October 1996. doi: 10.1093/mnras/282.3.L37.

R. Iaria, A. D'Aí, T. di Salvo, N. R. Robba, A. Riggio, A. Papitto, and L. Burderi. A ionized reflecting skin above the accretion disk of GX 349+2. A&A, 505:1143–1151, October 2009. doi: 10.1051/0004-6361/200911936.

R. Iaria, T. Di Salvo, M. Matranga, C. G. Galiano, A. D'Aí, A. Riggio, L. Burderi, A. Sanna, C. Ferrigno, M. Del Santo, F. Pintore, and N. R. Robba. A possible cyclotron resonance scattering feature near 0.7 keV in X1822-371. A&A, 577:A63, May 2015. doi: 10.1051/0004-6361/201423402.

C. A. Iglesias and F. J. Rogers. Radiative opacities for carbon- and oxygen-rich mixtures. ApJ, 412:752–760, aug 1993. doi: 10.1086/172958.

C. A. Iglesias and F. J. Rogers. Updated Opal Opacities. ApJ, 464:943, jun 1996. doi: 10.1086/177381.

S. A. Illovaisky, M. Auriere, L. Koch-Miramond, C. Chevalier, J. P. Cordonni, and R. A. Crowe. The 17.1-h optical and X-ray orbital period of AC 211/X 2127+119 in M 15. A&A, 270:139–150, March 1993.

J. J. M. in't Zand, F. Hulleman, C. B. Markwardt, M. Méndez, E. Kuulkers, R. Cornelisse, J. Heise, T. E. Strohmayer, and F. Verbunt. Bursts, eclipses, dips and a refined position for the luminous low-mass X-ray binary in the globular cluster Terzan 6. A&A, 406:233–243, July 2003. doi: 10.1051/0004-6361:20030681.

N. Itoh, H. Totsuji, S. Ichimaru, and H. E. Dewitt. Enhancement of thermonuclear reaction rate due to strong screening. II - Ionic mixtures. ApJ, 234: 1079–1084, December 1979. doi: 10.1086/157590.

N. Itoh, H. Hayashi, A. Nishikawa, and Y. Kohyama. Neutrino Energy Loss in Stellar Interiors. VII. Pair, Photo-, Plasma, Bremsstrahlung, and Recombination Neutrino Processes. ApJS, 102:411, feb 1996. doi: 10.1086/192264.

N. Ivanova. Low-Mass X-Ray Binaries with Pre-Main-Sequence Companions. ApJ, 653:L137–L140, December 2006. doi: 10.1086/510672.

N. Ivanova and J. L. A. Nandez. Common envelope events with low-mass giants: understanding the transition to the slow spiral-in. MNRAS, 462: 362–381, October 2016. doi: 10.1093/mnras/stw1676.

N. Ivanova and R. E. Taam. Magnetic Braking Revisited. ApJ, 599:516–521, December 2003. doi: 10.1086/379192.

N. Ivanova, F. A. Rasio, J. C. Lombardi, Jr., K. L. Dooley, and Z. F. Proulx. Formation of Ultracompact X-Ray Binaries in Dense Star Clusters. ApJ, 621:L109–L112, March 2005. doi: 10.1086/429220.

N. Ivanova, C. O. Heinke, F. A. Rasio, K. Belczynski, and J. M. Fregeau. Formation and evolution of compact binaries in globular clusters - II. Binaries with neutron stars. MNRAS, 386:553–576, May 2008. doi: 10.1111/j.1365-2966.2008.13064.x.

N. Ivanova, S. Justham, X. Chen, O. De Marco, C. L. Fryer, E. Gaburov, H. Ge, E. Glebbeek, Z. Han, X.-D. Li, G. Lu, T. Marsh, P. Podsiadlowski, A. Potter, N. Soker, R. Taam, T. M. Tauris, E. P. J. van den Heuvel, and R. F. Webbink. Common envelope evolution: where we stand and how we can move forward. A&ARv, 21:59, February 2013. doi: 10.1007/s00159-013-0059-2.

C. Jain, B. Paul, and A. Dutta. New measurement of orbital and spin period evolution of the accretion disc corona source 4U 1822-37. MNRAS, 409: 755–762, December 2010. doi: 10.1111/j.1365-2966.2010.17336.x.

Paul C. Joss and Saul A. Rappaport. Neutron Stars in Interacting Binary Systems. Annual Review of Astronomy and Astrophysics, 22:537–592, January 1984. doi: 10.1146/annurev.aa.22.090184.002541.

Stephen Justham, Saul Rappaport, and Philipp Podsiadlowski. Magnetic braking of Ap/Bp stars: application to compact black-hole X-ray binaries. *MNRAS*, 366:1415–1423, March 2006. doi: 10.1111/j.1365-2966.2005.09907.x.

P. Kaaret, E. H. Morgan, R. Vanderspek, and J. A. Tomsick. Discovery of the Millisecond X-Ray Pulsar HETE J1900.1-2455. *ApJ*, 638:963–967, February 2006. doi: 10.1086/498886.

Vassiliki Kalogera and Ronald F. Webbink. Formation of Low-Mass X-Ray Binaries. II. Common Envelope Evolution of Primordial Binaries with Extreme Mass Ratios. *ApJ*, 493(1):351–367, January 1998. doi: 10.1086/305085.

S. Karino and J. C. Miller. Accretion mode of the ultraluminous X-ray source M82 X-2. *MNRAS*, 462(4):3476–3482, November 2016. doi: 10.1093/mnras/stw1180.

Steven D. Kawaler. Angular Momentum Loss in Low-Mass Stars. *ApJ*, 333:236, October 1988. doi: 10.1086/166740.

L. Keek, W. Iwakiri, M. Serino, D. R. Ballantyne, J. J. M. in't Zand, and T. E. Strohmayer. X-Ray Reflection and an Exceptionally Long Thermonuclear Helium Burst from IGR J17062-6143. *ApJ*, 836:111, February 2017. doi: 10.3847/1538-4357/836/1/111.

Henry A. Kobulnicky and Chris L. Fryer. A New Look at the Binary Characteristics of Massive Stars. *ApJ*, 670(1):747–765, November 2007. doi: 10.1086/522073.

A. K. H. Kong, P. A. Charles, L. Homer, E. Kuulkers, and D. O'Donoghue. Simultaneous X-ray/optical observations of GX9+9 (4U1728-16). *MNRAS*, 368:781–795, May 2006. doi: 10.1111/j.1365-2966.2006.10157.x.

Z. Kopal. The classification of close binary systems. Annales d'Astrophysique, 18:379, January 1955.

R. P. Kraft, J. Mathews, and J. L. Greenstein. Binary Stars among Cataclysmic Variables. II. Nova WZ Sagittae: a Possible Radiator of Gravitational Waves. ApJ, 136:312–315, July 1962. doi: 10.1086/147381.

H. A. Krimm, C. B. Markwardt, C. J. Deloye, P. Romano, D. Chakrabarty, S. Campana, J. R. Cummings, D. K. Galloway, N. Gehrels, J. M. Hartman, P. Kaaret, E. H. Morgan, and J. Tueller. Discovery of the Accretion-powered Millisecond Pulsar SWIFT J1756.9-2508 with a Low-Mass Companion. ApJ, 668:L147–L150, October 2007. doi: 10.1086/522959.

L. D. Landau and E. M. Lifshitz. The classical theory of fields. 1975.

N. R. Landin, L. T. S. Mendes, and L. P. R. Vaz. Theoretical values of convective turnover times and Rossby numbers for solar-like, pre-main sequence stars. A&A, 510:A46, Feb 2010. doi: 10.1051/0004-6361/200913015.

K. Langanke and G. Martínez-Pinedo. Shell-model calculations of stellar weak interaction rates: II. Weak rates for nuclei in the mass range  $/A=45-65$  in supernovae environments. Nuclear Physics A, 673:481–508, jun 2000. doi: 10.1016/S0375-9474(00)00131-7.

J.-P. Lasota. The disc instability model of dwarf novae and low-mass X-ray binary transients. New Astron. Rev., 45:449–508, June 2001. doi: 10.1016/S1387-6473(01)00112-9.

James M. Lattimer and Madappa Prakash. Neutron star observations: Prognosis for equation of state constraints. Phys. Rep., 442(1-6):109–165, Apr 2007. doi: 10.1016/j.physrep.2007.02.003.

LIGO Scientific Collaboration and VIRGO Collaboration. GW151226: Observation of Gravitational Waves from a 22-Solar-Mass Binary Black Hole

Coalescence. Phys. Rev. Lett., 116:241103, June 2016. doi: 10.1103/PhysRevLett.116.241103.

LIGO Scientific Collaboration and Virgo Collaboration. GW170817: Observation of Gravitational Waves from a Binary Neutron Star Inspiral. Phys. Rev. Lett., 119:161101, October 2017. doi: 10.1103/PhysRevLett.119.161101.

Q. Z. Liu, J. van Paradijs, and E. P. J. van den Heuvel. A catalogue of low-mass X-ray binaries in the Galaxy, LMC, and SMC (Fourth edition). A&A, 469: 807–810, July 2007. doi: 10.1051/0004-6361:20077303.

D. Lommen, S. van Straaten, M. van der Klis, and B. Anthonisse. RXTE observations of the dipping low-mass X-ray binary 4U 1624-49. A&A, 435: 1005–1011, June 2005. doi: 10.1051/0004-6361:20040405.

Bo Ma and Xiang-Dong Li. The Bifurcation Periods in Low-Mass X-Ray Binaries: The Effect of Magnetic Braking and Mass Loss. ApJ, 691(2):1611–1617, Feb 2009a. doi: 10.1088/0004-637X/691/2/1611.

Bo Ma and Xiang-Dong Li. Formation of Ultracompact X-Ray Binaries through Circumbinary Disk-Driven Mass Transfer. ApJ, 698(2):1907–1913, Jun 2009b. doi: 10.1088/0004-637X/698/2/1907.

C. B. Markwardt and J. H. Swank. XTE J1814-338. IAU Circ., 8144, June 2003.

C. B. Markwardt, J. H. Swank, T. E. Strohmayer, J. J. M. in 't Zand, and F. E. Marshall. Discovery of a Second Millisecond Accreting Pulsar: XTE J1751-305. ApJ, 575:L21–L24, August 2002. doi: 10.1086/342612.

C. B. Markwardt, E. Smith, and J. H. Swank. XTE J1807-294. International Astronomical Union Circular, 8080:2, February 2003.

Brian D. Mason, William I. Hartkopf, Douglas R. Gies, Todd J. Henry, and John W. Helsel. The High Angular Resolution Multiplicity of Massive Stars. AJ, 137(2):3358–3377, February 2009. doi: 10.1088/0004-6256/137/2/3358.

D. Mata Sánchez, T. Muñoz-Darias, J. Casares, D. Steeghs, C. Ramos Almeida, and J. A. Acosta Pulido. Mass constraints to Sco X-1 from Bowen fluorescence and deep near-infrared spectroscopy. MNRAS, 449:L1–L5, April 2015. doi: 10.1093/mnrasl/slv002.

Sean P. Matt, Giovanni Pinzón, Thomas P. Greene, and Ralph E. Pudritz. Spin Evolution of Accreting Young Stars. II. Effect of Accretion-powered Stellar Winds. ApJ, 745(1):101, Jan 2012. doi: 10.1088/0004-637X/745/1/101.

L. Mestel. Magnetic braking by a stellar wind-I. MNRAS, 138:359, 1968. doi: 10.1093/mnras/138.3.359.

L. Mestel and H. C. Spruit. On magnetic braking of late-type stars. MNRAS, 226:57–66, May 1987. doi: 10.1093/mnras/226.1.57.

F. Meyer and E. Meyer-Hofmeister. On the Elusive Cause of Cataclysmic Variable Outbursts. A&A, 104:L10, 1981.

J. Michell. An Inquiry into the Probable Parallax, and Magnitude of the Fixed Stars, from the Quantity of Light Which They Afford us, and the Particular Circumstances of Their Situation, by the Rev. John Michell, B. D. F. R. S. Philosophical Transactions of the Royal Society of London Series I, 57: 234–264, 1767.

A. S. Mondal, G. C. Dewangan, M. Pahari, and B. Raychaudhuri. NuSTAR view of the Z-type neutron star low-mass X-ray binary Cygnus X-2. MNRAS, 474:2064–2072, February 2018. doi: 10.1093/mnras/stx2931.

G. Nelemans, L. R. Yungelson, M. V. van der Sluys, and C. A. Tout. The chemical composition of donors in AM CVn stars and ultracompact X-ray

binaries: observational tests of their formation. MNRAS, 401:1347–1359, January 2010. doi: 10.1111/j.1365-2966.2009.15731.x.

L. A. Nelson, S. A. Rappaport, and P. C. Joss. The evolution of ultrashort period binary systems. ApJ, 304:231–240, May 1986. doi: 10.1086/164156.

Lorne A. Nelson and Saul Rappaport. Theoretical Considerations on the Properties of Accreting Millisecond Pulsars. ApJ, 598(1):431–445, November 2003. doi: 10.1086/378798.

R. W. Noyes, L. W. Hartmann, S. L. Baliunas, D. K. Duncan, and A. H. Vaughan. Rotation, convection, and magnetic activity in lower main-sequence stars. ApJ, 279:763–777, April 1984. doi: 10.1086/161945.

T. Oda, M. Hino, K. Muto, M. Takahara, and K. Sato. Rate Tables for the Weak Processes of sd-Shell Nuclei in Stellar Matter. Atomic Data and Nuclear Data Tables, 56:231–403, mar 1994. doi: 10.1006/adnd.1994.1007.

F. Özel and P. Freire. Masses, Radii, and the Equation of State of Neutron Stars. ARA&A, 54:401–440, September 2016. doi: 10.1146/annurev-astro-081915-023322.

A. Papitto, C. Ferrigno, E. Bozzo, N. Rea, L. Pavan, L. Burderi, M. Burgay, S. Campana, T. di Salvo, M. Falanga, M. D. Filipović, P. C. C. Freire, J. W. T. Hessels, A. Possenti, S. M. Ransom, A. Riggio, P. Romano, J. M. Sarkissian, I. H. Stairs, L. Stella, D. F. Torres, M. H. Wieringa, and G. F. Wong. Swings between rotation and accretion power in a binary millisecond pulsar. Nature, 501:517–520, September 2013. doi: 10.1038/nature12470.

E. N. Parker. The Generation of Magnetic Fields in Astrophysical Bodies.IV. The Solar and Terrestrial Dynamos. ApJ, 164:491, March 1971. doi: 10.1086/150862.

- A. N. Parmar, T. Oosterbroek, L. Sidoli, L. Stella, and F. Frontera. BeppoSAX study of the X-ray binary XB 1832-330 located in the globular cluster NGC 6652. [A&A](#), 380:490–493, December 2001. doi: 10.1051/0004-6361:20011464.
- A. Patruno. The Slow Orbital Evolution of the Accreting Millisecond Pulsar IGR J0029+5934. [ApJ](#), 839:51, April 2017. doi: 10.3847/1538-4357/aa6986.
- K. Pavlovskii and N. Ivanova. Mass transfer from giant donors. [MNRAS](#), 449: 4415–4427, June 2015. doi: 10.1093/mnras/stv619.
- K. Pavlovskii and N. Ivanova. Mass transfer and magnetic braking in Sco X-1. [MNRAS](#), 456:263–269, February 2016. doi: 10.1093/mnras/stv2685.
- B. Paxton, L. Bildsten, A. Dotter, F. Herwig, P. Lesaffre, and F. Timmes. Modules for Experiments in Stellar Astrophysics (MESA). [ApJS](#), 192:3, January 2011. doi: 10.1088/0067-0049/192/1/3.
- B. Paxton, M. Cantiello, P. Arras, L. Bildsten, E. F. Brown, A. Dotter, C. Mankovich, M. H. Montgomery, D. Stello, F. X. Timmes, and R. Townsend. Modules for Experiments in Stellar Astrophysics (MESA): Planets, Oscillations, Rotation, and Massive Stars. [ApJS](#), 208:4, September 2013. doi: 10.1088/0067-0049/208/1/4.
- B. Paxton, P. Marchant, J. Schwab, E. B. Bauer, L. Bildsten, M. Cantiello, L. Dessart, R. Farmer, H. Hu, N. Langer, R. H. D. Townsend, D. M. Townsley, and F. X. Timmes. Modules for Experiments in Stellar Astrophysics (MESA): Binaries, Pulsations, and Explosions. [ApJS](#), 220:15, September 2015. doi: 10.1088/0067-0049/220/1/15.
- B. Paxton, J. Schwab, E. B. Bauer, L. Bildsten, S. Blinnikov, P. Duffell, R. Farmer, J. A. Goldberg, P. Marchant, E. Sorokina, A. Thoul, R. H. D. Townsend, and F. X. Timmes. Modules for Experiments in Stellar Astrophysics (MESA): Convective Boundaries, Element Diffusion, and Massive

Star Explosions. ApJS, 234:34, February 2018. doi: 10.3847/1538-4365/aaa5a8.

Bill Paxton, R. Smolec, Josiah Schwab, A. Gautschy, Lars Bildsten, Matteo Cantiello, Aaron Dotter, R. Farmer, Jared A. Goldberg, Adam S. Jermyn, S. M. Kanbur, Pablo Marchant, Anne Thoul, Richard H. D. Townsend, William M. Wolf, Michael Zhang, and F. X. Timmes. Modules for Experiments in Stellar Astrophysics (MESA): Pulsating Variable Stars, Rotation, Convective Boundaries, and Energy Conservation. ApJS, 243(1):10, Jul 2019. doi: 10.3847/1538-4365/ab2241.

W. Penninx and T. Augusteijn. The optical counterpart of the source GX 349+2. A&A, 246:L81, Jun 1991.

P. Podsiadlowski, S. Rappaport, and E. D. Pfahl. Evolutionary Sequences for Low- and Intermediate-Mass X-Ray Binaries. ApJ, 565:1107–1133, February 2002. doi: 10.1086/324686.

Ph. Podsiadlowski. Irradiation-driven mass transfer in low-mass X-ray binaries. Nature, 350:136–138, March 1991. doi: 10.1038/350136a0.

Ph. Podsiadlowski and S. Rappaport. Cygnus X-2: The Descendant of an Intermediate-Mass X-Ray Binary. ApJ, 529(2):946–951, February 2000. doi: 10.1086/308323.

O. R. Pols, C. A. Tout, P. P. Eggleton, and Z. Han. Approximate input physics for stellar modelling. MNRAS, 274:964–974, jun 1995. doi: 10.1093/mnras/274.3.964.

G. Ponti, S. Bianchi, T. Muñoz-Darias, and K. Nandra. Measuring masses in low mass X-ray binaries via X-ray spectroscopy: the case of MXB 1659-298. MNRAS, June 2018. doi: 10.1093/mnrasl/sly120.

A. Y. Potekhin and G. Chabrier. Thermodynamic Functions of Dense Plasmas: Analytic Approximations for Astrophysical Applications. Contributions to Plasma Physics, 50:82–87, jan 2010. doi: 10.1002/ctpp.201010017.

Sammanani S. Premachandra, Duncan K. Galloway, Jorge Casares, Danny T. Steeghs, and Thomas R. Marsh. Precision Ephemerides for Gravitational Wave Searches. II. Cyg X-2. ApJ, 823:106, June 2016. doi: 10.3847/0004-637X/823/2/106.

S. Rappaport, F. Verbunt, and P. C. Joss. A new technique for calculations of binary stellar evolution, with application to magnetic braking. ApJ, 275: 713–731, December 1983. doi: 10.1086/161569.

S. A. Rappaport, Ph. Podsiadlowski, and E. Pfahl. Stellar-mass black hole binaries as ultraluminous X-ray sources. MNRAS, 356(2):401–414, January 2005. doi: 10.1111/j.1365-2966.2004.08489.x.

E. M. Ratti, D. T. H. Steeghs, P. G. Jonker, M. A. P. Torres, C. G. Bassa, and F. Verbunt. Optical spectroscopy of the quiescent counterpart to EXO 0748-676: a black widow scenario? MNRAS, 420:75–83, February 2012. doi: 10.1111/j.1365-2966.2011.19999.x.

Meredith L. Rawls, Jerome A. Orosz, Jeffrey E. McClintock, Manuel A. P. Torres, Charles D. Bailyn, and Michelle M. Buxton. Refined Neutron Star Mass Determinations for Six Eclipsing X-Ray Pulsar Binaries. ApJ, 730:25, March 2011. doi: 10.1088/0004-637X/730/1/25.

D. Reimers. Circumstellar absorption lines and mass loss from red giants. Memoires of the Societe Royale des Sciences de Liege, 8:369–382, 1975.

M. Renzo, C. D. Ott, S. N. Shore, and S. E. de Mink. Systematic survey of the effects of wind mass loss algorithms on the evolution of single massive stars. A&A, 603:A118, July 2017. doi: 10.1051/0004-6361/201730698.

Victor Réville, Allan Sacha Brun, Sean P. Matt, Antoine Strugarek, and Rui F. Pinto. The Effect of Magnetic Topology on Thermally Driven Wind: Toward a General Formulation of the Braking Law. ApJ, 798:116, January 2015. doi: 10.1088/0004-637X/798/2/116.

Luciano Rezzolla, Elias R. Most, and Lukas R. Weih. Using Gravitational-wave Observations and Quasi-universal Relations to Constrain the Maximum Mass of Neutron Stars. ApJ, 852(2):L25, Jan 2018. doi: 10.3847/2041-8213/aaa401.

H. Ritter. Turning on and off mass transfer in cataclysmic binaries. A&A, 202: 93–100, August 1988.

H. Ritter and U. Kolb. Catalogue of cataclysmic binaries, low-mass X-ray binaries and related objects (Seventh edition). A&A, 404:301–303, June 2003. doi: 10.1051/0004-6361:20030330.

F. J. Rogers and A. Nayfonov. Updated and Expanded OPAL Equation-of-State Tables: Implications for Helioseismology. ApJ, 576:1064–1074, September 2002. doi: 10.1086/341894.

M. M. Romanova, A. A. Blinova, G. V. Ustyugova, A. V. Koldoba, and R. V. E. Lovelace. Properties of strong and weak propellers from MHD simulations. New Astron., 62:94–114, Jul 2018. doi: 10.1016/j.newast.2018.01.011.

M. Ruderman, J. Shaham, M. Tavani, and D. Eichler. Late Evolution of Very Low Mass X-Ray Binaries Sustained by Radiation from Their Primaries. ApJ, 343:292, August 1989. doi: 10.1086/167704.

E. E. Salpeter. Electrons Screening and Thermonuclear Reactions. Australian Journal of Physics, 7:373, September 1954. doi: 10.1071/PH540373.

H. Sana, S. E. de Mink, A. de Koter, N. Langer, C. J. Evans, M. Gieles, E. Gosset, R. G. Izzard, J.-B. Le Bouquin, and F. R. N. Schneider. Binary

Interaction Dominates the Evolution of Massive Stars. Science, 337:444, July 2012. doi: 10.1126/science.1223344.

Hugues Sana and Christopher J. Evans. The multiplicity of massive stars. In Coralie Neiner, Gregg Wade, Georges Meynet, and Geraldine Peters, editors, Active OB Stars: Structure, Evolution, Mass Loss, and Critical Limits, volume 272, pages 474–485, July 2011. doi: 10.1017/S1743921311011124.

A. Sanna, L. Burderi, A. Riggio, F. Pintore, T. Di Salvo, A. F. Gambino, R. Iaria, M. Matranga, and F. Scarano. Timing of the accreting millisecond pulsar SAX J1748.9-2021 during its 2015 outburst. MNRAS, 459:1340–1349, June 2016. doi: 10.1093/mnras/stw740.

A. Sanna, E. Bozzo, A. Papitto, A. Riggio, C. Ferrigno, T. Di Salvo, R. Iaria, S. M. Mazzola, N. D’Amico, and L. Burderi. XMM-Newton detection of the 2.1 ms coherent pulsations from IGR J17379-3747. ArXiv e-prints, art. arXiv:1807.08574, July 2018.

D. Saumon, G. Chabrier, and H. M. van Horn. An Equation of State for Low-Mass Stars and Giant Planets. ApJS, 99:713, aug 1995. doi: 10.1086/192204.

T. Shahbaz, C. Zurita, J. Casares, G. Dubus, P. A. Charles, R. M. Wagner, and E. Ryan. The Optical Light Curves of XTE J2123-058. III. The Mass of the Binary Components and the Structure of the Quiescent Accretion Disk. ApJ, 585:443–452, March 2003. doi: 10.1086/346001.

T. Shahbaz, C. A. Watson, and H. Hernandez-Peralta. On the ultracompact nature of 4U1822-000. MNRAS, 376:1886–1888, April 2007. doi: 10.1111/j.1365-2966.2007.11579.x.

L. Sidoli, A. N. Parmar, T. Oosterbroek, L. Stella, F. Verbunt, N. Masetti, and D. Dal Fiume. BeppoSAX study of the broad-band properties of luminous

globular cluster X-ray sources. A&A, 368:451–463, March 2001. doi: 10.1051/0004-6361:20000558.

Alison Sills, M. H. Pinsonneault, and D. M. Terndrup. The Angular Momentum Evolution of Very Low Mass Stars. ApJ, 534(1):335–347, May 2000. doi: 10.1086/308739.

A. Skumanich. Time Scales for CA II Emission Decay, Rotational Braking, and Lithium Depletion. ApJ, 171:565, February 1972. doi: 10.1086/151310.

G. E. Soberman, E. S. Phinney, and E. P. J. van den Heuvel. Stability criteria for mass transfer in binary stellar evolution. A&A, 327:620–635, November 1997.

D. Steeghs and J. Casares. The Mass Donor of Scorpius X-1 Revealed. ApJ, 568:273–278, March 2002. doi: 10.1086/339224.

L. Stella, N. E. White, and W. Priedhorsky. The Discovery of 15–30 Hertz Quasi-periodic Oscillations in the X-Ray flux of 4U 1820-30. ApJ, 315:L49, April 1987. doi: 10.1086/184859.

T. E. Strohmayer, Z. Arzoumanian, S. Bogdanov, P. M. Bult, D. Chakrabarty, T. Enoto, K. C. Gendreau, S. Guillot, A. K. Harding, W. C. G. Ho, J. Homan, G. K. Jaisawal, L. Keek, M. Kerr, S. Mahmoodifar, C. B. Markwardt, S. M. Ransom, P. S. Ray, R. Remillard, and M. T. Wolff. NICER Discovers the Ultracompact Orbit of the Accreting Millisecond Pulsar IGR J17062-6143. ApJ, 858:L13, May 2018a. doi: 10.3847/2041-8213/aabf44.

T. E. Strohmayer, P. S. Ray, K. C. Gendreau, P. M. Bult, S. Guillot, S. Mahmoodifar, G. K. Jaisawal, Z. Arzoumanian, D. Altamirano, S. Bogdanov, D. Chakrabarty, T. Enoto, C. B. Markwardt, F. Ozel, and S. M. Ransom. NICER discovers millisecond pulsations from the neutron star LMXB IGR J17379-3747. The Astronomer's Telegram, 11507:1, April 2018b.

Takeru K. Suzuki. Structured Red Giant Winds with Magnetized Hot Bubbles and the Corona/Cool Wind Dividing Line. ApJ, 659:1592–1610, April 2007. doi: 10.1086/512600.

B. E. Tetarenko, G. R. Sivakoff, C. O. Heinke, and J. C. Gladstone. WATCH-DOG: A Comprehensive All-sky Database of Galactic Black Hole X-ray Binaries. ApJS, 222:15, February 2016. doi: 10.3847/0067-0049/222/2/15.

The LIGO Scientific Collaboration, the Virgo Collaboration, R. Abbott, T. D. Abbott, S. Abraham, F. Acernese, K. Ackley, A. Adams, C. Adams, R. X. Adhikari, and et al. GWTC-1: A Gravitational-Wave Transient Catalog of Compact Binary Mergers Observed by LIGO and Virgo during the First and Second Observing Runs. Physical Review X, 9(3):031040, July 2019. doi: 10.1103/PhysRevX.9.031040.

The LIGO Scientific Collaboration, the Virgo Collaboration, R. Abbott, T. D. Abbott, S. Abraham, F. Acernese, K. Ackley, A. Adams, C. Adams, R. X. Adhikari, and et al. GWTC-2: Compact Binary Coalescences Observed by LIGO and Virgo During the First Half of the Third Observing Run. arXiv e-prints, art. arXiv:2010.14527, October 2020a.

The LIGO Scientific Collaboration, the Virgo Collaboration, R. Abbott, T. D. Abbott, S. Abraham, F. Acernese, K. Ackley, A. Adams, C. Adams, R. X. Adhikari, and et al. Population Properties of Compact Objects from the Second LIGO-Virgo Gravitational-Wave Transient Catalog. arXiv e-prints, art. arXiv:2010.14533, October 2020b.

F. X. Timmes and F. D. Swesty. The Accuracy, Consistency, and Speed of an Electron-Positron Equation of State Based on Table Interpolation of the Helmholtz Free Energy. ApJS, 126:501–516, feb 2000. doi: 10.1086/313304.

Richard Townsend. Mesa sdk for linux, May 2019. URL <https://doi.org/10.5281/zenodo.2669541>.

M. Tremmel, T. Fragos, B. D. Lehmer, P. Tzanavaris, K. Belczynski, V. Kalogera, A. R. Basu-Zych, W. M. Farr, A. Hornschemeier, L. Jenkins, A. Ptak, and A. Zezas. Modeling the Redshift Evolution of the Normal Galaxy X-Ray Luminosity Function. ApJ, 766:19, March 2013. doi: 10.1088/0004-637X/766/1/19.

K. X. Van, N. Ivanova, and C. O. Heinke. Low-mass X-ray binaries: the effects of the magnetic braking prescription. MNRAS, 483:5595–5613, March 2019. doi: 10.1093/mnras/sty3489.

Kenny X. Van and Natalia Ivanova. Evolving LMXBs: CARB Magnetic Braking. ApJ, 886(2):L31, Dec 2019. doi: 10.3847/2041-8213/ab571c.

Kenny X. Van and Natalia Ivanova. Constraining Progenitors of Observed LMXBs Using CARB Magnetic Braking. Submitted, 2021.

M. V. van der Sluys, F. Verbunt, and O. R. Pols. Creating ultra-compact binaries in globular clusters through stable mass transfer. A&A, 431:647–658, February 2005. doi: 10.1051/0004-6361:20041777.

L. van Zyl, P. A. Charles, S. Arribas, T. Naylor, E. Mediavilla, and C. Hellier. The X-ray binary X2127+119 in M15: evidence for a very low mass, stripped-giant companion. MNRAS, 350:649–656, May 2004. doi: 10.1111/j.1365-2966.2004.07676.x.

Smriti Vats, Rudy Wijnands, Aastha S. Parikh, Laura Ootes, Nathalie Degehaar, and Dany Page. The quiescent state of the neutron-star X-ray transient GRS 1747-312 in the globular cluster Terzan 6. MNRAS, 477:2494–2502, June 2018. doi: 10.1093/mnras/sty733.

F. Verbunt. The formation of ultra-short period binaries in globular clusters. ApJ, 312:L23–L25, January 1987. doi: 10.1086/184812.

F. Verbunt and C. Zwaan. Magnetic braking in low-mass X-ray binaries. A&A, 100:L7–L9, July 1981.

Stefanie Wachter and Bruce Margon. Photometry of GX 349+2: Evidence for a 22-Hour Period. AJ, 112:2684, Dec 1996. doi: 10.1086/118212.

F. M. Walter, N. E. White, and J. Swank. 4U 1916-05. International Astronomical Union Circular, 3611:2, June 1981.

L. Wang, D. Steeghs, J. Casares, P. A. Charles, T. Muñoz-Darias, T. R. Marsh, R. I. Hynes, and K. O'Brien. System mass constraints for the accreting millisecond pulsar XTE J1814-338 using Bowen fluorescence. MNRAS, 466: 2261–2271, April 2017. doi: 10.1093/mnras/stw3312.

Z. Wang and D. Chakrabarty. The Orbital Period of the Ultracompact Low-Mass X-Ray Binary 4U 1543-624. ApJ, 616:L139–L142, December 2004. doi: 10.1086/426787.

Z. Wang, R. P. Breton, C. O. Heinke, C. J. Deloye, and J. Zhong. Multi-band Studies of the Optical Periodic Modulation in the X-Ray Binary SAX J1808.4-3658 during Its Quiescence and 2008 Outburst. ApJ, 765:151, March 2013. doi: 10.1088/0004-637X/765/2/151.

A. L. Watts, B. Krishnan, L. Bildsten, and B. F. Schutz. Detecting gravitational wave emission from the known accreting neutron stars. MNRAS, 389:839–868, September 2008. doi: 10.1111/j.1365-2966.2008.13594.x.

R. F. Webbink, S. Rappaport, and G. J. Savonije. On the evolutionary status of bright, low-mass X-ray sources. ApJ, 270:678–693, July 1983. doi: 10.1086/161159.

Edmund J. Weber and Jr. Davis, Leverett. The Angular Momentum of the Solar Wind. ApJ, 148:217–227, April 1967. doi: 10.1086/149138.

J. M. Weisberg and Y. Huang. Relativistic Measurements from Timing the Binary Pulsar PSR B1913+16. ApJ, 829:55, September 2016. doi: 10.3847/0004-637X/829/1/55.

K. Werner, T. Nagel, T. Rauch, N. J. Hammer, and S. Dreizler. VLT spectroscopy and non-LTE modeling of the C/O-dominated accretion disks in two ultracompact X-ray binaries. A&A, 450:725–733, May 2006. doi: 10.1051/0004-6361:20053768.

Mateusz Wisniewicz, Andrzej Zdziarski, Agnieszka Janiuk, Dorota Rosinska, and Agnieszka Slowikowska. Long-term quasi-periodicity of 4U 1636-536 resulting from accretion disc instability. In 41st COSPAR Scientific Assembly, volume 41, pages E1.1–19–16, July 2016.

T. E. Woods and N. Ivanova. Can We Trust Models for Adiabatic Mass Loss? ApJ, 739:L48, October 2011. doi: 10.1088/2041-8205/739/2/L48.

J. Xiang, J. C. Lee, M. A. Nowak, J. Wilms, and N. S. Schulz. The Accretion Disk Corona and Disk Atmosphere of 4U 1624-490 as Viewed by the Chandra High Energy Transmission Grating Spectrometer. ApJ, 701:984–993, August 2009. doi: 10.1088/0004-637X/701/2/984.

J. Zhong and Z. Wang. The Likely Orbital Period of the Ultracompact Low-mass X-ray Binary 2S 0918-549. ApJ, 729:8, March 2011. doi: 10.1088/0004-637X/729/1/8.

D. R. Zurek, C. Knigge, T. J. Maccarone, A. Dieball, and K. S. Long. An Ultracompact X-Ray Binary in the Globular Cluster NGC 1851. ApJ, 699:1113–1118, July 2009. doi: 10.1088/0004-637X/699/2/1113.